UiT
THE ARCTIC UNIVERSITY OF NORWAY

Faculty of Science and Technology
Department of Physics and Technology

Estimating thermospheric neutral densities using ISR-observations during active HF-radio wave ionospheric heating experiment

—

Marcus Nicolai Pedersen

FYS-3931 Master's thesis in Space Physics – December 2017

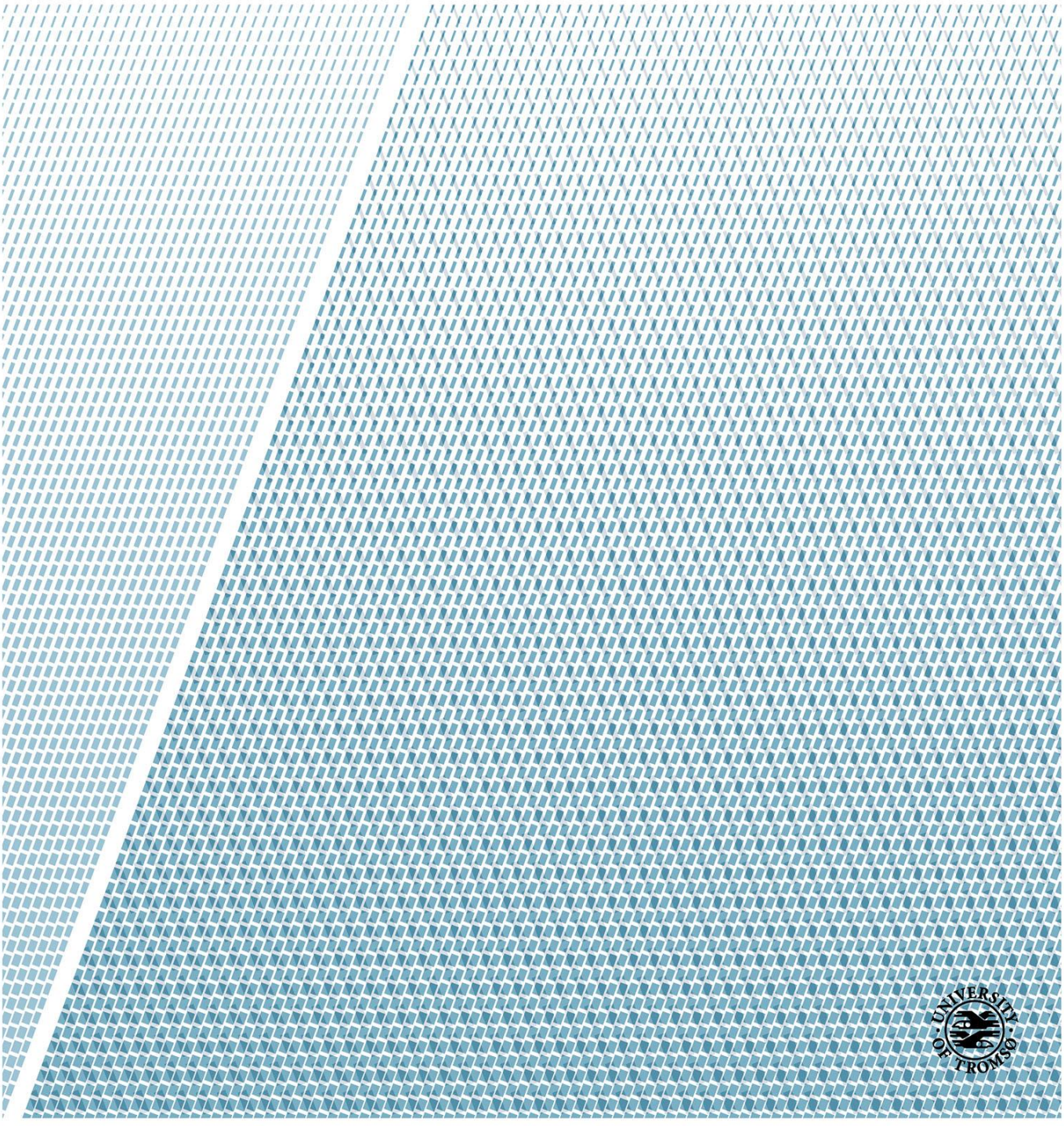

Estimating thermospheric neutral densities using ISR-observations during active HF-radio wave ionospheric heating experiment

Marcus N. Pedersen

Department of Physics and Technology

Faculty of Science and Technology

University of Tromsø

Norway

December 15, 2017

Abstract

In this study we present a method to estimate neutral thermospheric densities using ISR-observations following a sequence of high-frequency radio wave ionospheric heating modifications in the vicinity of the ionosphere peak density altitude (hmF2), and the results from two different days of observations with low geomagnetic activity levels (AP$\leq$ 4) that are compared to the MSIS model.

Slight discrepancies between the estimated neutral thermospheric densities and the MSIS model was found for the 18th of October, where the total density was a factor 0.98$\pm$0.02 of MSIS at the hmF2, with increasing deviations at higher altitudes, ending at a factor 0.94 ± 0.04 at 300 km. The main thermospheric neutral constituents, O, N_2 and O_2 were estimated to a factor 1.05 ± 0.03, 0.950 ± 0.002 and 0.73 ± 0.03 of the MSIS modelled constituents at hmF2, respectively, with all factors slightly decreasing with altitude.

The 15th of August achieved less electron heating at hmF2 due to a widespread electron content and high absorption in the E and D regions, and had significantly more noise making the standard errors in the estimates far exceed a reasonable density for quiet geomagnetic activities, at a factor 0.98 ± 0.37 of MSIS, making the result from the 15th of August inconclusive.

The findings from the observations has shown that this method can if observation-data from several individual heating-cycles are used extract the neutral thermospheric densities within reasonable certainty, if the thermospheric-ionospheric condition allow for repeated measurements.

Acknowledgement

First and foremost I would like to thank my supervisor Prof. Björn Gustavsson for letting me work on an extremely interesting experiment, and for always having an open door whenever I ran into troubles or had questions regarding my research.

Also I would like to thank my family for their continuous support throughout the years, and for telling me in the moment of doubt to apply for this tremendously fascinating field of study; now five years later I couldn't be more grateful.

And last but not least I would like to thank all the friends I have come to make during my years of studying, both here in Tromsø and elsewhere while on exchange, without all of you the experience would be incomplete.

Contents

Chapter 1

Introduction

The upper atmosphere is part of our protective layer shielding us from dangerous Solar Extreme Ultraviolet (EUV) radiation, where most of the energy goes into exciting neutral molecules into positive ions and leaving tons of free electrons swirling around the heavier ions, creating a partly ionized plasma engulfing the Earth from roughly 80 km altitude upto several thousands of km. The upper atmosphere is commonly described as two joint entities; the ionosphere and the thermosphere, where the ionosphere represents the ions and electrons behaviour by the governing electromagnetic (EM) forces, and the thermosphere represents the entirety of constituents that includes the neutral particles that constantly gets excited and de-excited due to energy-transfers from the precipitating electrons and internal collisions.

Getting a good estimate of the electron and ion density in the ionosphere can be achieved by well-established techniques with the use of ionosondes or incoherent scatter radars (ISR), because the electrons are negatively charged and the ions positive, they directly interact with the EM waves that are transmitted and we get a clear signature of their presence in the backscattered signal. The neutral particles on the other hand does not have this property, as they are neither negative nor positively charged and therefore do not *directly* interact with EM transmissions. This makes trying to measure the neutral density much more difficult than for its charged neighbours Nevertheless knowing their presence is still very important as they make up for most of the particles in the thermosphere and has a dominant effect on all chemical processes, e.g aurora. Any satellite in low earth orbit (LEO), such as the International Space Station are affected by a significant drag from the neutral particles it encounters, and over many orbits this drag will significantly reduce the velocity of the satellite and hence also make it fall closer to Earth. By knowing the density of the neutral particles at these altitudes better predictions regarding the satellites trajectory can be made and therefore reducing fuel and maintenance costs.

The ionosphere is also our gateway to study the magnetosphere (e.g. Cowley,

2000), by looking at the ionospheric structures and how they change with the space weather we can learn more about the interactions between the interplanetary magnetic field (IMF) and Earth's magnetosphere and its coupling with the ionosphere and upper atmosphere. Secondly as charged particles from the IMF penetrates into the ionosphere causing ionization it is important to have good estimates of the neutral density populations to correctly interpret the observations for inverse problems e.g. the height profile of the total energy deposited from the solar winds in the ionosphere.

In the last decades information regarding the thermospheric parameters such as the neutral density and its composition are most commonly derived from the Mass Spectrometer Incoherent Scatter (MSIS) atmospheric model (Hedin, 1987). This model has shown to have significant deviations from observations during high geomagnetic activities (Mikhailov and Schlegel, 1998; Litvin et al., 2000; Pavlov and Foster, 2001). In quiet periods the model agrees well with observations, but slight variations may still occur on a day to day basis. In this study we will be modelling the electron temperatures following ionospheric heating by a powerful HF radio wave, and by solving inverse problems using the observed electron temperatures derived from European Incoherent Scatter (EISCAT) and the electron energy rates to the ions and neutral constituents obtain most-likely parameters for the MSIS model on the day and time of the observations.

Chapter 2

Theory and Fundamentals

As the methods used to interpret the observations in this thesis are built on plasma theory such as the ionospheric response to HF radio waves and our understanding of incoherent scatter radar measurements, we will in this chapter introduce some of the theory underlying the most important concepts of plasma physics.

2.1 Plasma theory

A plasma is a collection of positive ions and free electrons, an ionized gas. As positive ions and electrons are oppositely charged they will naturally attract each other by the Coulomb force, making the less heavy electrons oscillate fast around the more massive ions. However, as the gas is filled with many such ions and electrons the long range Coulomb forces is more important than near-neighbouring forces, and as each specie themselves repel each other —ions repel ions, and electrons repel electrons— any dominant specie gives the gas a net charge, making it repel more of that specie and attract more of the opposite. Because of this, the plasma will naturally move toward an equilibrium of charge neutrality, moving so that the overall charge of the plasma is zero, a condition for the plasma better known as the plasma being *quasi-neutral*.

A plasma in thermodynamic equilibrium can be described by a Maxwellian velocity distribution, characterized by an absolute temperature T. In the upper atmosphere above 100 km —where the electron, ion and neutral temperatures are not equal, $T_e \neq T_i \neq T_n$— steady state prevails when the net energy losses of each species is zero and each can be said to have a Maxwellian velocity distribution of their own. The three-dimensional Maxwellian distribution function is defined as:

$$f_M(v) = 4\pi v^2 \left(\frac{m}{2\pi k_B T}\right)^{3/2} \exp\left[\frac{-(v-v_d)^2}{2v_{th}^2}\right] \tag{2.1.1}$$

where $m,\ k_B,\ T,\ v,\ v_d,\ v_{th}$ is the particle mass, Boltzmann's constant, temper-

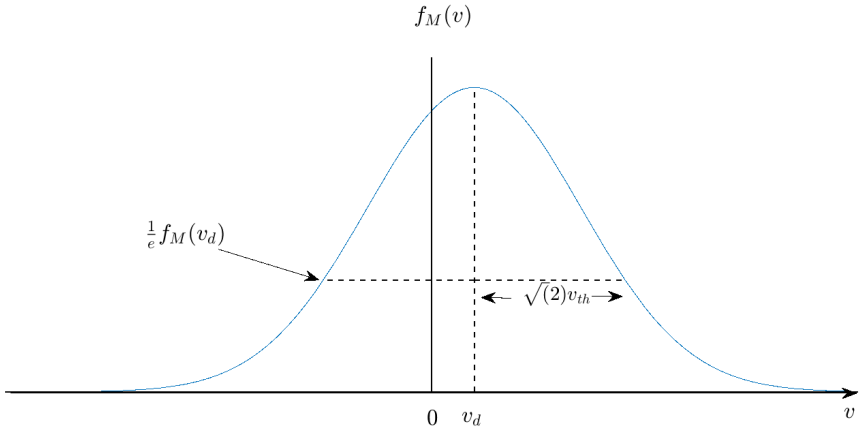

Figure 2.1: Maxwellian distribution: v_d is the drift velocity of the particle specie. $\pm\sqrt{2}v_{th}$ indicates where the velocity distribution has reduced by a factor $1/e$ from $f_M(v_d)$.

ature, individual particles velocity, drift velocity of the cloud and the thermal velocity, respectively.

As the plasma is an ionized gas and therefore heavily governed by the electromagnetic forces, it is often described as the fourth state of matter besides solids, liquids and neutral gases.

2.1.1 Gyrofrequency and E×B drift

In a collisionless plasma the electrons and ions are governed by the Lorentz force:

$$\mathbf{F} = q(\mathbf{E} + \mathbf{v} \times \mathbf{B}), \tag{2.1.2}$$

where q is the electric charge, $\mathbf{E}$ the electric field, $\mathbf{v}$ the velocity of the particle and $\mathbf{B}$ is the magnetic field.

If the particle is only in a magnetic field, so $\mathbf{E} = 0$ and $\mathbf{B} = \textit{constant}$ we get:

$$\mathbf{F} = q(\mathbf{v} \times \mathbf{B})$$

therefore the only force on the particle is perpendicular to both $\mathbf{B}$ and $\mathbf{v}$,

making it move in a circular motion and there must be a centripetal force:

$$\begin{aligned} m\frac{d\mathbf{v}_\perp}{dt} &= q\mathbf{v}_\perp \times \mathbf{B} \\ m\frac{v_\perp^2}{r} &= q\mathbf{v}_\perp \cdot \mathbf{B} \\ \rightarrow \mathbf{v}_\perp &= \frac{q\mathbf{B}r}{m}. \end{aligned}$$

The frequency of this rotational motion is:

$$f = \frac{\mathbf{v}_\perp}{2\pi r} \rightarrow \Omega = 2\pi f$$

$$\Omega = \frac{q\mathbf{B}}{m} \tag{2.1.3}$$

where Ω is the angular gyrofrequency of a charged particle in a constant magnetic field.

We have now showed how the particle behaves under only the influence of a magnetic field. But with a constant electric and magnetic field the Lorentz Force can be expressed as

$$m\frac{d(\mathbf{v}_\parallel + \mathbf{v}_\perp)}{dt} = q(\mathbf{E}_\parallel + \mathbf{E}_\perp + \mathbf{v} \times \mathbf{B}),$$

here the subscripts $\parallel$ and $\perp$ denotes the vector component parallel and perpendicular on the magnetic field, respectively. If we now look at the case were $\mathbf{E}_\parallel = 0$, saying the electric field is perpendicular on the $\mathbf{B}$ field, all components will be working on the particle in direction perpendicular to the $\mathbf{B}$ field, therefore

$$m\frac{d\mathbf{v}_\perp}{dt} = q\mathbf{E}_\perp + q\mathbf{v}_\perp \times \mathbf{B}$$

Now the forces governing the particle will be from the $q\mathbf{v}_\perp \times \mathbf{B}$ and $q\mathbf{E}_\perp$, therefore it is fair to suggest it will have a circular motion with some drift due to an instability caused by the electric field, we therefore split the velocity component

$$\mathbf{v}_\perp = \mathbf{u_E} + \mathbf{v}'_\perp$$

where $\mathbf{u_E}$ is the constant drift of the guiding center and $\mathbf{v}'_\perp$ is the cyclotron drift. This makes Equation (2.1.2)

$$m\frac{d\mathbf{v}'_\perp}{dt} + m\frac{d\mathbf{u_E}}{dt} = q\mathbf{E}_\perp + q\mathbf{v}'_\perp \times \mathbf{B} + q\mathbf{u_E} \times \mathbf{B}$$

where $\frac{d\mathbf{u_E}}{dt} = 0$. Now we're interested in the long term motion of this particle, therefore we want to look at how it changes over one or several gyrations to exclude the short term perturbations due to the cyclotron velocity

$$\langle m\frac{\mathbf{dv}'_\perp}{dt} - q\mathbf{v}'_\perp \times \mathbf{B}\rangle = q\mathbf{E}_\perp + q\mathbf{u_E} \times \mathbf{B}$$

we see the left hand size (LHS) is zero over one gyration, and we solve the right hand side (RHS) for $\mathbf{u_E}$

$$(\mathbf{E} \perp + \mathbf{u_E} \times \mathbf{B}) \times \mathbf{B} = 0$$
$$\mathbf{E}_\perp \times \mathbf{B} - \mathbf{u_E B^2} + \mathbf{B}(\mathbf{u_E} \cdot \mathbf{B}) = 0$$

and as $\mathbf{u_E} \perp \mathbf{B}$, $\mathbf{u_E} \cdot \mathbf{B} = 0$ and we see that

$$\mathbf{u_E} = \frac{\mathbf{E}_\perp \times \mathbf{B}}{B^2} \tag{2.1.4}$$

This is called the zeroth order drift, or more commonly known as $E \times B$ drift. The electrons and the ions in the upper ionosphere - where collisions are negligible and the particles mostly affected by the Lorentz force - drift with this velocity.

2.1.2 Debye shielding and debye length

Imagine putting a test charge in the plasma, how would we expect the electrical potential of this charge to drop of compared to if it was placed in a vacuum? As the test charge is surrounded by numerous charges of same and opposite polarity, some will attract and some repel to it. These other charges interacting with our test charge will move to restore neutrality in the plasma and try to cancel out the additional electrical potential that was added by our test charge.

To come to any conclusion regarding the potential we start by looking at the general expression of the Poisson's equation in order to look at the different contributors

$$\nabla^2 \phi = -\frac{\rho}{\epsilon_0} = \frac{e}{\epsilon_0}(n_e - n_i) - \frac{q}{\epsilon}(\delta(\vec{r})) \tag{2.1.5}$$

where ϕ is the electric potential, ρ charge density, and on the RHS we have the charge densities comprised of the three contributors, $-en_e$, en_i and $q(\delta(\vec{r}))$ that are the electron population, ion cloud and the test charge, respectively. Due to symmetry in the plasma the potential ϕ depends only on the radius r, this makes Poisson's equation:

$$\nabla^2 \phi(r) = \frac{1}{r^2}\frac{1}{dr}\left(r^2 \frac{d\phi}{dr}\right) = \frac{e}{\epsilon_0}\left(n_e - n_i\right) \tag{2.1.6}$$

We also assume thermal equilibrium in the plasma, and we can then use Boltzmann's relation for the distribution of the electrons and ions:

$$n_e = n_0 \exp\left(\frac{e\phi}{k_B T_e}\right)$$
$$n_i = n_0 \exp\left(\frac{-e\phi}{k_B T_e}\right).$$

Here we have related the fluctuations in n_e and n_i to the fluctuations in the electric potential ϕ, and we have used our statement of quasi-neutrality, that over sufficiently large scales $n_i = n_e = n_0$.
Away from the test charge we find

$$\frac{e\phi}{k_B T_e} \ll 1, \qquad \frac{e\phi}{k_B T_i} \ll 1$$

and we can use the expressions from the Boltzmann's distribution of n_e and n_i and use this to rewrite them as $n_e \approx n_0(1 + \frac{e\phi}{k_B T_e})$ and $n_i \approx n_0(1 - \frac{e\phi}{k_B T_i})$, and neglect any higher order terms. We use these expressions in Equation (2.1.6)

$$\frac{1}{r^2}\frac{d}{dr}\left(r^2 \frac{d\phi}{dr}\right) = \frac{n_0 e^2}{\epsilon_0 k_B}\left(\frac{1}{T_e} + \frac{1}{T_i}\right)\phi \tag{2.1.7}$$

and now we define the new parameters:

$$\lambda_e = \sqrt{\frac{\epsilon_0 k_B T_e}{n_0 e^2}}$$
$$\lambda_i = \sqrt{\frac{\epsilon_0 k_B T_i}{n_0 e^2}}$$
$$\frac{1}{\lambda_D^2} = \frac{1}{\lambda_e^2} + \frac{1}{\lambda_i^2}.$$

Here λ_D is the Debye length, the characteristic length of the potential in a plasma with only electrons and ion, but we could break down the ions into several ion species and they would each add to the characteristic length as showed above. Now to answer our first question, how will the potential of this test charge decay with increasing radius? For that we need to solve the differential Equation (2.1.5) for ϕ, using the parameters we have found we can rewrite this as:

$$\nabla^2 \phi = \frac{1}{\lambda_D^2}\phi + \frac{e}{\epsilon_0}\delta(\vec{r})$$

and this has the solution:

$$\phi(r) = \phi_0 \exp\left(\frac{-r}{\lambda_D}\right).$$

We see that the altered Coulomb potential inside a plasma decays as the exponential of the radius, and not the inverse as it does in vacuum. We also know that the initial condition for the potential at $r \to 0$ must be the same, $\phi_0 = \frac{q}{4\pi\epsilon_0 r}$, and our final expression for the altered Coulomb potential:

$$\phi(r) = \frac{q}{4\pi\epsilon_0 r}\exp\left(\frac{-r}{\lambda_D}\right) \tag{2.1.8}$$

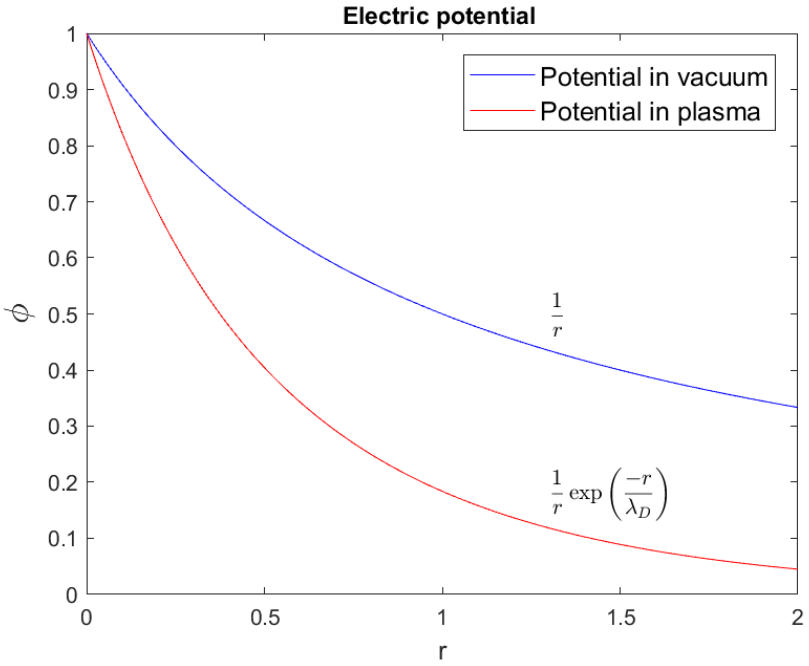

Figure 2.2: Normalized electric potential from a test charge in vacuum and in a plasma as a function of distance r in units of Debye lengths. The potential in the plasma decreases drastically faster than the unaltered Coulomb potential, giving rise to the Debye shielding of electric potential taking place inside an ionized gas.

with the characteristic e-folding Debye length

$$\frac{1}{\lambda_D^2} = \frac{1}{\lambda_e^2} + \frac{1}{\lambda_i^2}. \tag{2.1.9}$$

This rapid fading of any disturbing electric potential is a unique and strong property inhabited by plasmas, and is more commonly known as *Debye shielding*. Figure 2.2 shows the potential for a test charge both in vacuum and in a plasma as a function of radius measured in units of λ_D. We will see later in Section 3.1 how Debye shielding is an essential feature for the use of incoherent scatter radars.

2.1.3 Ion and electron mobility and velocity

The *mobility* is the ratio between how influenced the particles are by the electromagnetic forces and the forces due to binary collisions with other species, or more precise $\kappa_j = \frac{\Omega_j}{\nu_{jn}}$. The higher the gyrofrequency (Ω) is compared to the

neutral collision frequency (ν), the more freely will the particle gyrate around the magnetic field lines.
Starting from the ion and electron momentum equation:

$$n_j m_j \frac{d\mathbf{v_j}}{dt} = q_j n_j (\mathbf{E} + \mathbf{v_j} \times \mathbf{B}) - n_j m_j \nu_{jn} (\mathbf{v_j} - \mathbf{u_n}) \tag{2.1.10}$$

Here $j = i, e$, $q_e = -e$ and $q_i = e$. m_j is the mass of specie j, ν_{jn} is the collision frequency with neutral particles, $\mathbf{v_j}$ is the particle velocity and $\mathbf{u_n}$ is neutral wind velocity (bulk velocity of the neutral particles).
If we look at this while under steady-state ($\frac{d}{dt} = 0$) we can solve for the ion and electron velocity as

$$\mathbf{v_i} = \mathbf{u_n} + \frac{E}{m_i \nu_{in}} (\mathbf{E} + \mathbf{v_i} \times \mathbf{B}).$$

By solving Equation (2.1.10) with the expression for the ion and electron velocity under steady-state we obtain:

$$\mathbf{v_i} = \frac{\kappa_i}{1+\kappa_i^2} \frac{\mathbf{E}}{B} + \frac{\kappa_i^2}{1+\kappa_i^2} \frac{\mathbf{E} \times \mathbf{B}}{B^2} + \frac{\kappa_i^3}{1+\kappa_i^2} (\mathbf{E} \cdot \mathbf{B}) \mathbf{B} \tag{2.1.11a}$$

$$\mathbf{v_e} = -\frac{\kappa_e}{1+\kappa_e^2} \frac{\mathbf{E}}{B} + \frac{\kappa_e^2}{1+\kappa_e^2} \frac{\mathbf{E} \times \mathbf{B}}{B^2} - \frac{\kappa_e^3}{1+\kappa_e^2} (\mathbf{E} \cdot \mathbf{B}) \mathbf{B}, \tag{2.1.11b}$$

and assuming that the electric field, $\mathbf{E}$ only has perpendicular components to the magnetic field $\mathbf{B}$, we have $(\mathbf{E} \cdot \mathbf{B}) = 0$ and can further simplify this to:

$$\mathbf{v_i} = \frac{\kappa_i}{1+\kappa_i^2} \frac{\mathbf{E}}{B} + \frac{\kappa_i^2}{1+\kappa_i^2} \frac{\mathbf{E} \times \mathbf{B}}{B^2} \tag{2.1.12a}$$

and the electrons

$$\mathbf{v_e} = -\frac{\kappa_e}{1+\kappa_e^2} \frac{\mathbf{E}}{B} + \frac{\kappa_e^2}{1+\kappa_e^2} \frac{\mathbf{E} \times \mathbf{B}}{B^2} \tag{2.1.12b}$$

2.2 Conductivities in the ionosphere

Both electrons and ions move in the ionosphere, each carrying their own electric current given as $\mathbf{j_e} = -n_e \cdot e \cdot \mathbf{v_e}$ and $\mathbf{j_i} = n_e \cdot e \cdot \mathbf{v_e}$, where the total electric current is the sum of all the electrons current and the current from all different ion species (here all the ion species are denoted under one):

$$\mathbf{j} = n_e \cdot e \cdot (\mathbf{v_i} - \mathbf{v_e}),$$

Using the expression for the ion and electron velocity, Equation (2.1.11a and 2.1.11b) the current density in the ionosphere becomes

$$\mathbf{j} = n_e \cdot e \left[\left(\frac{\kappa_e}{1+\kappa_e^2} + \frac{\kappa_i}{1+\kappa_i^2} \right) \frac{\mathbf{E}_\perp}{B} - \left(\frac{\kappa_e^2}{1+\kappa_e^2} - \frac{\kappa_i^2}{1+\kappa_i^2} \right) \frac{\mathbf{E} \times \mathbf{B}}{B^2} + (\kappa_e + k_i) \frac{\mathbf{E}_\parallel}{B} \right]$$

where the $\mathbf{E} = \mathbf{E}_\perp + \mathbf{E}_\parallel$, perpendicular and parallel indicates directions with respect to $\mathbf{B}$.

Now we introduce the better known Pedersen, Hall and parallel conductivities:

$$\sigma_P = \frac{n_e \cdot e}{B}\left(\frac{\kappa_e}{1+\kappa_e^2} + \frac{\kappa_i}{1+\kappa_i^2}\right) \tag{2.2.1}$$

$$\sigma_H = \frac{n_e \cdot e}{B}\left(\frac{\kappa_e^2}{1+\kappa_e^2} - \frac{\kappa_i^2}{1+\kappa_i^2}\right) \tag{2.2.2}$$

$$\sigma_\parallel = \frac{n_e \cdot e}{B}(\kappa_e + \kappa_i) \tag{2.2.3}$$

and by using these conductivities we can simplify the current density expression above to:

$$\mathbf{J} = \sigma_P \mathbf{E}_\perp - \sigma_H \frac{\mathbf{E} \times \mathbf{B}}{B^2} + \sigma_\parallel \mathbf{E}_\parallel. \tag{2.2.4}$$

We will later in chapter 2.5 be describing the conductivity in of form of the conductivity tensor, and to clarify the directions let's say we have a coordinate system where the z-axis points along the magnetic field lines, then the conductivity tensors will be expressed as:

$$\bar{\sigma} = \begin{pmatrix} \sigma_P & -\sigma_H & 0 \\ \sigma_H & \sigma_P & 0 \\ 0 & 0 & \sigma_\parallel \end{pmatrix}. \tag{2.2.5}$$

2.3 Incoherent scattering

Incoherent scattering is a technique proposed by Professor Bill Gordon (Gordon, 1958). Each free electron in an ionized medium with many such free electrons will scatter some of the energy associated with an EM wave propagating trough. The incoherent backscattering of such a medium is the backscattering from density fluctuations in the plasma. As an electromagnetic wave is travelling through the plasma it makes the charged particles oscillate, and as the ions are far more massive than that of the electrons, the electrons will be oscillating much much faster than the ions, giving off far more radiation.

It was first thought that free independent electrons caused scattering, and that the backscattered signal would be extremely weak and detection would require enormous antennas (such as Arecibo). This assumption turned out to be wrong. It is true that the backscattered signal is weak — the total radar cross-section of an ionospheric column is like a pencil head — but the dominant scattering is not from free electrons, but from density fluctuations due

to waves in the plasma matching the Bragg condition. By having a probing frequency $\omega_{radar} \gg \omega_{debye}$ the wave propagates almost unperturbed through the ionospheric plasma, with only a small fraction of the wave energy going to accelerating the electrons, therefore we see the collective behaviour of the plasma as a whole. The fact that it backscatters off the collective behaviour allows us to use drastically smaller antennas (reducing the required antenna diameter from $\sim$ 300m to $\sim$ 40m) and still be able to estimate plasma parameters from the ion line spectrum.

The ions too absorb energy from the propagating wave, but ions have a far higher mass than the electrons, and thus their radar scattering cross section is a factor $(m_e/m_i)^2$ lower than the electrons and their contribution to backscattered signal is negligible. Even though little of the backscattered signal comes from the ions themselves, the electrons are bound to follow the ions in the plasma and the backscattered signal therefore reflects the motion of the ions.

The scattering mechanism is known as Thomson's scattering, and is just the low energy limit of Compton scattering. As the electromagnetic transmission travels through the collision-less plasma it makes the electrons oscillate along the transverse wave, accelerating them and in turn causing them to radiate at the same frequency as the incident transmission (Thomson, 1903). The oscillation is caused (for non-relativist particles) by the electric field, and the magnetic field plays no role (Thomson, 1903), and the particle accelerates in the direction of the electric field, resulting in electromagnetic dipole radiation (see Figure 2.4). For bistatic or tristatic experiments it is important to be aware the dipole radiation has an angular dependency on the incident and received wave, and can be shown to be diminishing by a factor $\cos^2\chi$, where χ is the angle difference; therefore measurements done at right angles to the incident wave will be in the blind spot of the backscattered radiation.

2.4 Electron energy transfers in the ionosphere

Cooling and heating of the electrons makes up much of the total energy flow in the ionosphere. For day-time conditions the F-region electron heating is dominated by (solar U.V radiation) photoelectron heating (Schunk and Nagy, 1978), while the most dominate electron cooling processes are:

- Elastic collision with positive ions
- Elastic collision with neutrals
- Vibrational excitation of O_2
- Rotational excitation of O_2
- Electron excitation of O
- Fine structure excitation of O
- Vibrational excitation of N_2
- Rotational excitation of N_2

In this chapter we will go through the analytical expressions of the electron

energy loss and background-heating used in this study to model the electron temperature, as well as explain some basic principles and underlying assumptions concerning the HF-heating.

2.4.1 Electron energy loss to neutrals

Stubbe and Varnum (1972) calculated and fitted the above cooling processes to analytical expressions. Some of these cross sections have been improved over the years, and hence also update cooling rates (see Pavlov, 1998a,b; Campbell et al., 2004; Jones et al., 2003).

Elastic Collisions

For the electron cooling rates caused by elastic collisions with neutrals, Stubbe and Varnum (1972) showed that for the elastic collisions between electrons and the most dominant neutral species in the ionosphere, O, N_2 and O_2, the analytical expressions for the energy transfer rate are:

$$Q_C(O) = -n_e n(O) \cdot 5.3 \cdot 10^{-19} T_e^{1/2} (T_e - T_n)(1 + 5.7 \cdot 10^{-4} T_e) \tag{2.4.1}$$

$$Q_C(O_2) = -n_2 n(O_2) \cdot 1.2 \cdot 10^{-18} T_e^{1/2} (T_e - T_n)(1 + 3.6 \cdot 10^{-2} T_e^{1/2}) \tag{2.4.2}$$

$$Q_C(N_2) = -n_e n(N_2) \cdot 1.8 \cdot 10^{-19} T_e (T_e - T_n)(1 - 1.21 \cdot 10^{-4} T_e) \tag{2.4.3}$$

They too showed that energy loss due to the electron excitation of the O(^{1}D) state of oxygen could be expressed as:

$$Q_{EE}(O) = n_e n(O) + 1.57 \cdot 10^{-12} \exp\left(f \frac{T_e - 3000}{3000 Te}\right) \left[\exp\left(-22713 \frac{T_e - T_n}{T_e T_n}\right) - 1\right] \tag{2.4.4}$$

where

$$f = 2.4 \cdot 10^4 + 3 \cdot 10^{-1}(T_e - 1500) - 1.947 \cdot 10^{-5}(T_e - 1500)(T_e - 4000)$$

And for the fine structure excitation of Oxygen, they furthered previous work done by Dalgarno et al. (1968) and showed that this energy loss could be expressed as:

$$Q_{fine}(O) = -n_e n(O) \cdot 3.4 \cdot 10^{-12} T_n^{-1} (1 - 7 \cdot 10^{-5} T_e)(T_e - T_n) \tag{2.4.5}$$

where n_e is the electron density, T_e is electron temperature, T_n is the neutral temperature and $n(O), n(O_2), n(N_2)$ is the number density of the atomic oxygen, molecular oxygen and molecular nitrogen, respectively. All cooling rates were measured in units of [eV cm^{-3} sec^{-1}].

Vibrational excitation N_2 and O_2

Pavlov (1998b) calculated an analytical expression for the electron cooling rates due to collisions of electrons with unexcited $N_2(0)$ and vibrationally excited $N_2(v > 0)$, as well as for unexcited $O_2(0)$ and vibrationally excited $O_2(v > 0)$. The electron energy loss due to vibrational excitation of N_2 can be expressed as:

$$\begin{aligned} L_0(N_2^*) =& n_e[N_2]\{1 - \exp(-E_1/T_{vib})\} \cdot \sum_{v=1}^{10} Q_{0v}\{1 - \exp\left[vE_1(T_e^{-1} - T_{vib}^{-1}\right]\} \\ L_v(N_2^*) =& n_e[N_2]\{1 - \exp(-E_1/T_{vib}\} \exp(-E_1/T_{vib}) \\ & \cdot \sum_{v=2}^{v=10} \{Q_{v1}\{1 - \exp\left[(v-1)E_1(T_e^{-1} - T_{vib}^{-1}\right]\} \end{aligned} \tag{2.4.6}$$

where $E_1 = 3353$ K (or equivalently $E_1 = 0.2889$ eV) is the energy level of the first vibrational state of N_2, $N_2(0)$ is the ground state, $N_2(v > 1)$ is a vibrationally excited state and $[N_2]$ is the number density of molecular nitrogen. The total electron energy loss due to vibrational excitation of the molecular nitrogen is the sum of the two

$$L(N_2^*) = L_0(N_2^*) + L_v(N_2^*).$$

A lot of the energy contribution to $L(N_2^*)$ arises from deexcitation from higher vibrational energy states, in particular $N_2(1)$ and $N_2(2)$, therefore the production rate of N_2(v) and production frequency of N_2 is of high importance, where the terms Q_{v1} and Q_{v0} are analytical functions of electron temperature that incorporates this, and is expressed as:

$$\begin{aligned} \log Q_{0v} &= A_{0v} + B_{0v}T_e + C_{0v}T_e^2 + D_{0v}T_e^3 + E_{0v}T_e^4 + F_{0v}T_e^5 - 16 \\ \log Q_{1v} &= A_{1v} + B_{1v}T_e + C_{1v}T_e^2 + D_{1v}T_e^3 + E_{1v}T_e^4 + F_{1v}T_e^5 - 16 \end{aligned}$$

with coefficients found from Table 1 and 3 in (Pavlov, 1998b). This table shows the coefficients for the temperature range $1600 - 6000$ K for excitations from the ground ($v = 0$) and first ($v = 1$) vibrational state upto the 10th vibrational state.

Pavlov (1998a) showed the electron cooling rate from (Prasad and Furman, 1973) due to excitation of the vibrational O_2 can be expressed as

$$L(O_v^*) = n_e[O_2]Q(T_e)\{1 - \exp(E_1(T_e - T_n)^{-1})\} \tag{2.4.7}$$

assuming the deexcitation rate of $O_2(v > 0)$ is the same as that for $O_2(1)$, and that $T_{vib} = T_n$. They made a similar analytical expression for the vibrational excitation of O_2 as for O_2:

$$L_{v0}(O) = A_v \exp\{(1 - B_v T_e^{-1})\}(C_v + D_v \sin\left[F_v(T_e - G_v)\right]\} \tag{2.4.8}$$

where the constants $A_v,\ B_v,\ C_v, D_v$ and G_v is from Table 1 in (Pavlov, 1998a). Equation (2.4.8) must be summed over all the contributing deexcitation states (1 - 7 is what they recommended, and what we will be using in our analysis)

Rotation excitaiton O_2 and N_2

The cooling rate due to rotational excitation of N_2 and O_2 they showed could be calculated as:

$$L_{rotN_2} = 1.255 \cdot 2.8 \cdot 10^{-14} N_2 \cdot T_e^{-1/2} \cdot (T_e - T_n) \tag{2.4.9}$$

$$L_{rotO_2} = 5.2 \cdot 10^{-15} O_2 \cdot T_e^{-1/2} \cdot (T_e - T_n) \tag{2.4.10}$$

where the correction factor of 1.255 in the electron energy loss to rotation N_2 was shown by Stubbe (1971); Stubbe and Varnum (1972).

2.4.2 Electron energy loss to ions

The electron energy-loss to the ions was modelled as (Schunk and Nagy, 2009):

$$L_{ei} = 3.2 \cdot 10^{-14} n_e \cdot f(n_e, n_i, T_e, T_i) \cdot \frac{T_e - T_i}{T_e^{1.5}} \cdot g([\tilde{\text{ion}}_{\text{specie}}]) \tag{2.4.11}$$

where f and g are a collective energy transfer function and appropriate ion specie weighing function:

$$f(n_e, n_i, T_e, T_i) = \ln\left(\frac{4k_B T_e}{(q \cdot e^{0.577})^2 \sqrt{\frac{k_B T_e}{4\pi n_e q}}}\right) - \left(\frac{n_e T_i}{n_i T_e} + 1\right) \cdot \ln\left(\sqrt{\frac{n_e T_i}{n_i T_e} + 1}\right)$$

$$g([\tilde{\text{ion}}_{\text{specie}}]) = [\tilde{\text{O}^+}] + 4[\tilde{\text{He}^+}] + 16[\tilde{\text{H}^+}] + 0.5[\tilde{\text{O}_2}^+] + 0.53[\tilde{\text{NO}^+}]$$

where $[\tilde{\ }]$ are expressed in percentage of the total ion density.

Finally the total electron energy loss to the neutrals and ions are the sum of all process above:

$$\begin{aligned} L = {} & Q_C(O) + Q_C(O_s) + Q_C(N_2) + Q_{EE}(O) + Q_{fine}(O) \\ & + L(N_2^*) + L(O^*) + L_{rotN_2} + L_{rotO_2} + L_{ei} \end{aligned} \tag{2.4.12}$$

2.5 Ionospheric response to HF radio waves

The first form of field-align irregularities (FAI) in the ionospheric F-region generated by a high power HF radio wave was detected by Thome and Blood (1974). Since then it has become well known that high power HF radio waves

can cause changes to the ionospheric plasma, e.g. enhancements to the electron temperature (Thomson, 1970; Mantas et al., 1981; Stocker et al., 1992).

The ionospheric response to the HF transmission highly depends on the frequency of the pump wave, ω_{HF}, and the plasma frequency, ω_{pe}. We will split them into two different cases: $\omega_{HF} < \omega_{pe}$ and $\omega_{HF} > \omega_{pe}$, that we will call overdense and underdense, respectively.

In the case of overdense heating, where the ionosphere critical frequency (foF2) is higher than the HF transmitted frequency the pump wave will be reflected and deposit most of its energy just below this reflection altitude, and due to the large number of plasma processes happening at this region it is difficult to accurately separate the heating due to HF-heating from the effects of non linear and resonance processes. Therefore the ionospheric heating has to be modelled by the use of the coupled ion and electron continuity, momentum, and energy equations (Hansen et al., 1992a,b; Shoucri et al., 1984).

For the underdense case the pump wave propagates through the ionosphere, and the heating becomes smoothly distributed in the vicinity of the hmF2 without creating sharp gradients in the plasma pressure so no significant n_e modulations arises. As underdense heating applies an ambient heat source that has little perturbations on the plasma in other ways it is far easier to model than the overdense case. Gustavsson et al. (2009) simplified the model of the ionospheric heating due to HF transmissions for the underdense case and showed that a one dimensional energy equation along the magnetic field could be used to model the electron temperature[1]:

$$\frac{3}{2}k_B n_e \frac{\partial T_e}{\partial t} = \frac{\partial}{\partial z}K_e(T_e, z, t)\frac{\partial T_e}{\partial z} + Q_{HF}(T_e, z, t) + Q_0(z, t) - L(T_e, z, t) \tag{2.5.1}$$

where K_e is the parallel thermal conductivity (that we will show later far dominates the Pedersen and Hall conductivities above 100km), Q_{HF} is the HF pump wave energy deposited to the electrons, and L is the combined electron heat loss. This works since the heat conductivity is much larger along the background magnetic field line than the perpendicular, and by assuming plasma drift and convective terms to be negligible[2]

For the Ohmic heating we take the time average of the pump-wave electric field multiplied with the induced current (Gustavsson et al., 2010):

$$Q_{HF} = \frac{1}{2}\mathbf{Re}[\mathbf{E}^* \cdot \bar{\sigma} \cdot \mathbf{E}] \tag{2.5.2}$$

where $\bar{\sigma}$ is the conductivity tensor mentioned in Equation (2.2.5).

For this study we will be looking at the energy equation from when the HF pump is turned off, therefore we will not directly be using much of the above

[1]There should be a factor $\sin^2 I$ in the gradient term in Equation (2.5.1), but as the inclination of the geomagnetic field lines is $I \approx 78^\circ$ at EISCAT, $\sin^2(78^\circ) = 0.96$ this factor was neglected.

[2]These are justifiable assumption for our experiment as the field aligned plasma drift and convective terms measured by EISCAT is found to be insignificantly small.

equations mentioned in this subsection in the analysis, but it is important to know how the heating of the pump wave can affect the ionosphere.

2.6 Electron Background Heating

For the electron background heating from natural processes we set $Q_{HF} = 0$ in Equation 2.5.1 and look at the electron energy equation for the HF off:

$$Q_0 = \frac{3}{2} k_b n_e \frac{\partial T_e}{\partial t} - \frac{\partial}{\partial z} K_e \frac{\partial T_e}{\partial z} + L \tag{2.6.1}$$

For day-time F-region conditions Q_0 is essentially obtained by equating it with the electron cooling rates L and the electron heating by photoelectron electron heating, Q_e^* (Schunk and Nagy, 1978). The photoelectron electron heating can be expressed as (Gustavsson et al., 2010)

$$Q_e^* = n_e(z) \int_{E_c}^{\inf} L_{ee}(E, z) I_e(E, z) dT \tag{2.6.2}$$

where I_e is the photoelectron flux at altitude z and energy E, and L_{ee} is the electron stopping power or loss function (Swartz et al., 1971)

$$L_{ee}(E) = \frac{3.37 \cdot 10^{-12}}{E^{0.94} n_e^{0.03}} \left(\frac{E - E_e}{E - 0.54 E_e} \right)^{2.36} \text{eVcm}^2 \tag{2.6.3}$$

where E_e is the electron temperature in units of eV.

Later in chapter 3.1 we will show how we derive plasma parameters e.g. electron density and temperature from ISR, and these parameters we will use in our study for the analytical equations above to calculate the background heating Q_0, electron energy loss and the electron energy equation.

2.7 Thermal conductivity

The thermal conductivity, K_e, in Equation 2.5.1 and 2.6.1 was estimated as (Rees and Roble, 1975):

$$\begin{aligned}
Q_1 =& 2.82 \cdot 10^{-17} T_e^{1/2} - 3.41 \cdot 10^{-21} T_e^{3/2} \\
Q_2 =& 2.2 \cdot 10^{-16} + 7.92 \cdot 10^{-18} T_e^{1/2} \\
Q_3 =& 3.2 \cdot 10^{-16} \\
Q_4 =& 5.6 \cdot 10^{-16} \\
Q_5 =& 5.47 \cdot 10^{-15} - 7.45 \cdot 10^{-19} T_e
\end{aligned}$$

$$K = \frac{7.75 \cdot 10^{-5} T_e^{2.5}}{1 + 3.22 \cdot 10^4 \frac{T_e^2}{n_e} \left(Q_1[N_2] + Q_2[O_2] + Q_3[O] + Q_4[H_e] + Q_5[H]\right)} \quad (2.7.1)$$

where the densities are expressed in cm^{-3}

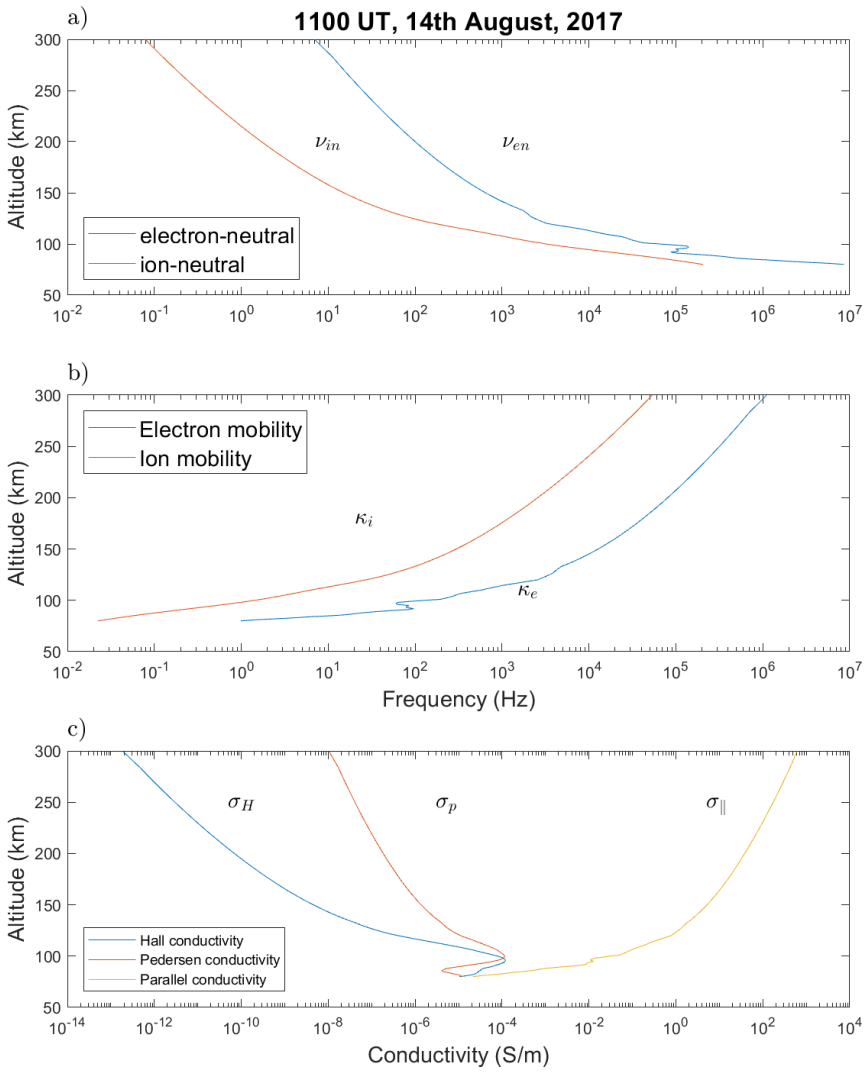

Figure 2.3: Typical altitude profiles over auroral and polar latitudes such as Tromsø, Norway. a) Shows the ion-neutral and electron-neutral collision frequencies, ν_{in} and ν_{en}, b) ion and electron mobility (Ω/ν), and c) altitude profiles of the Pedersens, Hall and parallel conductivities derived for the ionosphere above EISCAT Tromsø 14th of August 2017.

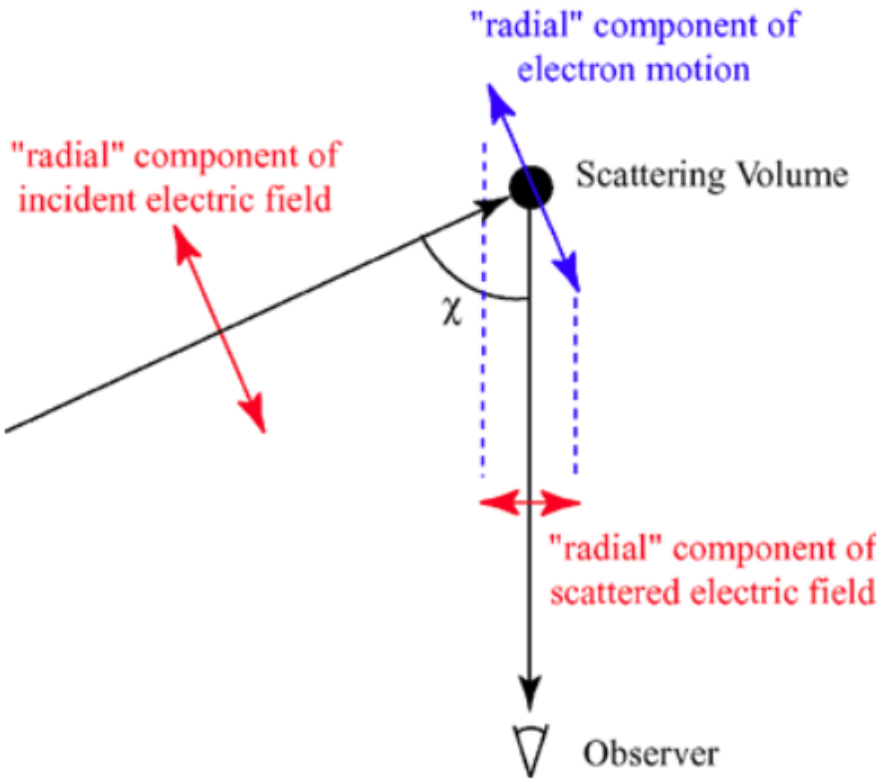

Figure 2.4: Thomson scattering for a bistatic system with scattering off a plasma volume with an incident and scattered angle difference χ. The blue arrows shows the directions of oscillation by the volume as a result of the radial electric field component of the incident wave (Illustration from Wikipedia (2004)).

Chapter 3

Instruments and models for upper atmosphere observation and prediction

In this chapter we will describe the working principles of two radio probing instruments: ISR (in particular the EISCAT radar) and ionosondes, as well as two ionospheric models: the MSIS model and international Reference Ionosphere (IRI) model, that we will use in this study to estimate the plasma parameters and the ionospheric condition for the days of the experiments.

3.1 Incoherent Scatter Radars - EISCAT

In this section we will only cover the most important concepts of how ISR such as the EISCAT radar works and how we derive the plasma parameters from the received backscattered signals.

In section 2.3 we described incoherent scattering (IS) and the scattering mechanism, as well as some of the important restrictions on the probing wavelength to get backscatter off the collective behaviour of the electrons. From this backscatter we measure the signal as a time-series of voltage with frequency on the order of the transmitter frequency (for the EISCAT Tromsø system: 224MHz and 930MHz for the VHF and UHF, respectively) and this is then brought down to baseband —centred around 0, with ion and electron frequency ranges— for simpler and faster sampling for the analogue to digital (AD) converter.
When analysing the received signal we want to be able to distinguish between different height regions, and with an as good range resolution as possible to resolve smaller scale structures. To achieve this the EISCAT radars transmit alternating codes (Lehtinen and Häggström, 1987; Wannberg, 1993), where the

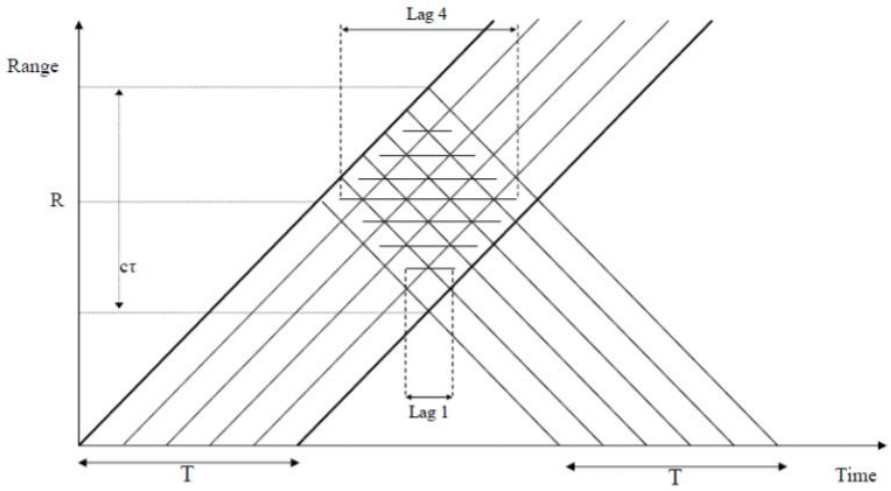

Figure 3.1: A range-time diagram, the pulse lasts for T units of time and is split into 5 subpulses. This diagram shows how the transmitted and received pulse is split to distinguish between ranges, here making 7 different range gates. Only the backscattered waves that reaches the antenna during the sampling time gets measured, therefore the altitude region measured is the overlapping volume as seen in this diagram. (Figure from lecture notes at the University Centre in Svalbard)

transmitted pulses are divided into continuous sequence of subpulses that each has a phase of either 0 or 180° (1 or -1) that are predetermined based on the number of subpulses in a pulse. The selection of phase modulation (or pulse coding) are made so that after a set of transmitted pulses the backscatter from regions separated by the length of a subpulse can be separated i.e. all ambiguities cancels after exactly one complete scan, splitting the backscattered signal into many distinguishable range gates.

Figure 3.1 shows the time-range diagram of a pulse split into five subpulses. These five subpulses are then scattered off all the heights in the ionosphere and then sampled at some time Δt later with a sampling code applied to the sampling interval (just like the subpulses in the pulse, the sampling applies five phases to the received signal as illustrated in figure 3.1), and from this a lag profile matrix is made. The lag profile matrix is created from the second order product between the received signal sampled at a fixed time period, and then shifted by one lag at a time. Many such lag profiles are made before the ensemble average of all the different realisations of a set time period is used to create the auto correlation function (ACF).
Nowadays alternating codes are the standard measurement technique in all ISR observations, and higher resolutions can be achieved by sampling with fractional lags (oversampling) (Huuskonen et al., 1996), however increasing range

resolution (smaller subpulses) will reduce the SNR as for every height region the scattering volume will become smaller, and it will also take longer for the cancellation property in the alternating code to complete and therefore reducing the possible peak time resolution.

After obtaining the ACF it is then Fourier transformed from the time-lag domain to produce the *power density spectrum* (PDS), and from the PDS we can derive most of the plasma parameters, e.g. neutral density, electron and ion temperature, ion velocity.

For deriving the plasma parameters we need to study the plasma in the kinetic description. We have two main types of models for describing the physics of plasmas: the fluid description and the kinetic description, where the fluid description looks at the plasma as fluids with a sequence of conservation equations and not on the individual particles. The fluid description is a fairly simple approach, and adequate in many cases, however some phenomena requires the velocity distribution of the particles to be considered. One of these phenomena is Landau damping, where the particles moving slightly faster than the phase velocity of the wave on average gives energy to the wave, while the particles slower receives energy from the wave, see figure 3.2. As the velocity distribution of the electrons in the plasma is typically is Maxwellian distributed, more particles are gaining energy from the wave, and therefore the wave has a net energy loss and is being damped, this damping of the plasma waves is what is known as Landau damping.
If we were to use the fluid description, the ion spectrum would not be damped, and it would only be single spikes at the locations of the ion lines.

Under the assumption that the wave has sinusoidal behaviour, its time variations can be expressed as:

$$e^{-i\omega t} = e^{i\omega_r t} e^{\omega_i t}$$

For the ion acoustic wave in the kinetic description the real and the complex wave frequencies are:

$$\omega_i = \omega_{i,r} + i\omega_{i,i}$$

$$\omega_{i,r} = \frac{k c_s}{1 + k^2 \lambda_D^2} \tag{3.1.1a}$$

$$\omega_{i,i} = -\sqrt{\frac{\pi}{8}} \frac{\omega_{i,r}}{(1 + k^2\lambda_D^2)^{3/2}} \left(\left(\frac{T_e}{T_i} \right)^{3/2} \exp\left[-\frac{T_e/T_i}{2(1 + k^2\lambda_D)} + \sqrt{\frac{m_e}{m_i}} \right] \right) \tag{3.1.1b}$$

$$c_s = \left(\frac{k_B T_e + 3 k_B T_i}{m_i + m_e} \right)^{1/2} \tag{3.1.1c}$$

Where c_s is the speed of sound in the medium, k the wave number and λ_D

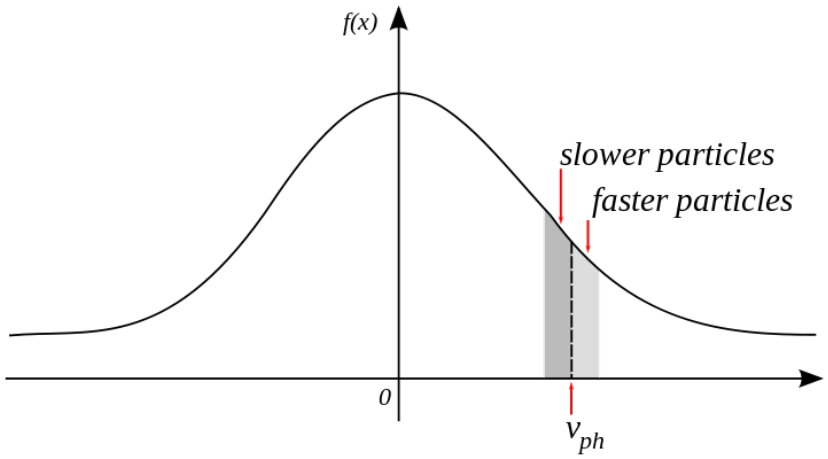

Figure 3.2: Figure showing the velocity distribution of ions in a plasma and the phase velocity of the wave, v_{ph}. As there are more particles with a velocity slower than the phase velocity in the wave, the wave will have a net loss of energy—this being the landau damping of the wave (figure from Wikipedia (2010)).

is the Debye radius that we touched upon in chapter 2.1.2:

$$\frac{1}{\lambda_D^2} = \frac{1}{\lambda_e^2} + \frac{1}{\lambda_i^2}$$
$$\lambda_{e,i} = \sqrt{\frac{\epsilon_0 k_B T_{e,i}}{n_0 e^2}}$$

For the electron plasma waves we have the angular wave frequencies:

$$\omega_{e,r} = \left(\omega_{pe}^2 + k^2\lambda_D^2\right)^{1/2} \tag{3.1.2a}$$
$$w_{e,i} = -\,C \cdot \frac{\omega_{pe}}{k^2\lambda_D} \exp\left(\frac{-1}{2k^2\lambda_D^2}\right) \tag{3.1.2b}$$

where C is a constant. In the case of weak landau damping, $k^2\lambda_D^2 \ll 1$, the dominating term in the complex ion acoustic frequency expression (equation 3.1.1b) will be the T_e/T_i:

$$\omega_{i,i} \propto \left(\frac{T_e}{T_i}\right)^{3/2} \exp\left(-\frac{Te}{T_i}\right)$$

therefore from the valley in the ion line spectrum (see figure 3.3) we can retrieve information about the T_e/T_i ratio.

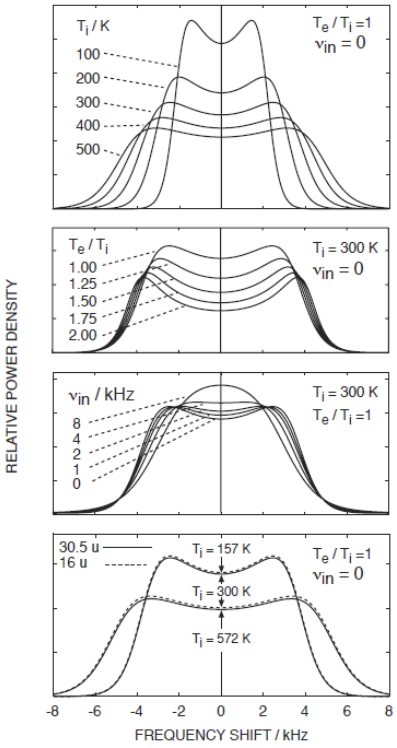

Figure 3.3: Illustration of the power density spectrum from the analysed EISCAT data for one range gate, showing the dependence on the shape of the ion line to the plasma parameters (Nygrén, 1996)

The drift velocity of the plasma, v_i, is found from the Doppler shift of the backscattered signal. The change in frequency due to the Doppler shift is:

$$\omega_d = \left(\frac{c + v_i}{c}\right)\omega_0$$

$$v_i = c \cdot \frac{\omega_d - \omega_0}{\omega_0} = c \cdot \frac{\Delta\omega}{\omega_0}$$

where c is the speed of light[1], ω_0 is the radar frequency and ω_d is the observed Doppler shifted frequency.

The ion acoustic frequency is found from the two peaks of the ion spectrum, and is directly linked to Equation 3.1.1a. For weak landau damping Equation

[1]Now this is not exactly the case, the wave will travel ever so slightly slower than the speed of light, but as the refractive index of the air and gases in the ionosphere is extremely close to one, we will assume that the EM wave travels at the speed of light. And for any statistical purpose the deviation in our measurements will be many orders of magnitude higher than the error inflicted by this approximation.

3.1.1a becomes:

$$\omega_{i,r} = k\left(\frac{k_B T_e + 3k_B T_i}{m_i + m_e}\right)^{1/2}$$

and as $m_i \gg m_e$, and for most of the ionosphere $T_e \gg T_i$, this can be used to find information about the ratio T_i/m_i, visible from the full width half maximum (FWHM) of the ion lines in the PDS.

For every backscattered wave there is an electron there to radiate it, therefore we can obtain information about the total electron density from the area underneath the ion line spectrum, or simply to integrate over all the received ion frequencies. A second way to find the electron density from the PDS is from the location of the plasma lines —as we remember from section 3.2 the electron density is directly related to the plasma frequency— but these are often harder to find as they are very narrow and located at frequency offsets at the order of MHz from the ion-line.

3.2 Ionosondes

The most straightforward way to map the electron density in the ionosphere is by the use of an ionosonde (Judd, 1987). An EM wave cannot propagate into regions where the plasma-frequency is higher than the wave-frequency, and the same goes for the ionosphere. The plasma frequency is:

$$\omega_{pe} = \sqrt{\frac{e^2 n_e}{m_e \epsilon_0}} \tag{3.2.1}$$

where e, n_e, m_e, ϵ_0 is the electron charge, electron density, electron mass and permittivity in vacuum, respectively. The plasma frequency is the oscillation of the electrons in the plasma, and as all terms except for n_e is constant it shows a direct relation between the plasma frequency and the electron density.
An ionosonde has three main parts: A HF transmitter, a tracking HF receiver that tracks the frequency of the transmitter, and an antenna to measure the reflected signal. In the ionosphere the plasma frequency is usually in the order of a few MHz, and as the ionsonde transmits pulses at steadily increasing frequency in the range 0.5MHz to ∼23MHz, the signal propagates up until it reaches the height where the plasma density corresponds to a plasma frequency equal to the wave frequency, where it simply is reflected back in all directions, the ionosonde then receives some of this backscatter that it uses to measure the time Δt it took the wave to reach the plasma and back, and from this and Equation (3.2.1) one can easily obtain a height profile of the electron density.

Depending on the polarization of the wave the reflected signal is split into ordinary (O) and extraordinary (X) modes. The O mode is the part of the signal that gets reflected from the altitude with matching plasma frequency,

while the X-modes gets reflected from the x-mode cut off frequency. The lower-hybrid and upper-hybrid frequencies are the plasma oscillation with or against the cyclotron frequencies:

$$O - \text{mode} = \omega_{pe} \tag{3.2.2a}$$

$$X_1 - \text{mode} = \omega_{pe} + \Omega_e = \sqrt{\frac{e^2 n_e}{m_e \epsilon_0}} + \frac{eB}{m_e} \tag{3.2.2b}$$

$$X_2 - \text{mode} = \omega_{pe} + \Omega_e = \sqrt{\frac{e^2 n_e}{m_e \epsilon_0}} - \frac{eB}{m_e} \tag{3.2.2c}$$

For mapping of the ionospheric electron density the O-mode trace is used. We won't be going much further into the X-mode reflections, but they're worth mentioning as they do give clear reflected signatures in the ionograms, and they can play an important role in plasma heating from the HF pump mentioned in section 2.5 as the pump wave (O-mode) splits into UH wave (X-mode) in the vicinity of the UH resonance level where the electric field of the UH wave can reinforce FAI.

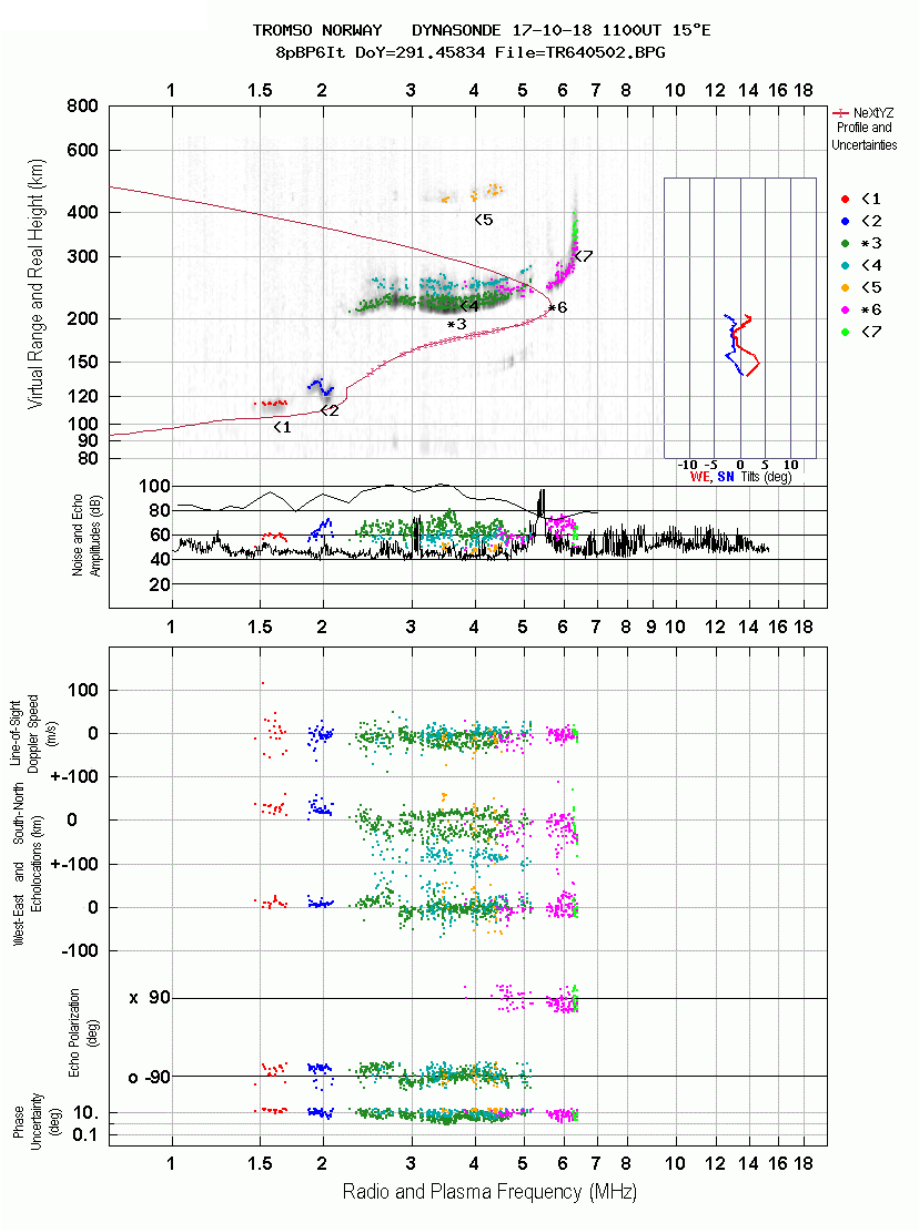

Figure 3.4: Ionogram from 18th of October from the EISCAT Dynasonde (see Rietveld et al., 2008). The plot shows the foF2 at 5.662MHz. The green locus shows the O-mode reflections, and the purple is the X-mode reflections, with the numbers indicating the virtual range. The red line indicates the calculated plasma frequency at that altitude.

3.3 Empirical model for upper atmospheric composition

It can be difficulty to directly measure the neutral density in the ionosphere—and even more so for each atmospheric component—we are therefore reliant on models based on data from compiled decades of observations and experiments. The two models we are using in this study is the MSIS model, and the IRI model. Having reliable information about how the ionospheric components changes with variations in location, solar activity, time of year, magnetic local time (MLT) etc. is important for the research community studying the upper atmosphere, space missions operations and not least space mission design, just to mention a few of the fields.

3.3.1 Mass Spectrometer Incoherent Scatter model

The MSIS empirical model (Hedin, 1987) have been the choice for background statistical estimates regarding the expected neutral density and temperature of the thermosphere for upper atmospheric scientist for decades. Many improvements has been made to better estimate the neutral parameters since the model was first introduced (Hedin, 1991; Picone et al., 2002). The computed values from MSIS is thought to be very close to the true value in a statistical sense, but for any given day the model densities might deviate significantly (with even a factor of 2) from the actual densities.
For the model to make the estimate of the neutral density it bases it on empirical studies from ISR, drag measured by accelerometers on-board in situ satellites such as the low-earth polar orbiting CHAMP satellite (Reigber et al., 2002) and of many previous rocket flight measurements.

For data on the neutral density composition mass spectrometers on-board satellites has been used to scan the composition in the thermosphere under many different ionospheric conditions (Hedin et al., 1977; Hedin, 1989), looking for absorption signatures from the elements in the ionosphere. These lines do not change for the vibrationally unexcited and vibrationally excited molecules, making it impossible for mass spectrometry to differential between the unexcited and vibrationally excited population of N_2 mentioned in chapter 2.4.

The MSIS model gives us information about the following thermospheric parameters in between 60 to 1000 km altitude:

- Neutral temperature, T_n
- Total mass density
- Density of He
- Density of Ar
- Density of H

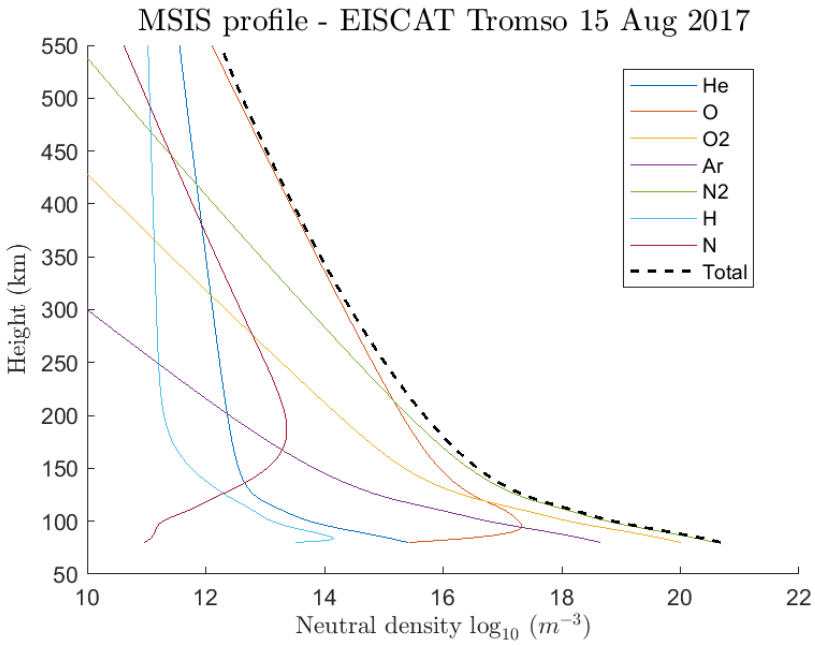

Figure 3.5: Computed MSIS neutral densities using the atmosnrlrmsis function from MatLab's Aerospace Toolbox for Tromsø 15th August 2017. Here with F10.7 cm flux = 70 sfu, and AP = 4.

- Density of O
- Density of N_2
- Density of O_2
- Density of N
- Anomalous oxygen number density

The MSIS model we will be using in this study is provided by MatLab Aerospace toolbox, NRLMSISE-00.

3.3.2 International Reference Ionosphere

For information about the different ion species in the ionosphere we will be using data from IRI (Rawer et al., 1978; Bilitza et al., 1990). The IRI project started in 1969 as a joint project of International Union of Radio Science (URSI) and Committee on Space Research (COSPAR), and has been storing data from ionosondes all over the world for the ionosphere peak density (NmF2) and ionosphere total electron content (TEC) under varying ionospheric conditions and geographic locations. It also used data from the incoherent scatter measurements to map the electron temperature, ion temperature and the ion density, and for more extensive results of the electron density at these locations, as well as data from in situ satellite and rocket measurements to achieve an as good

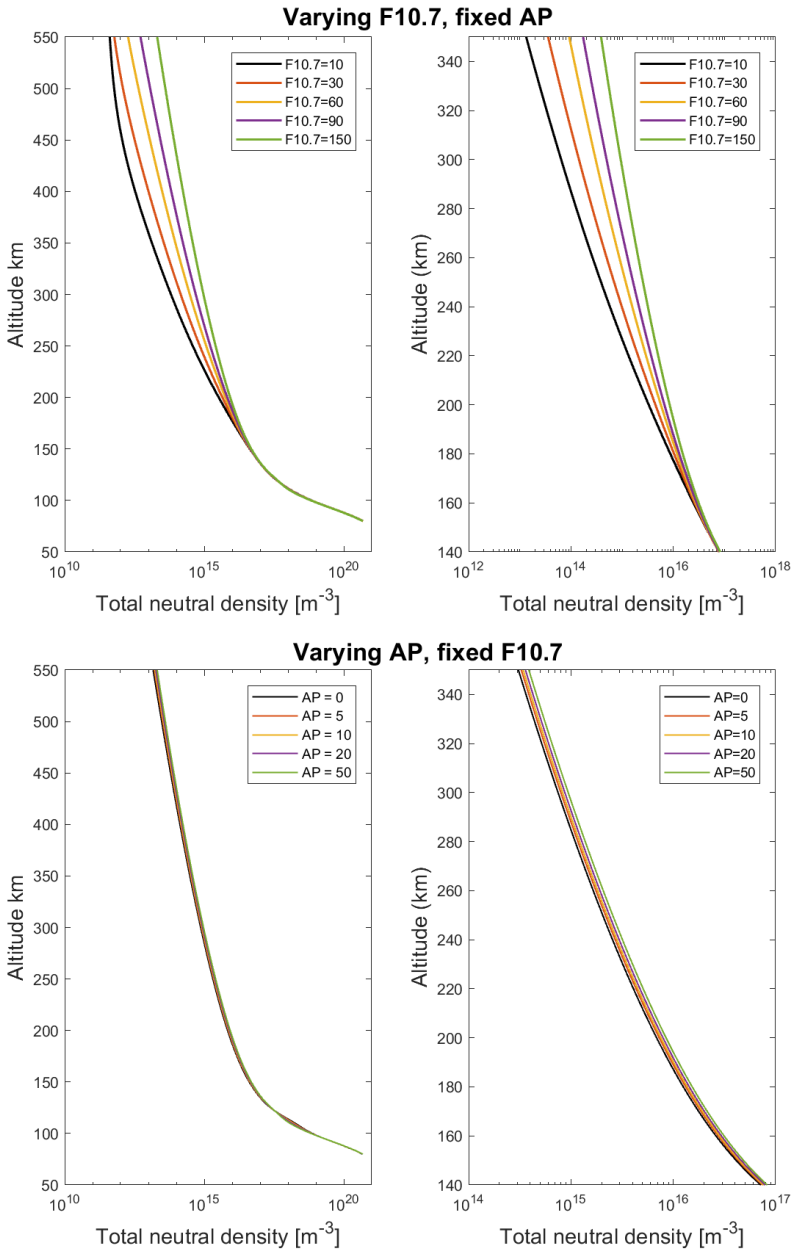

Figure 3.6: Computed neutral densities using the MSIS model for the 18th of October with fixed and varying F10.7 and AP values. Both show that the MSIS neutral density estimate increase with increasing solar EUV fluxes, but that it is much more prone to changes in the F10.7 flux than to the AP index. The top panels were computed using AP = 4, and bottom panels using F10.7 = 70.

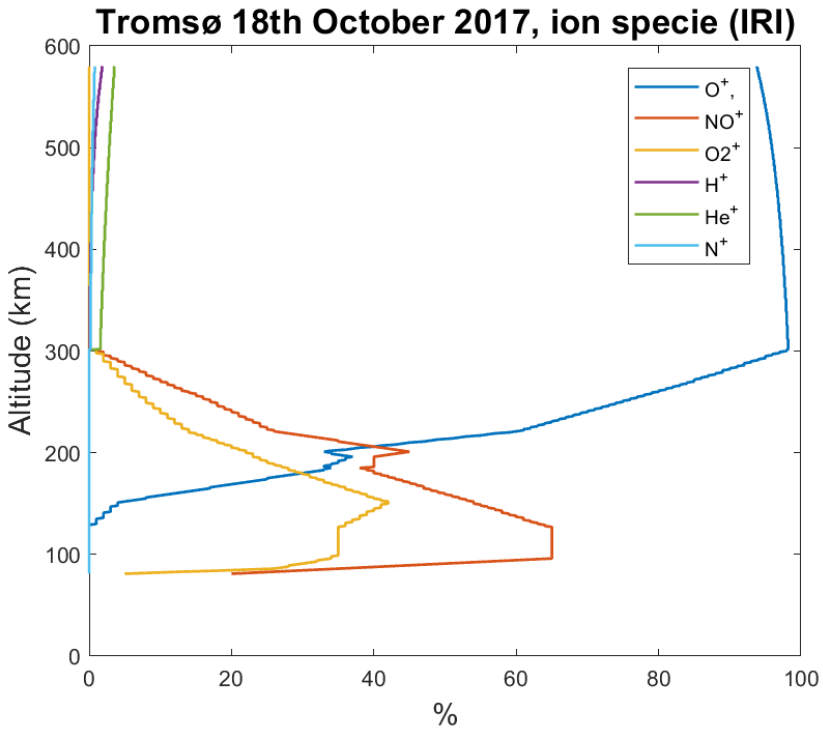

Figure 3.7: Ion fraction (in percentage) over Tromsø as estimated by IRI for the 18th of October 2017. At lower altitudes the ionized molecular oxygen and nitrogen oxide dominates, with a transition to atomic oxygen at approximately 230 km altitude(just above the F2 peak density).

reference ionosphere as possible.

IRI provides the following parameters:

- Ion temperature
- Electron temperature
- Electron density
- Density of O^+
- Ionospheric electron content
- Density of H^+
- Density of Ne^+
- Density of NO^+
- Density of O^+_2
- F peak and spread probabilities

Chapter 4

Experiment and Observations

In this chapter we will discuss the pre-analysed ISR-data from the days of the experiments and then present the method utilized in finding the most-likely MSIS parameters that was used to estimate the thermospheric neutral densities.

We collected data using EISCAT (Du Castel and Testud, 1974; Rishbeth and Williams, 1985; Folkestad et al., 1983). The experiment and observations were conducted between 10 and 12 UT (universal time, local time -1) the 14th and 15th of August 2017 using the ultra high frequency (UHF) radar. The UHF radar was pointing field aligned and we used the EISCAT Heating facility (Rietveld et al., 1993) to heat the electrons in the $180 - 240$km altitude, the EISCAT Heating was operating in a 3 minute on 3 minutes off cycle period transmitting at 4.40 MHz.
On the 18th of October the heating experiment was conducted again, but with the HF pump wave on for 120 seconds followed by 330 seconds off, and with an initial frequency of 5.50 MHz that every 10th second reduced by 20kHz, ending at 5.30 MHz before HF off.

4.1 Weather and ionospheric conditions

The weather conditions were 10°C the 14th of August, and slightly colder at about 8°C the 15th of August, with little to no rain either days. The ionospheric conditions were quiet, with the Deep Space Climate Observatory (DSCOVR) satellite (Yang et al., 2013) reporting positive IMF B_z for the 14th and 15th of August, indicating small energy transfer from the solar wind into the magnetosphere, therefore no loading of the Earth's magnetic tail and little to no electron precipitation into the ionosphere (Brautigam et al., 1991).
For the 18th of October the IMF B_z was slightly negative with proton velocities and densities reported at 350 km/s and 4.5 cm^{-3}, respectively. Some loading

Figure 4.1: Data on the B_z component of the IMF at the 1st Lagrange point between the Sun and Earth measured by DSCOVR for the times of the experiments. Slightly negative B_z on the 18th of October for the hours before and during the first half of the heating experiment. A few hours before the experiment is included as it may take the ionosphere one to three hours (depending on solar wind speed and convection velocity over the polar cap) to react to the IMF measured at L1.

of the magnetospheric tail and electron precipitation in the region around the open-closed field-line boundary was expected, but as EISCAT Tromsø is located equatorward of the cusp during daytime hours this slight southward B_z should have negligible influence on the local ionosphere. Figure 4.1 shows the B_z component of the IMF for the 15th of August and 18th of October a few hours before and during the experiments.

The reported F10.7 and AP values from Space Weather Prediction Center (SWPC) can be seen in Table 4.1; all three days had quiet ionospheric conditions.

Table 4.1: Daily solar EUV values from SWPC

Date	F10.7	AP
14 August	68	4
15 August	68	3
18 October	70	4

4.2 Estimating collision frequency and conductivities in the ionosphere

We estimated the altitude profiles of the electron-neutral and ion-neutral collision frequencies and then derived the conductivities on the dates of the experiments.

For the electron-neutral collisions we used the model by (Nicolet, 1953), looking at the region where N_2 and O_2 dominates (see figure 3.5):

$$\nu_{en} = 5.4 \cdot 10^{-16} n_n \cdot T_e^{1/2}.$$

where ν_{en} and n_n is the electron neutral collision frequency and neutral density. For the ion-neutral collision frequency we applied a method known from literature:

$$\nu_{in} = k_{N_2} \cdot [N_2] + k_{O_2} \cdot [O_2] + k_O \cdot [O]$$

where k_{N_2}, k_{O_2} and k_O are the collision rates according to the neutral and ionized species involved, and the bracket denotes the number density of that neutral specie (Brekke, 2013). The collision rate coefficients obtained from (Kunitake and Schlegel, 1991) for an average ion mass number of 30.7 can be found in Table 4.2

Table 4.2: Collision rate coefficients for N_2, O_2 and O $[m^3/s]$

k_{N_2}	k_{O_2}	k_O
$4.34 \cdot 10^{-16}$	$4.28 \cdot 10^{-16}$	$4.44 \cdot 10^{-16}$

For the data taken on August 15, 2017 the calculated mobilities and conductivities can be seen in Figure 4.2. The neutral density constituents was taken from atmosnrlmsise00 model in MatLab, with input parameters for EISCAT Tromsø and the 10.7cm flux being estimated to 68 sfu and $AP = 6$ for the given day.

We got very typical values for both the collision frequencies and the conductivities over Tromsø for quiet ionospheric conditions, as can be seen in figure 4.2. The electron mobility (ratio of gyrofrequency to neutral collision frequency)

indicates it is in the EM domain at virtually all heights, while the ions transitions from being heavily influenced by the neutrals at approximately 120 km. Figure 4.2 shows that the parallel conductivity dominates above the D regio , as is excepted and has been one of our assumptions for many of the analytical expressions of the electron energy transfers in chapter 2.4.

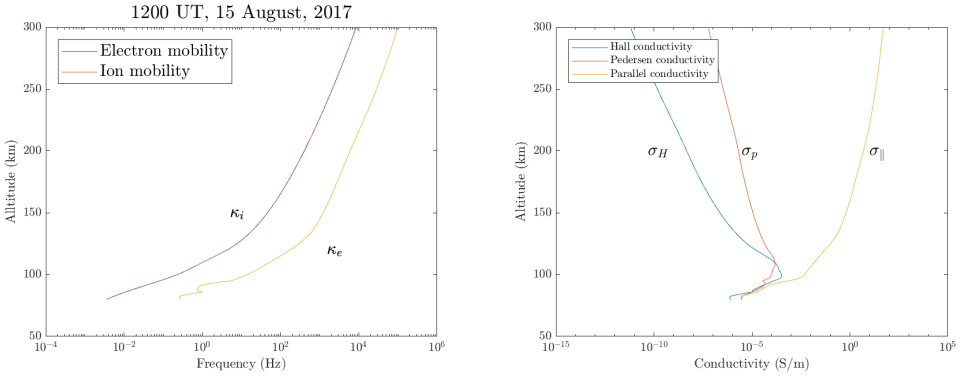

Figure 4.2: Altitude profiles of the electron and ion mobility and conductivities derived from EISCAT Tromsø at 12:00 UT on August 15, 2017. In the top figure κ_i transitions approximately at 120 km, while the electrons are dominated by electromagnetic influence at virtually all measured heights. The first perturbation in the electron κ_e is due to high spread and bad SNR in the measured T_e at the lower altitudes.

We estimated the absorption in the D region and lower F region at the days of the experiment, as will be seen very varying electron heating was achieved on the different days. We estimated this as

$$K = \frac{q_e^2}{z\epsilon_0 m_e c} \cdot \frac{1}{\mu} \int_{80\text{km}}^{150\text{km}} \frac{n_e \nu_{en}}{\nu_{en}^2 + (\omega_{HF} \pm \omega_g)^2} dz \tag{4.2.1}$$

which gives an estimate of the absorption in the lower region between $80 - 150$ km in dB.

4.3 Experiment mode

The EISCAT facility has many standard experiment programs that has been optimized to allow the user to look at specific structures of the ionosphere, such as to allow for collection of the plasma line data as well as the standard ion line data, or to allow the antenna to scan the sky while observing. For additional technical details see (Folkestad et al., 1983).
We ran the experiment mode beata, it uses a 32 bit alternating code with 20µs subpulses. In table 4.3 the properties of the beata mode is listed for both the

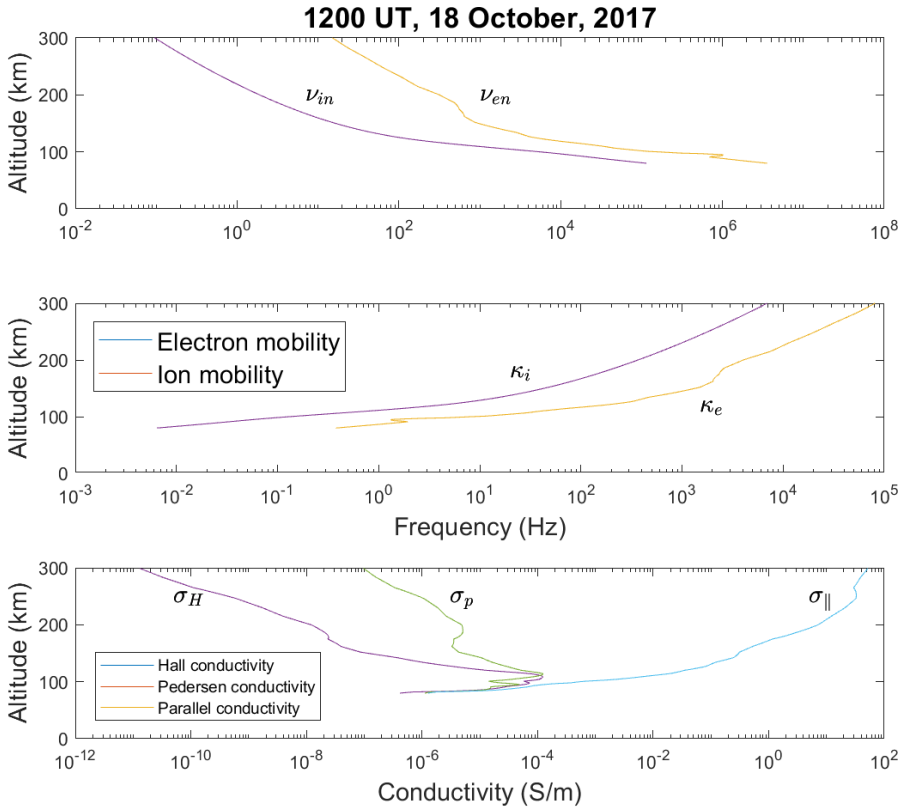

Figure 4.3: Estimated collision frequency, mobility and conductivities over EISCAT Tromsø the 18th of October at the time of our experiment.

UHF and the very high frequency (VHF). The beata experiment at EISCAT has tristatic support, although for this study we only used the UHF radar.

Table 4.3: Beata experiment properties

Radar	Code length (bit)	Baud length (µs)	Sampling rate (µs)	Range span (km)	Time resolution (s)	Plasma line	Raw data
UHF	32	20	10	49 – 693	5	Yes	–
VHF	32	20	20	52 – 663	5	Yes	–

In addition we used the Common Program 1 (CP1), this is the program of choice for a fixed transmitting antenna pointing along the geomagnetic field

lines (78° inclination).

4.4 Estimates of ionospheric parameters

The radar data was analysed using the Grand Unified Incoherent Scatter Design and Analysis Package (GUISDAP) (Lehtinen and Huuskonen, 1996; Lehtinen et al., 1997). We analysed the data with 5 second integrations (no overlapping time integrations — this for best possible temporal resolution) with no range gating. Due to the low number of time integrations, there are points where there is not sufficient SNR, and hence missing data points. The GUISDAP analysed data can be seen in figure 4.4 for the electron density, electron temperature and ion temperature. The data received on the 14th had almost no electron heating and could not be used for this study. The data from the 15th and 18th achieved significantly higher electron heating and is what we have based the rest of the analysis on. A calibration was done for the data received on the 18th of October that compared the electron density from the ion line spectrum to the plasma lines, this showed that the plasma lines was found at a greater frequency than what indicated by the ion line spectrum alone, resulting in a scaling of the electron density by a factor 1.22.

The GUISDAP analysed data was then preprocessed into Heating-cycles covering one HF on and one HF off period, this simply to make the bookkeeping easier when modelling the electron temperature for each cycle.

In figure 4.5 data for the 18th of October is plotted after being preprocessed. a) and d) shows the 23rd range gate (216 km altitude) for all the cycles, and as can be seen GUISDAP has rejected a lot of data points shortly after HF_{on} which is likely due to the HF-modification creating all kind of anomalous effects in the ionosphere. This does not inflict with our study as we are only interested in the temperature after HF_{off} and the following two minutes when the electrons cool down to the background temperature, this time period we will call the relaxation window.

Some data points were also missing within the relaxation window for the 7th and 11th cycle on the 18th of October. Analysing the raw data using GUISDAPs analysis control to increase the allowed number of iterations (allowing GUISDAP more iterations to fit the data to a model set of plasma parameters for these times) was done, but to no success.

For the 15th of August there was also some bad data integrations as can be seen in figure 4.6. In the relaxation window of the 1st, 4th, 5th and 11th cycle abnormal electron temperatures were observed that makes the background heating artificially high, therefore these cycles were excluded from further analysis.

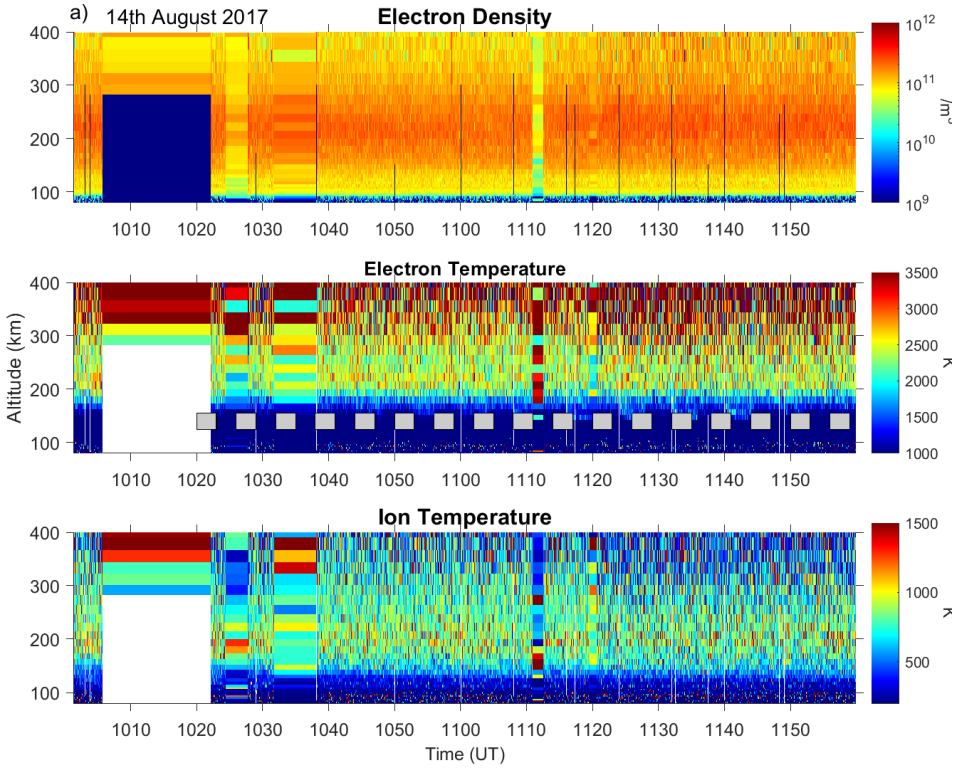
a) 14th August 2017
Electron Density
Electron Temperature
Ion Temperature
Altitude (km)
Time (UT)
K
m^-3

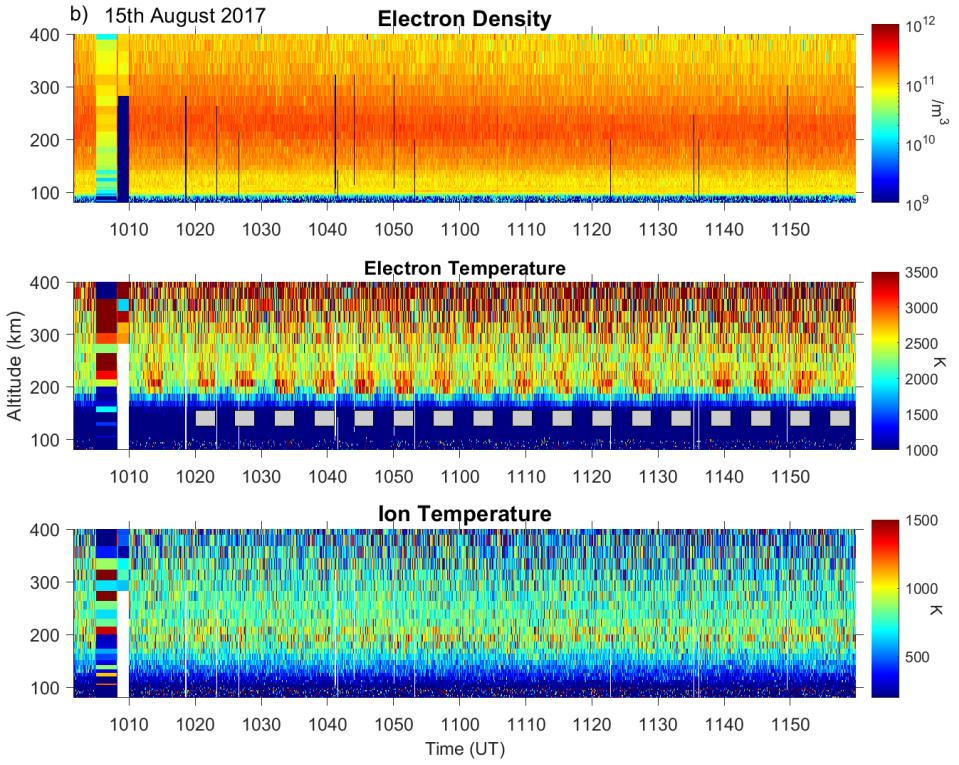
b) 15th August 2017
Electron Density
Electron Temperature
Ion Temperature
Altitude (km)
Time (UT)
K
m^-3

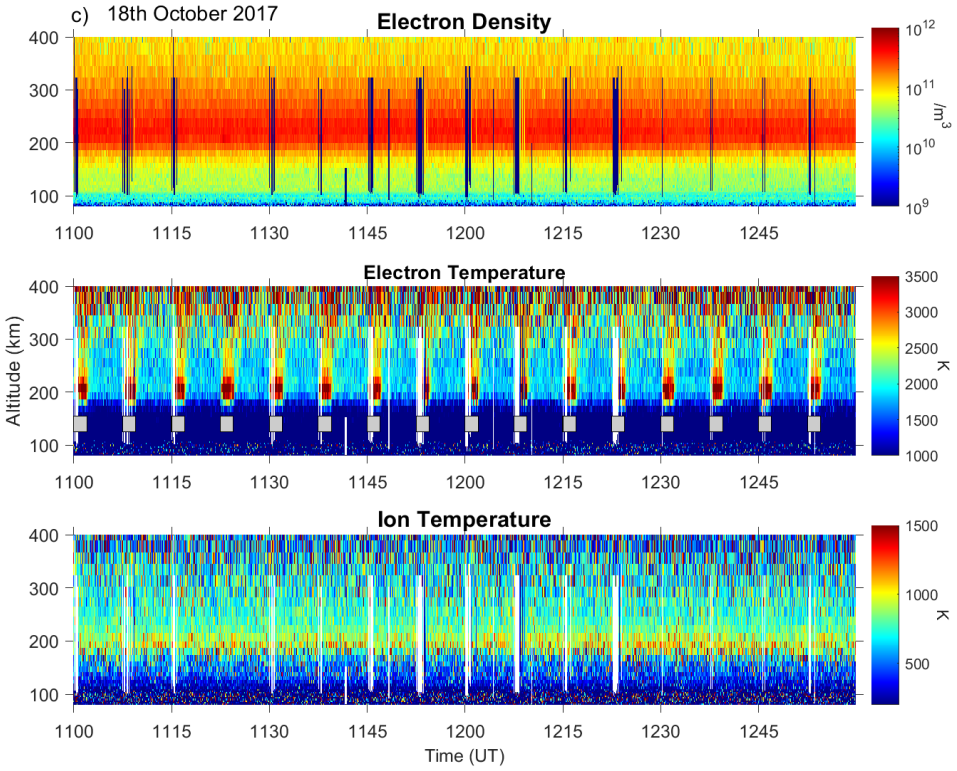

Figure 4.4: The electron density, electron temperature and ion temperature on the times of the heating experiment. Good electron heating was achieved in both *b* and *c*, but for *a* very little energy from the HF beam was deposited in the ionosphere and almost no electron heating was observed. The grey bars in the electron temperature plots indicate when the HF beam was turned on. The NmF2 was also slightly lower in *a* than in *b* and significantly lower than in *c*, and being both higher and more concentrated in *c* than *a* and *b*. At the early hours of the experiment in both *a* and *b* we had issues with the UHF transmitter, therefore whites and splashes are shown at the start. The electron density in the E and D region are also significantly higher on the 14th and 15th of August in comparison to the 18th of October, therefore less of the pump wave was absorbed at lower altitudes in the October experiment.

4.4.1 EISCAT, MSIS and IRI parameters

The EISCAT derived plasma parameters that we need for the analysis is:

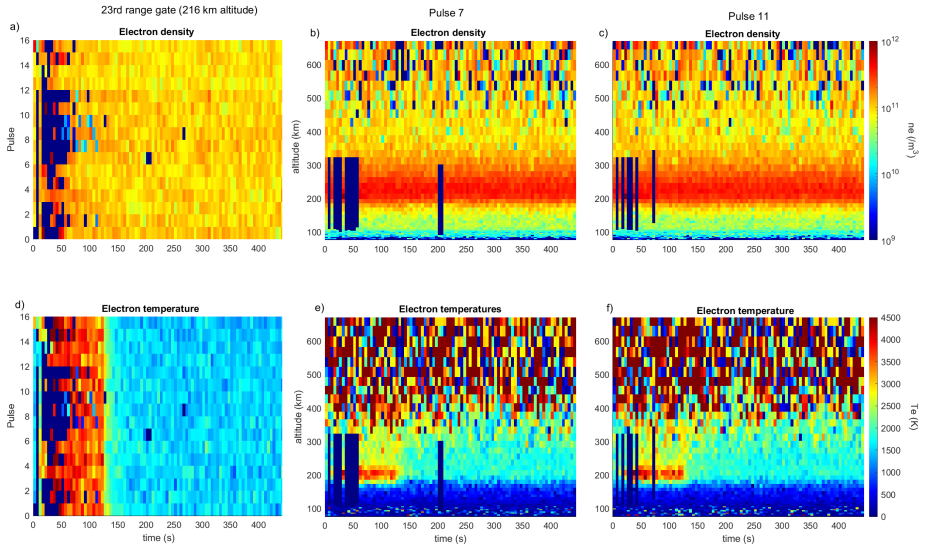

Figure 4.5: EISCAT data from the 18th. a) and d) shows the electron density and electron temperature from the range gate at 216 km altitude for all the cycles. Figure b) and e) shows electron density and temperature, respectively, for the 7th cycle. Bad data points observer about 200 seconds into the cycle, this caused errors in our later computations for this cycle as it is in the relaxation window we are studying. Figure c) and f) shows cycle 11, here as with cycle 7 a lot of bad data points during the HF on, but with no bad points for the relaxation window following HF_{off} (when the HF pump was turned off), therefore one of many good cycles for this study.

- Electron temperature
- Electron density
- Errors in electron temperature
- Ion temperature
- Error in ion temperature
- Errors in electron density

From the MSIS we used:

- Neutral temperature
- Density of O_2
- Density of He
- Density of O
- Density of N_2
- Density of H

The contribution to the heat equation from the other neutral densities are insignificant[1]. Atomic oxygen, molecular nitrogen and molecular oxygen are the

[1] N, H and H_e also have much lower densities than the three others constituents, and therefore only plays a minor role.

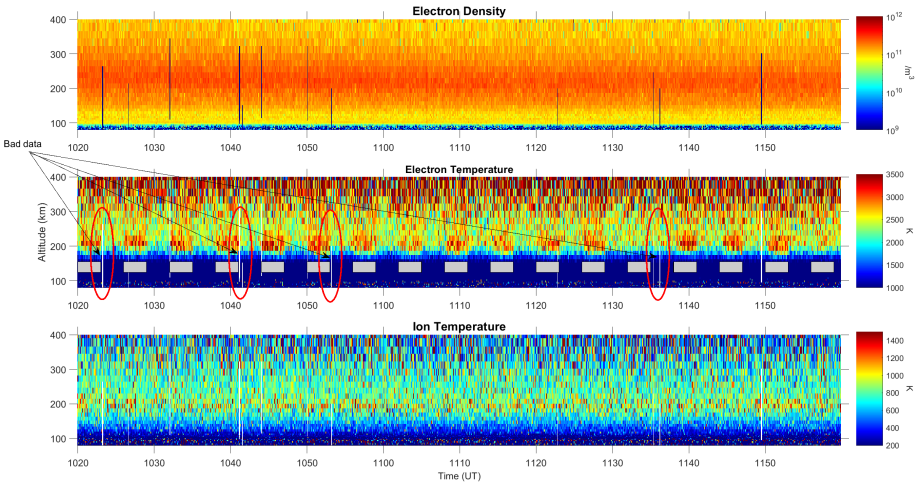

Figure 4.6: Overview plot of the GUISDAP analysed data from the 15th of August, analysed with 5 seconds integrations, showing the electron density n_e, electron temperature T_e and ion temperature T_i. The grey boxes indicate when the HF beam was on. For cycle 1, 4, 5 and 13, there was inadequate data points shortly after HF_{off} (indicated by red markers), where the electrons reached unnaturally high temperatures with equally high standard deviation.

dominating constituents of the ionosphere at the height region we are studying, as can be seen in figure 3.5.

From the IRI model we use:

- Density of O^+
- Density of H^+
- Density of $O_2{}^+$
- Density of He^+
- Density of NO^+

4.4.2 Background temperature and heating

The EISCAT background parameters was calculated from the 10 last integrations *before* next HF_{on} for each cycle, at this time the electron temperature is assumed to be in a steady state and all the energy from the HF pump has been transferred from the electrons to the ions & neutrals. These parameters represent the unperturbed ionospheric state for that cycle.

We then make a first estimated of the background heating from the EISCAT background parameters and the MSIS and IRI modelled parameters for the observation days using equation (2.6.1) under the assumption of steady-state:

$$Q_0 = -\frac{\partial}{\partial z} K_e \frac{\partial T_e}{\partial z} + L \tag{4.4.1}$$

Figure 4.7 shows the estimated background heating for the 15th of August and 18th of October, where the estimate shows good agreement to the neutral density in the spread and variation of the background heating, but overestimates the amplitude of the 15th of August relative to the 18th of October, as there are significantly more electrons at hmF2 for the 18th of October. This estimate is prone to uncertainties as it is directly calculated using the observed electron temperature and density with an estimate of the thermal conductivity in the plasma from equation (2.7.1), but it gives a good indication of the magnitude, spread and variation in the background heating. We will come to see later that the background estimate Q_0 was scaled down for both the 15th of August and the 18th of October.

4.5 Solving the electron heat equation

To model the electron cooling we used the electron energy equation we described in chapter 2.4, where the electron temperature profiles along the magnetic field line for HF-off could be determined from a partial differential equation (PDE):

$$\frac{3}{2} k_B n_e \frac{\partial T_e}{\partial t} = \frac{\partial}{\partial z} K_e(T_e, z, t) \frac{\partial T_e}{\partial z} + S(T_e, z, t)$$

where $S(T_e, z, t) = Q_0(z, t) - L(T_e, z, t)$ is the combined background electron heating and cooling rates.

For the PDE solver to not get unnecessary measurement noise due to sharp gradients in the parameters we filtered the electron density and temperatures to get smoother variations. For the electron density we did a polynomial fitting of $\log(n_e)$ to get smooth variations with time. To reduce the observation noise and get better boundary and initial conditions in the PDE for the electron temperature we used a bilateral filter. This was done for both the electron and the electron background temperatures.

After the filtering, we interpolated all the EISCAT parameters so that we could use it for arbitrary height and time scales. We then choose our region of interest to be from 140 to 300 km altitude, as this region should well cover where the majority of the HF-heating is distributed.

4.6 Computing the modeled temperature

The modelled temperature was found by solving the energy equation. The PDE we solved is the non-conservative convective-diffusion equation:

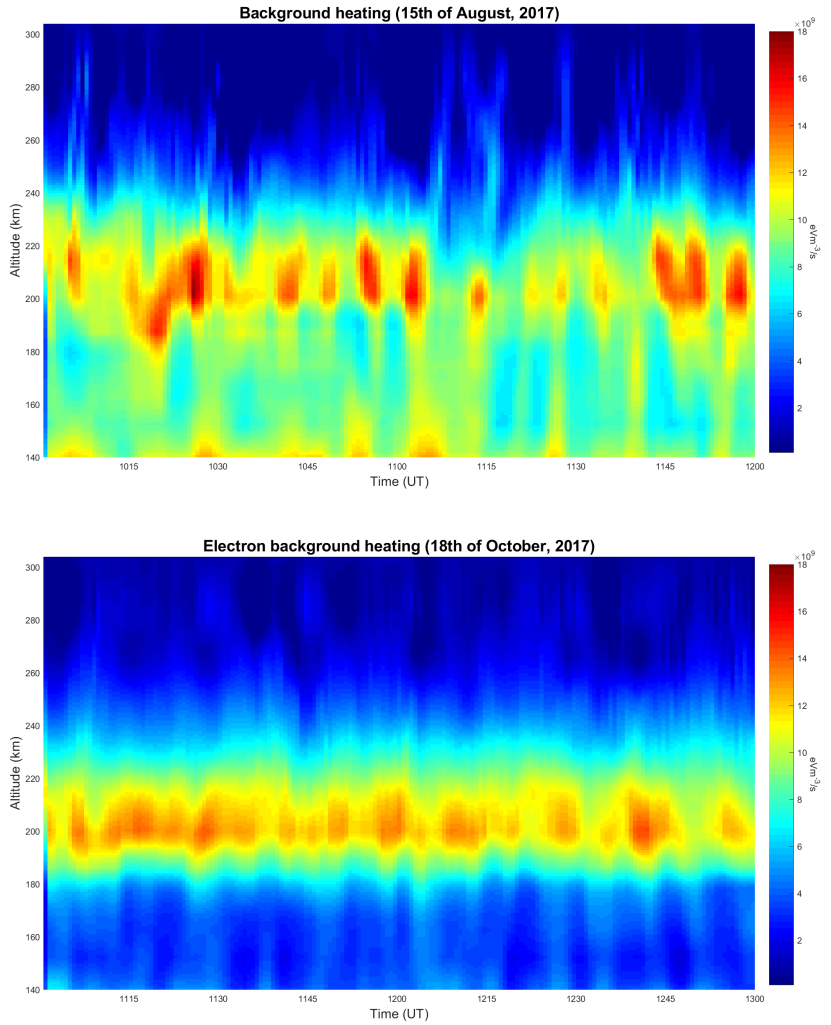

Figure 4.7: Estimated electron background heating, Q_0, for the 15th of August and 18th of October, estimated directly using the EISCAT parameters from the 10 last integrations in each cycle. As a result of the electron density peak being less extended in altitude on the 18th the more concentrated the background heating is at the hmF2 compared to the 15th of August, as is expected. On the contrary the 15th of August has an higher background heating amplitude at hmF2, as is unrealistic with a significantly lower NmF2.

$$A(t,z,T_M)\frac{\partial T_M}{dt} + V(t,z,T_M)\frac{\partial T_M}{dz} = f(t,z,T_M)\frac{\partial^2 T_M}{dz^2} + s(t,z,T_M) \quad (4.6.1)$$

where T_M is the modelled temperature, V is the convective velocity (this we set equal to 0 as the observed ion velocities are small and therefore this term gives insignificant contribution), f is the diffusivity function and s is the source term as described in the section above. The PDE was solved using Green's function approach and Runge-Kutta 2nd order method, described further in Appendix A.2. Equation 4.6.1 was solved over the 120s-time-period after $\mathrm{HF_{off}}$ when T_e decreases to the background steady-state temperature, with initial condition ($t = 0$) set to the observed temperature at $\mathrm{HF_{off}}$. For the initial condition we used a second analysis of the radar data using GUISDAP with the same parameters but time integration over 15 seconds rather than 5, this was done in order to obtain less noisy temperature profiles for the initial condition. The upper boundary condition for the PDE was set to $\frac{\partial T_{eMod}}{dz} = \frac{\partial T_e}{\partial z} = 130$ [K/Range gate] for the two top range gates, assuming that at the top heights there would be no temperature gradient contribution from the HF-heating, and the lower boundary was set to the observed electron temperature, as can be seen in the right panel of figure 4.8 are fitting assumptions.

4.7 Optimizing Parameters

We used a constrained Nelder-Mead simplex search (CNMSS) (Nelder and Mead, 1965) function to minimize the difference between our modelled electron temperature, T_{eM}, and the observed electron temperature, T_e. We wanted to get the minimum cumulative error:

$$err = \sum_{0s}^{120s}\sum_{140km}^{300km} \frac{\left(T_e - T_{eM}(\bar{q})\right)^2}{\sigma^2_{T_e}} \quad (4.7.1)$$

by allowing for slight changes to the parameters $\bar{q}$ in $T_{eM}(\bar{q})$. The sums is over all ranges and time periods of T_e and T_{eM} within the relaxation window and heights of interest. In equation 4.7.1 the standard deviation of the observed temperature, σ_{T_e}, weighs the uncertainty of each point, but as can be seen in the first and second panel of figure 4.10 this uncertainty may not be precise in our measurements due to the short integration time. Because of this a 3×3 median filter was applied to the standard deviations to reduce the risk of over-weighing certain points. Also as the altitude increases, so too does the separation between each range gate, therefore more of the interpolated temperatures (which was set to a fixed 1 km step size) is used for each range gate at higher altitudes. As a result of these two corrections the weighing of each point becomes very prone to changes with altitude, and only slight variations with time as a result of the variance of the measurement, therefore the variance of the observed temperature has almost negligible effect for the CNMSS-optimization.

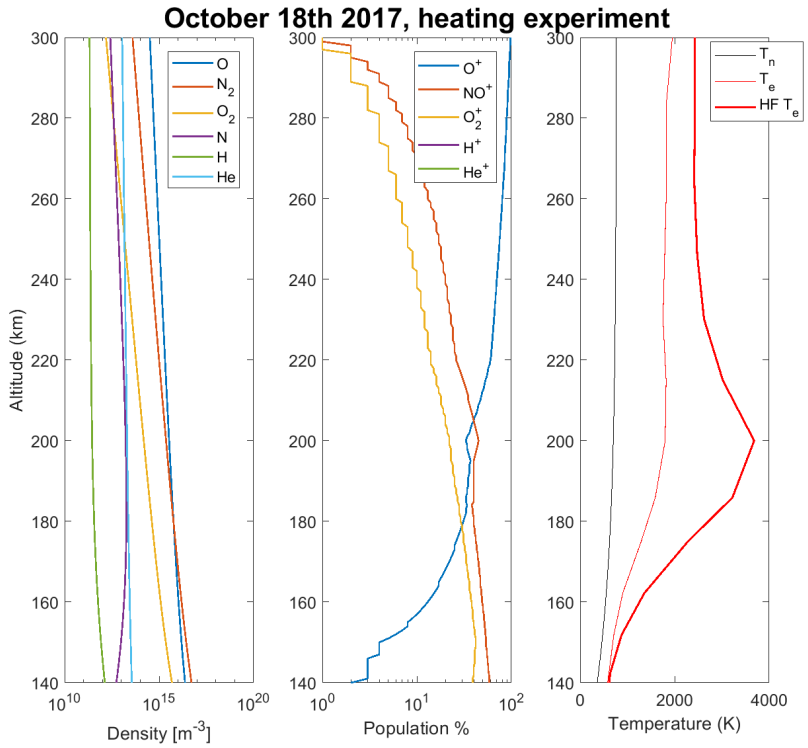

Figure 4.8: Pre-estimated neutral density from MSIS and ion composition from IRI in the first two panels. Last panel shows the estimated neutral temperature (from MSIS, thin black line) and the observed background electron temperature (thin red line) and observed electron temperature during heating (bold red line).

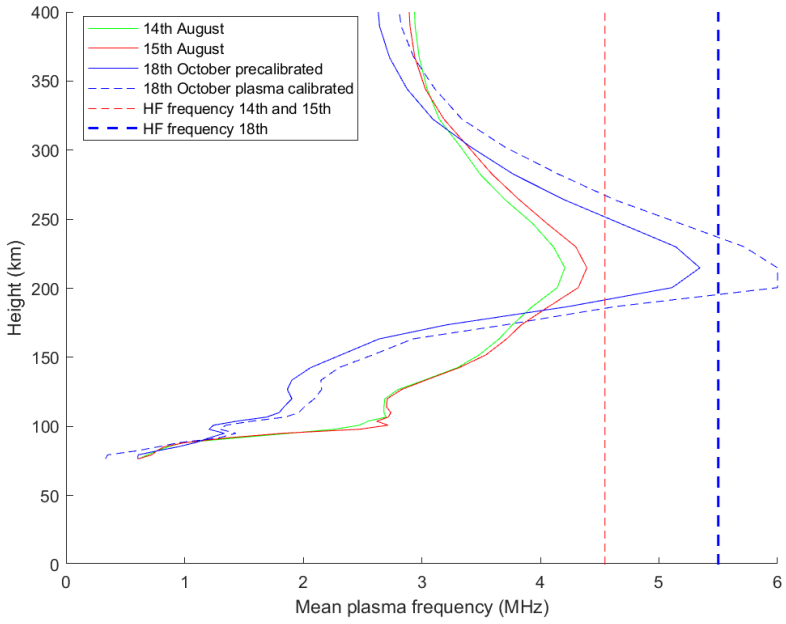

Figure 4.9: Mean electron plasma frequency in the ionosphere (calculated from n_e) during the heating experiment. The red dashed line is the frequency of the HF pump on the 14th and 15th, and the blue bold dashed line is for the 18th. Total reflection of the pump wave was observed on the 18th of October, as the plasma line calibration properly indicates. Much lower electron density in the D and E region for the 18th than 14th and 15th, therefore more HF-heating was absorbed in the lower region for the experiment in August than in October.

The first parameters we set as variables was the temperature gradient at the upper boundary, and the background heating Q_0, the optimization was done individually for each cycle. For the background temperature Q_0 we used the mean background temperature throughout the experiment, it can be seen in figure 5.3.

After optimizing for the upper boundary T_e gradient and background heating, we started optimizing for the F10.7 cm flux, AP index of the day and the atomic oxygen scaling factor. The F10.7 cm flux and AP index are both inputs to the MSIS model atmosphere, and the atomic oxygen is one of the output parameters, this optimization in F10.7 and AP index allows for slight changes to all the MSIS output parameters, with additional scaling to the atomic oxygen density.

The atomic oxygen, molecular oxygen and molecular nitrogen are the dominant constituents of the neutral density at the height of interest, but varying $[O_2]$ and $[N_2]$ in the parameter fitting process has previously given larger cor-

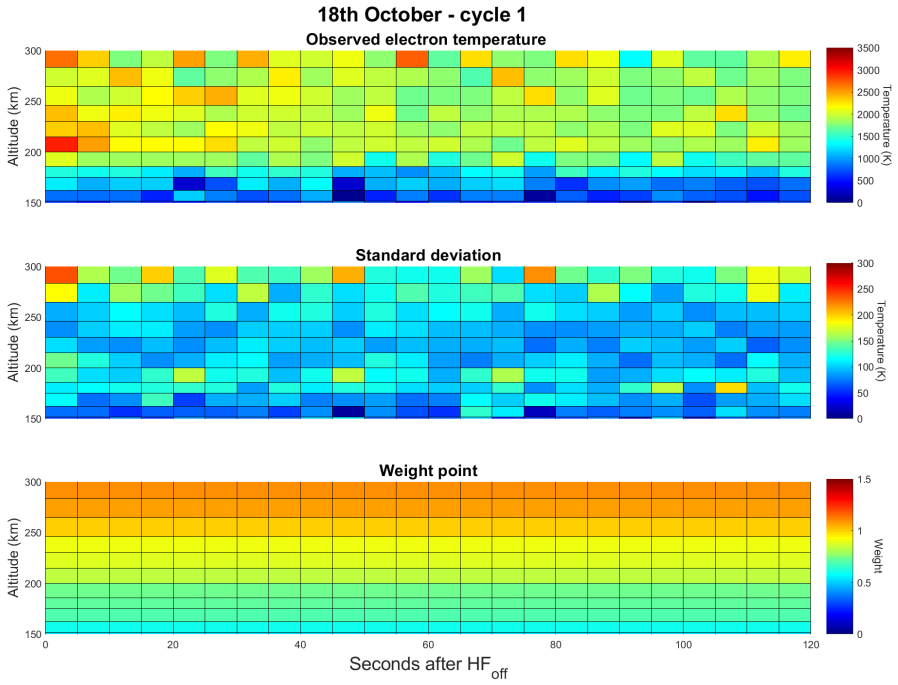

Figure 4.10: Observed electron temperature, standard deviation, and weighted points for each pixel. Many of the standard deviations does not match with the outliers of the electron temperature, i.e (55s, 300km) is clearly an error measurement but gets reported with a relatively low standard deviation, this is one of the disadvantages with a high temporal resolution and may lead to an overconfident certainty in the result. The weight points incorporates both the filtered standard deviation and the increasing separation in the range gates.

rection factors (1.5 - 2) under quiet geomagnetic conditions, as looks unreal (Mikhailov and Lilensten, 2004). Therefore in this study we will only vary [O] and keep $[O_2]$ and $[N_2]$ fixed to the default MSIS values.

Chapter 5

Analysis and Results

During the analysis we will come to see that the results for the 15th of August had significant variance and uncertainties, therefore in this chapter we will carry out the analysis and then show the most-likely parameters for both days, but highlight the results from the 18th of October. At the end we will present the estimated thermospheric densities of the dominant constituents and compare them and the total density with the MSIS.

The CNMSS-optimization (will be referred to as optimization) was set to run for 300 iterations per cycle or until it found a minimum with no positive gradient to a limit 10^{-4}, as was often the case. The optimization for the temperature gradient and the background heating gave the following most-likely values for each cycle:

Table 5.1: Best fit from optimization of $\partial T_e/\partial z$ and C_0.

18th of October					
Cycle	∇T_e^{top}	C_0	Cycle	∇T_e^{top}	C_0
1	1.910	0.649	9	2.018	0.558
2	1.950	0.607	10	2.074	0.554
3	2.013	0.559	11	1.887	0.668
4	2.243	0.451	12	2.131	0.513
5	2.048	0.595	13	2.247	0.450
6	2.144	0.581	14	1.646	0.762
7	2.043	0.652	15	2.032	0.504
8	2.028	0.548	16	1.779	0.600

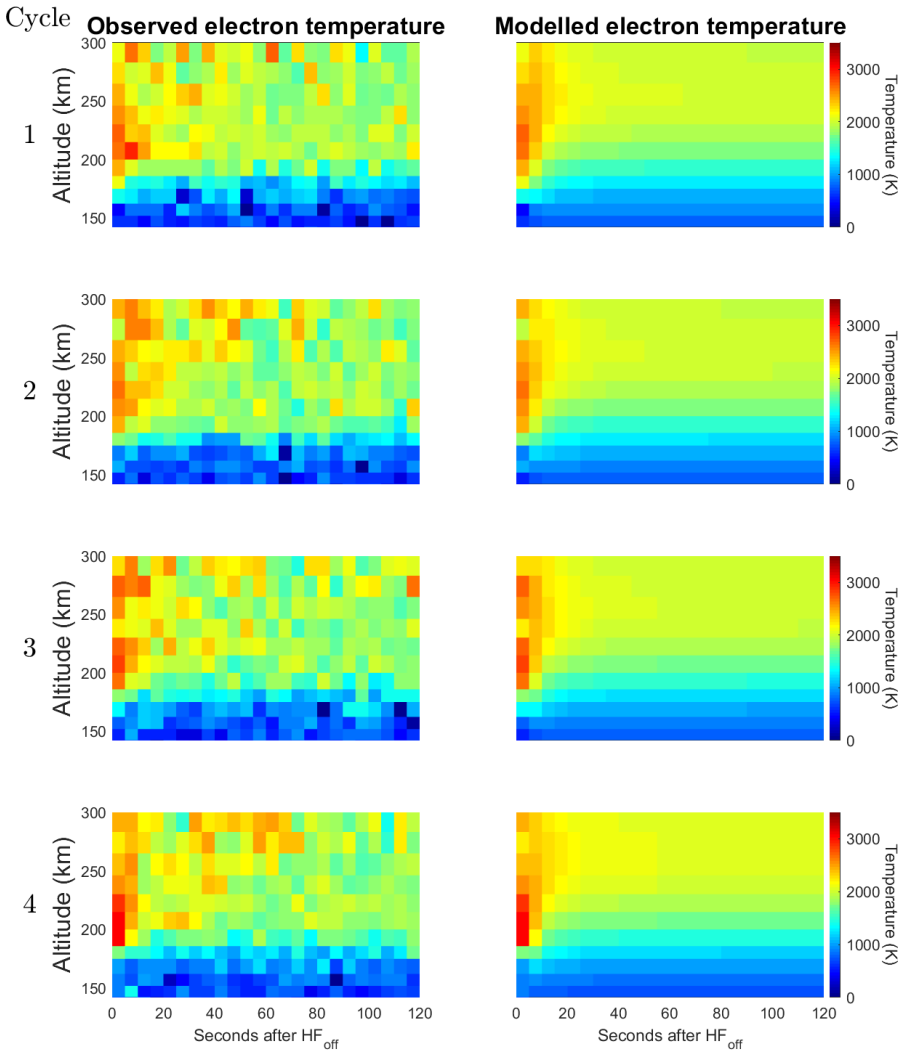

Figure 5.1: Observed and modelled electron temperature for the first 4 heating cycles on October 18th. Here optimized only for gradient $\partial T_e/\partial z$ and a constant C_0 times the background heating, Q_0. The peak background temperature is slightly skewed toward higher altitudes in the modelled than the observed electron temperature. The lower values indicate that the lower boundry condition is promising, $T_{eM} = T_e$.

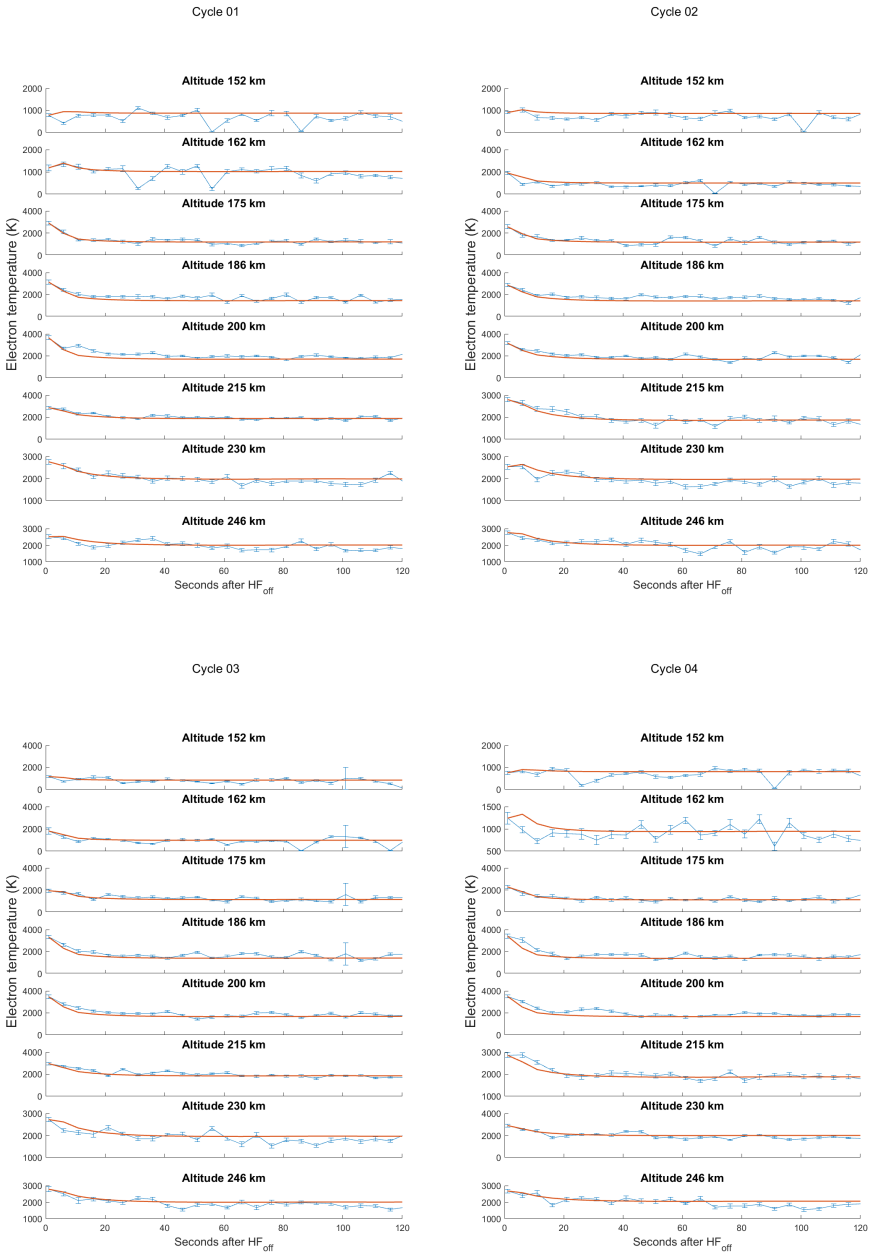

Figure 5.2: Modelled electron temperature (red) and observed electron temperature (blue) with GUISDAP derived errorbars for the 18th of October. Here the first 4 cycles are shown at 8 range gates from 152 to 246 km altitude, this is by only optimizing and modelling the temperature gradient and the background electron heating. At the higher altitudes the background heating may seem to be slightly overestimating the background temperature.

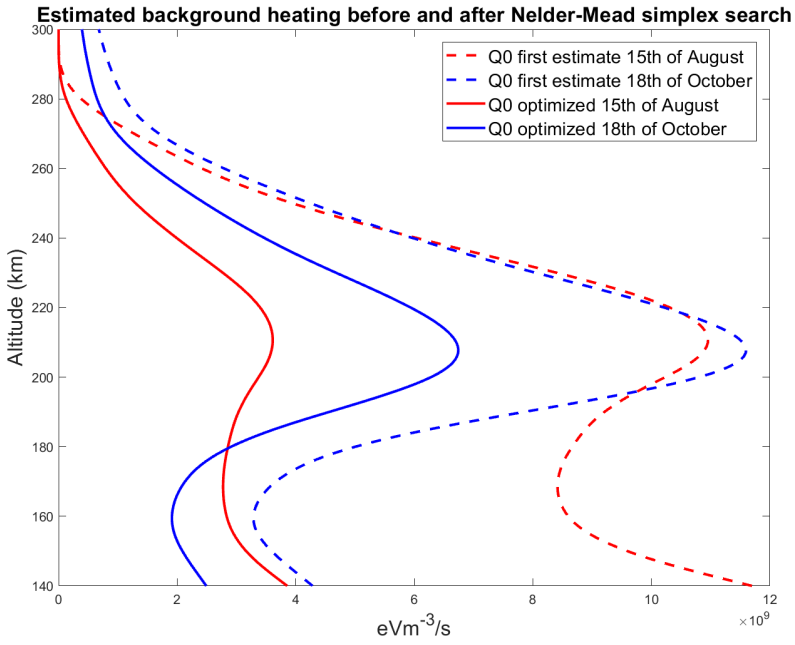

Figure 5.3: Mean electron background heating for both days. The dashed lines are the first estimate from equation (4.4.1), and the bold lines are the post optimized most-likely background heating.

From Table 5.1 the optimization indicate that for all the cycles background heating had to be scaled down by a factor $0.4 - 0.7$ for the 18th of October, this is not unlikely as the initial estimate of the background heating is prone to uncertainties. The lowest and highest C_0 came from cycle 13 and 14, respectively, and under quiet geomagnetic conditions such a change (a factor 1.7 in the background heating) in 6 minutes is not realistic, indicating that there may be significant uncertainties to some of these parameters. The overall C_0 centres around 0.58, with most cycles within $\pm 10\%$.

Figure 5.3 shows the optimized mean background heating from all the cycles as well as the mean of the first estimated background heating that was shown in Figure 4.7 for both days. The optimized background heating show a much more realistic relation between the two days, as both had close to the same quiet ionospheric conditions and the 18th of October had a significantly higher NmF2, therefore it was also expected to have a higher background heating at hmF2. At the lower altitudes the 15th of August had a higher background heating, as reflects the higher electron content compared to the 18th of October at the E and D regions.

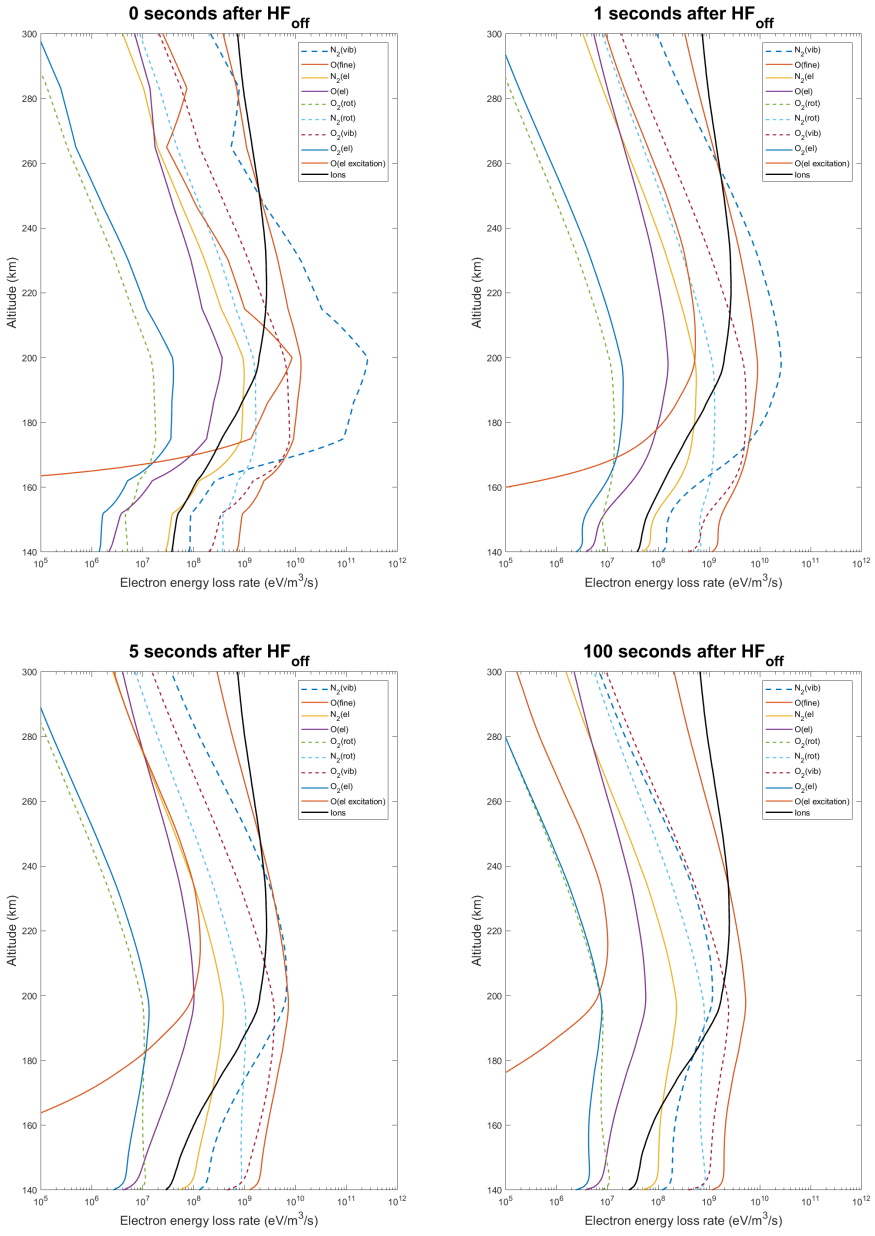

Figure 5.4: Electron energy loss rates to the neutrals and ions right at and shortly after HF_{off}. Vibrational excitation of N_2 is the dominant cooling term in our modelling for the first five seconds, from then the fine structure excitation of the atomic oxygen. The electron-ion energy transfer is less effected by the electron temperature than the electron-neutral energy transfers, that all steadily decreases with the temperature. sharp gradients are observed in the first figure when HF_{off}, this is because it is directly based on the observed temperatures at the initial condition.

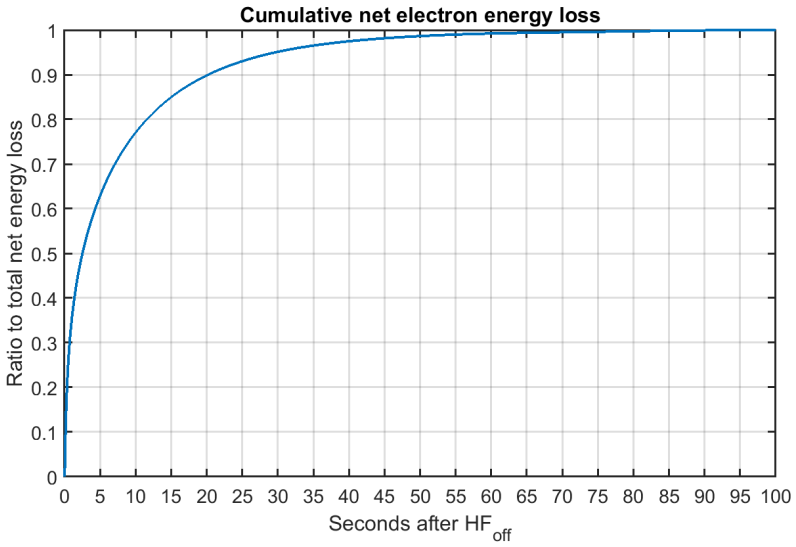

Figure 5.5: Mean cumulative net electron energy loss at 200 km altitude for the 18th of October as a ratio to the total electron energy loss in the first 100 seconds after HF_{off}.

The modelled electron energy loss rates can be seen in Figure 5.4 for the first few seconds shortly after HF_{off}, and the last panel shows the background energy loss rates 100 seconds into the relaxation window when the ionosphere is close to steady-state. Figure 5.5 shows the total cumulative energy loss, and it shows that more than 60% of the modelled electron energy loss happens within the first 5 seconds of HF_{off} where the vibrational excitation of N_2 is of a magnitude higher than the other contributing terms.

The observed and modelled electron temperature for cycle 1 to 4 on the 18th of October can be seen in Figure 5.1 and 5.2, with the most-likely parameters listed in Table 5.1. Comparing these two figures we observe good agreement between the observed and modelled electron temperature, but that there might be a slight overestimate to the modelled background heating at higher altitudes. At the lower altitudes significant spread in the observed temperature is measured, this is likely due to lower signal-to-noise ratio (SNR) as there were a significantly lower electron density in upper E-region, and the fact that we are using very short integration time. Also the GUISDAP errorbars to the observed electron temperatures are peculiarly low compared to the observed variation between consecutive time-steps, where Figure 5.2 shows variability at all altitudes after more than 60 seconds from HF_{off}.

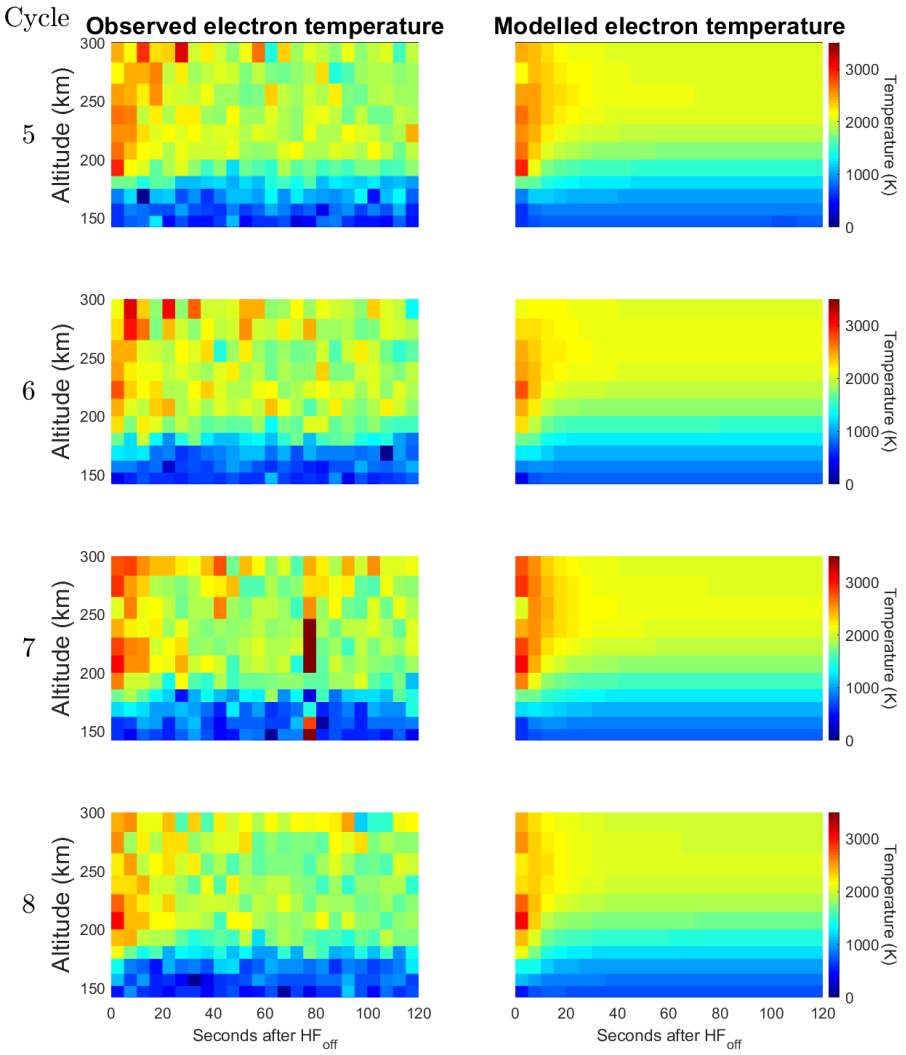

Figure 5.6: Observed and modelled electron temperature for Cycle 5 to 8 for the 18th of October using all the optimized parameters. The modelled temperatures agrees well with the observed electron temperatures.

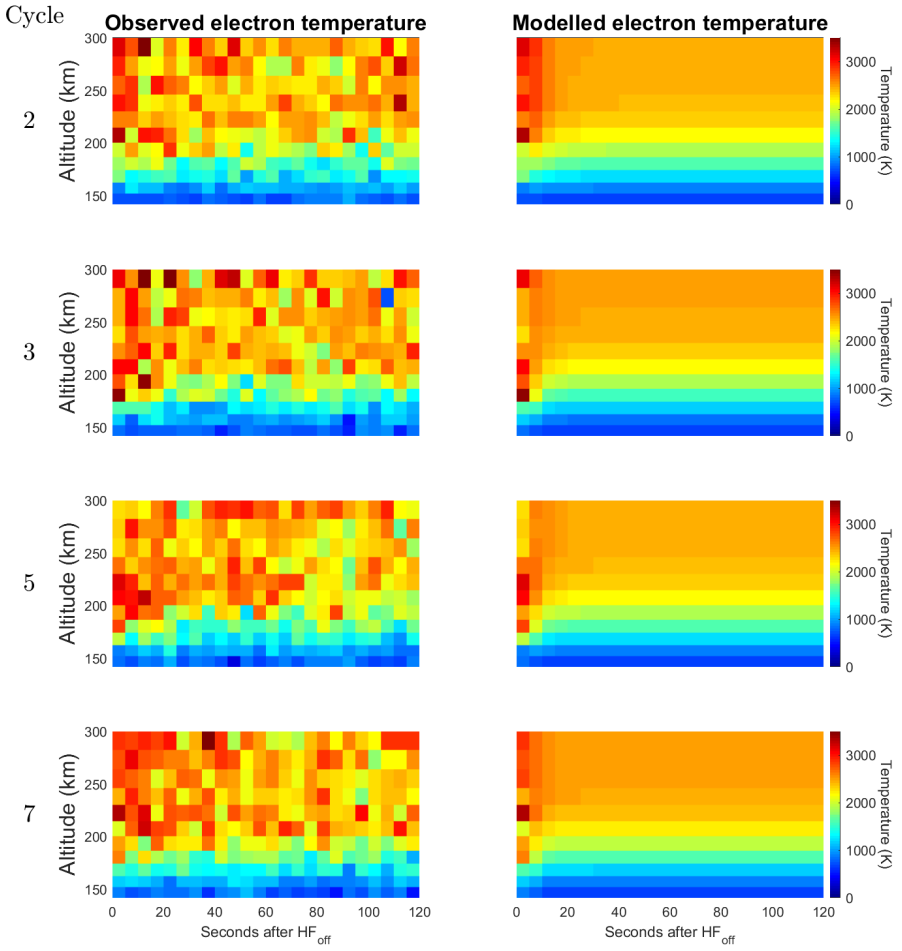

Figure 5.7: Observed and modelled electron temperature using the optimized parameters for the 15th of August. Much higher variance in the observed electron temperature than for the 18th of October, hence also the modelling temperatures had a significantly higher cumulative error (equation 4.7.1) in the CNMSS.

The parameters in Table 5.1 was then set fixed to the most-likely value for each cycle before optimizing for the MSIS input: F10.7cm and AP index, and a scaling factor to the output atomic oxygen density, [O]. We started the optimization from the SWPC reported EUV values for each day shown in Table 4.1, and from 300 iterations for each cycle we got the result seen in Table 5.2.

Table 5.2: Most-likely F10.7, AP and Oxygen factor after optimization for 18th of October

Cycle	F10.7	AP	Oxygen factor	Cycle	F10.7	AP	Oxygen factor
1	55.1290	$3.7 \cdot 10^{-5}$	1.1249	9	60.9310	0	1.0734
2	55.3102	0	1.1143	10	69.7408	50	0.6415
3	75.1397	$1.0 \cdot 10^{-6}$	1.0093	11	61.4218	0	1.0664
4	75.1397	$1.0 \cdot 10^{-6}$	1.0093	12	65.3004	0	1.0507
5	60.1914	$1.0 \cdot 10^{-6}$	1.0800	13	68.9091	0	1.0565
6	69.5658	0	1.0643	14	50.4688	0	1.0991
7	66.8336	$3.0 \cdot 10^{-6}$	1.0759	15	84.1160	0	0.9750
8	64.4220	0	1.0524	16	80.2060	0.0011	1.0001

All the AP values for the 18th of October are converging toward the lower or upper limit for the CNMSS (0 and 50). The AP was reported low (AP= 4) but this may indicate that our model is not sensitive to the AP-dependence, or that it gets overshadowed by the F10.7-dependence as figure 3.6 shows play a more significant role to the neutral density population.

Cycle 7 and 10 had abnormal electron temperatures in the relaxation window, therefore such a big discrepancy is found in the AP and Oxygen factor for cycle 10. Cycle 7 appears to be less affected, and that could be because the abnormality was later in the relaxation window and not shortly after HF_{off}, as was the case for cycle 10.

The combined result for the optimized parameters with estimated standard deviations (for derivation of the standard deviations and mean see Appendix: B.1) can be seen in Table 5.3 and Figure 5.8 for the 15th of August, and Table 5.4 and Figure 5.9 for the 18th of October. The standard deviations varies greatly from cycle to cycle, even if there are good agreements between the parameters, this variation is believed to be mainly caused by the dependence to the calculated standard deviations on the GUISDAP derived observed electron temperatures and the variation in the observed temperatures themselves in each cycle.

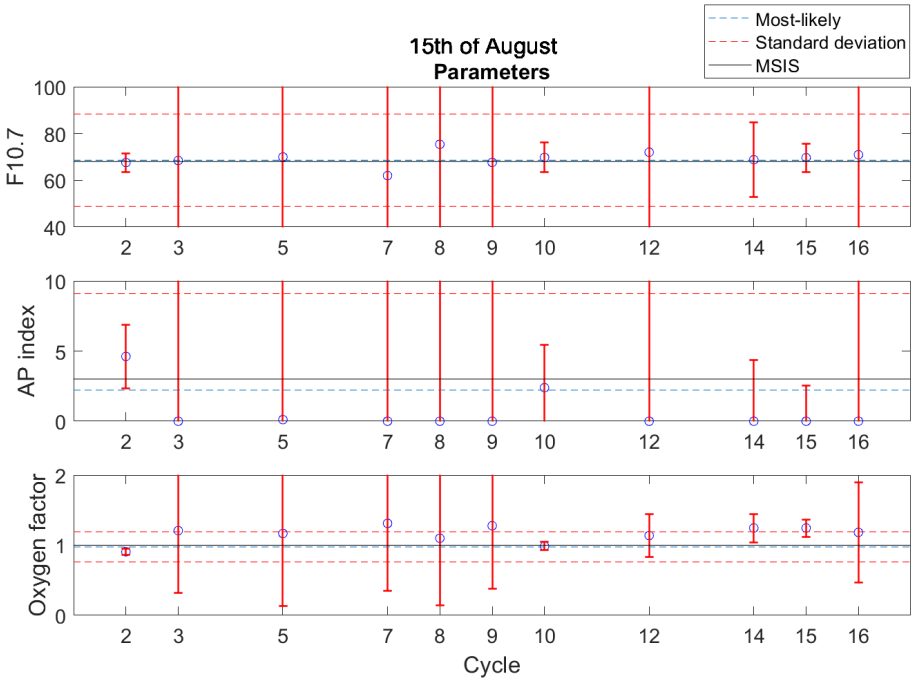

Figure 5.8: Most-likely MSIS parameters for the 15th of August shown for each cycle with estimated standard deviations, and the most-likely parameters from the combined cycles with uncertainties shown in dashed lines, as well as the SWPC suggested EUV fluxes in solid line. The complete numerical list including ∇T_e^{top} and C_0 can be seen in Table 5.3.

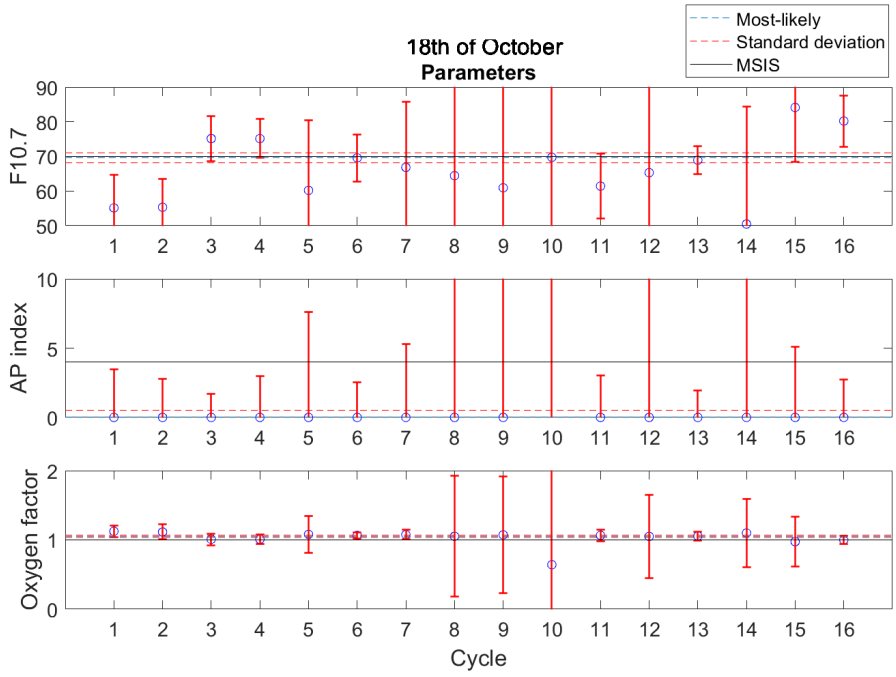

Figure 5.9: Same as Figure 5.8, for the 18th of October. Much lower uncertainties are observed and better agreement between the parameters from cycle to cycle. The complete numerical list including ∇T_e^{top} and C_0 can be seen in Table 5.4.

Table 5.3: Optimized parameters with estimated standard deviations for the 15th of August for each individual cycle.

15th of August

Cycle	∇T_e^{top}	C_0	F10.7	AP	Oxygen factor
2	2.996 ± 0.0637	0.2739 ± 0.0158	67.57 ± 4.16	4.616 ± 2.3833	0.9063 ± 0.051
3	3.089 ± 0.2248	0.2618 ± 0.1877	68.45 ± 84.52	0 ± 30.8466	1.208 ± 0.845
5	2.965 ± 0.2524	0.3303 ± 0.2495	69.96 ± 102.33	0.1099 ± 37.1140	1.167 ± 1.088
7	3.041 ± 0.2519	0.3709 ± 0.2493	61.99 ± 91.88	0 ± 33.8186	1.311 ± 0.976
8	3.164 ± 0.2597	0.2702 ± 0.1961	75.4 ± 98.73	0 ± 34.3147	1.100 ± 0.976
9	3.097 ± 0.2534	0.3926 ± 0.2331	67.65 ± 87.10	0 ± 30.6482	1.278 ± 0.924
10	2.988 ± 0.0237	0.2918 ± 0.0154	69.79 ± 7.64	2.389 ± 3.4123	0.986 ± 0.064
12	3.104 ± 0.1891	0.3886 ± 0.0807	72.01 ± 45.34	0 ± 13.9405	1.138 ± 0.3612
14	3.357 ± 0.1315	0.3113 ± 0.0867	68.8 ± 15.46	0 ± 4.1871	1.246 ± 0.208
15	3.386 ± 0.0342	0.39 ± 0.0647	69.64 ± 6.21	0 ± 2.7159	1.245 ± 0.133
16	3.404 ± 0.1942	0.3456 ± 0.1828	70.94 ± 69.65	0.00193 ± 24.1877	1.183 ± 0.755

Table 5.4: Optimized parameters with estimated standard deviations for the 18th of October for each individual cycle.

18th of October					
Cycle	∇T_e^{top}	C_0	F10.7	AP	Oxygen factor
1	1.910 ± 0.0466	0.6489 ± 0.0535	55.13 ± 9.51	0 ± 3.4904	1.125 ± 0.0815
2	1.949 ± 0.0479	0.6076 ± 0.0585	55.31 ± 8.28	0 ± 2.8003	1.114 ± 0.1076
3	2.013 ± 0.0703	0.5588 ± 0.0555	75.14 ± 6.55	0 ± 1.7175	1.009 ± 0.0833
4	2.244 ± 0.0382	0.4496 ± 0.0385	75.14 ± 5.60	0 ± 2.9600	1.009 ± 0.0682
5	2.049 ± 0.0821	0.595 ± 0.1208	60.19 ± 20.18	0 ± 7.6029	1.08 ± 0.2689
6	2.145 ± 0.0547	0.5812 ± 0.0402	69.57 ± 6.81	0 ± 2.5139	1.064 ± 0.0487
7	2.043 ± 0.0944	0.6521 ± 0.0372	66.83 ± 18.99	0 ± 5.3171	1.076 ± 0.0670
8	2.028 ± 0.1100	0.5484 ± 0.3355	64.42 ± 62.74	0 ± 25.4111	1.052 ± 0.8729
9	2.018 ± 0.1060	0.558 ± 0.3292	60.93 ± 60.08	0 ± 24.6251	1.073 ± 0.8393
10	2.074 ± 0.1568	0.5543 ± 0.4482	69.74 ± 38.87	50.0 ± 57.2140	0.6415 ± 2.2393
11	1.887 ± 0.0614	0.6687 ± 0.0569	61.42 ± 9.30	0 ± 3.0447	1.066 ± 0.0822
12	2.132 ± 0.1022	0.5126 ± 0.2192	65.30 ± 49.11	0 ± 19.0026	1.051 ± 0.6001
13	2.247 ± 0.0284	0.4508 ± 0.0337	68.91 ± 4.12	0 ± 1.9345	1.057 ± 0.0659
14	1.646 ± 0.0912	0.7629 ± 0.2236	50.47 ± 33.96	0 ± 13.1503	1.099 ± 0.4932
15	2.032 ± 0.0291	0.5044 ± 0.1514	84.12 ± 15.69	0 ± 5.1118	0.975 ± 0.3583
16	1.779 ± 0.0772	0.6002 ± 0.0489	80.21 ± 7.40	0.001 ± 2.7382	1.000 ± 0.0626

Table 5.5: Most-likely values for the 15th of August.

∇T_e^{top}	C_0	F10.7	AP	Oxygen factor
3.115 ± 0.055	0.2886 ± 0.0520	68.56 ± 19.78	2.21 ± 6.87	0.976 ± 0.215

Table 5.6: Most-likely values for the 18th of October.

∇T_e^{top}	C_0	F10.7	AP	Oxygen factor
2.0744 ± 0.0108	0.561 ± 0.009	69.60 ± 1.43	0.0108 ± 0.5068	1.053 ± 0.016

From the optimized parameters and the estimated standard deviations we can see that statistical significance may be achieved by repeating the Heating-experiment for many cycles under the same ionospheric-thermospheric conditions. In the case of high NmF2 with low extent, as was the case for the 18th of October, more energy is absorbed at hmF2 and there is a high electron density for the backscatter at the altitudes of interest and the electron temperature can be modelled to a reasonable certainty. The estimated uncertainties in the ∇T_e^{top} and C_0 becomes very small —just 0.5% and 0.016%, respectively— as is peculiar by comparison to the observed variation in these parameters from cycle to cycle.

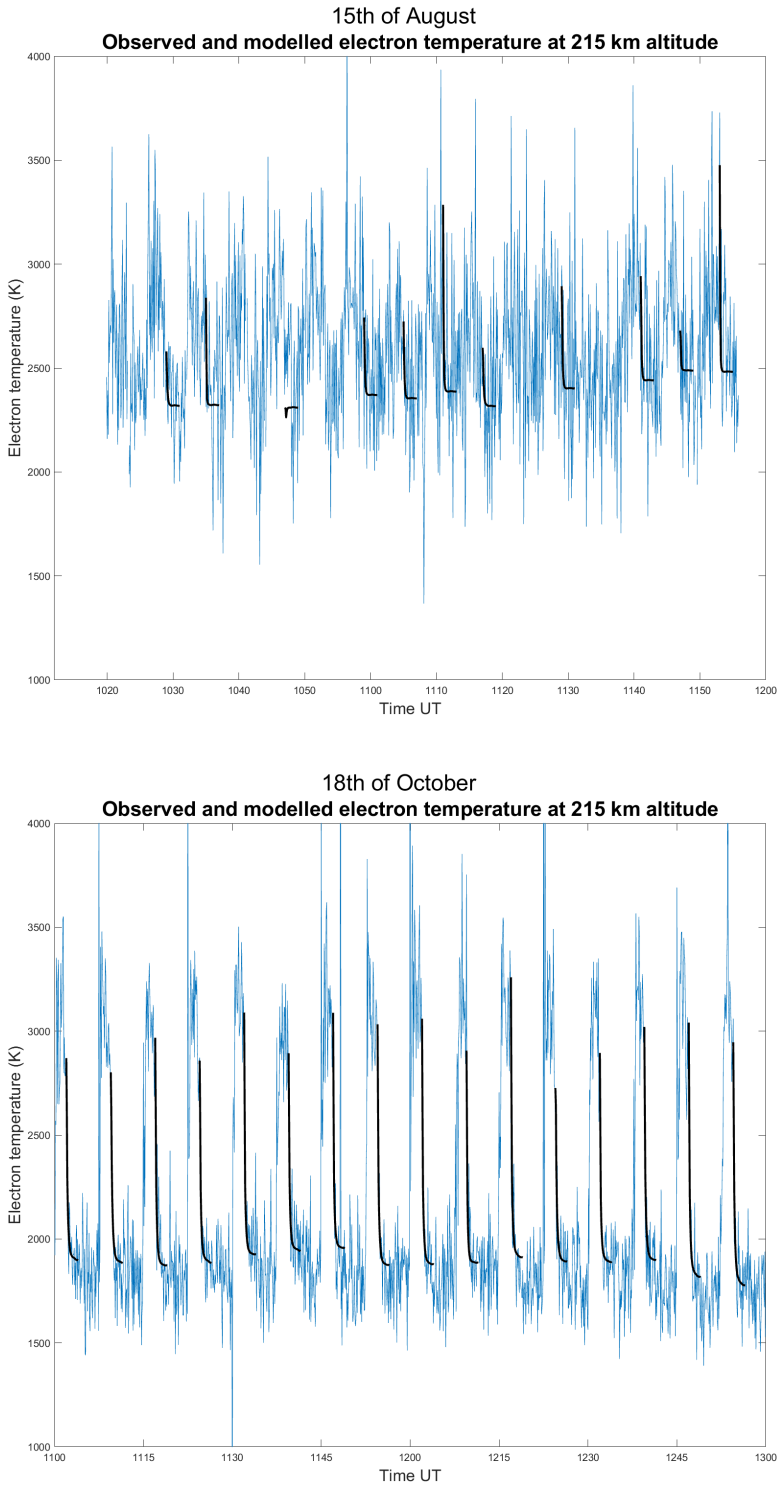

Figure 5.10: Observed electron temperature at the 23rd range gate during the experiment (blue line), and the modelled electron temperature from HF_{off} (black line) for for both days.

The temperature plot for both days in Figure 5.10 shows the modelled and observed electron temperature for the whole experiments at 215 km altitude using the most-likely parameter for their respective cycles. The 15th of August had a slower response to the HF-heating —both at HF_{on} and HF_{off}— and with significantly higher variance and spread from measurement to measurement. This made the modelling for the 15th of August much more uncertain and prone to errors than what was for the 18th of October. A good example is the 5th cycle for the 15th of August shown in Figure 5.10, where the initial condition has been taken from a measurement that certainly does not reflect the true electron temperature at the time of HF_{off} at the 23rd range gate, and this with an initial condition set from a 15 seconds time integrated GUISDAP analysis. The SNR for the observation is of high importance as we are requiring a high temporal resolution, therefore the higher NmF2 —resulting in bigger radar cross-section and more backscatter— for the 18th of October gave much less variation in the observed temperatures. The plots for the 18th of October shows very promising results, where the modelled temperature clearly reflects the observed temperature.

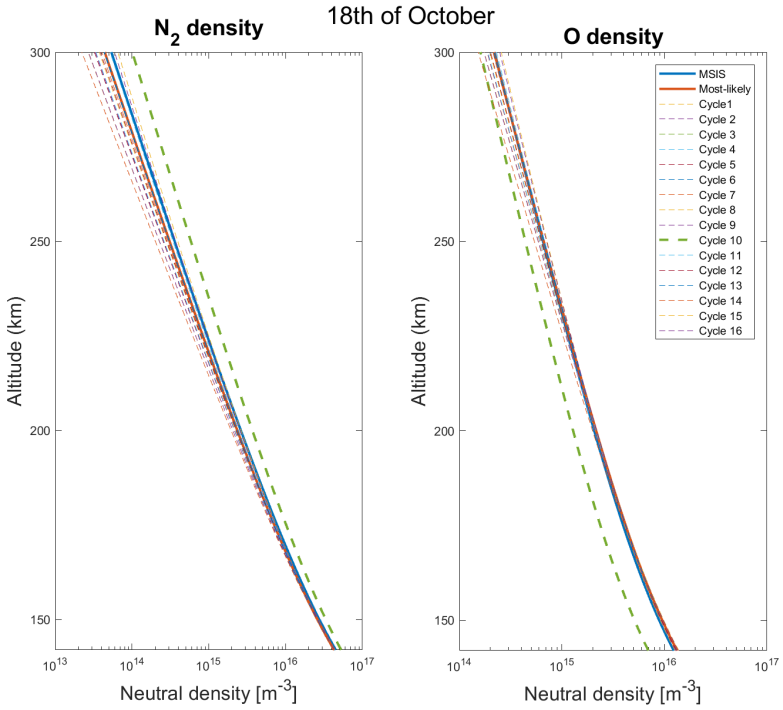

Figure 5.11: Molecular nitrogen and atomic oxygen density estimated using the most-likely parameter for each cycle (dashed lines) and the combined most-likely (red solid line), as well as the MSIS (blue solid).

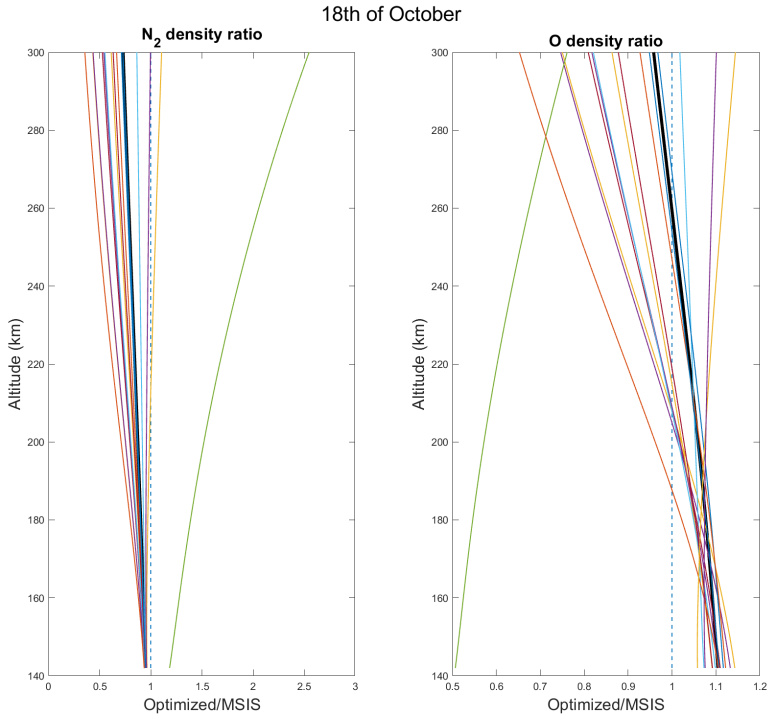

Figure 5.12: N_2 and O ratio between the optimized parameters in each cycle and the MSIS. The most-likely from all cycles are the bold black line, and the dashed blue is the 1 ratio (MSIS). The green outlier is the 10th cycle.

The estimated N_2 is slightly lower than MSIS at the lower altitudes, but the estimated N_2 decreases faster with altitudes than MSIS predicts. The same is for O, but at lower altitudes it starts out higher than MSIS and then decreases to lower values, with an intersection at roughly 250 km, as can be seen in Figure 5.11. At all altitudes O has been scaled with the Oxygen factor, but with increasing altitudes the EUV dependence overshadows the Oxygen factor, even with the increasing O fraction of the upper thermosphere.

The total estimated neutral density with plotted standard errors can be seen in Figure 5.13 for both the 15th of August and the 18th of October. The 15th of August shows a very similar value to the MSIS, but with high standard error. This is an indication that the method has high accuracy if sufficiently many cycles are taken. For the 18th of October the total density decreases faster with altitude than predicted by MSIS, as the estimated EUV fluxes were lower than the reported SWPC values, which has a bigger impact at the higher altitudes.

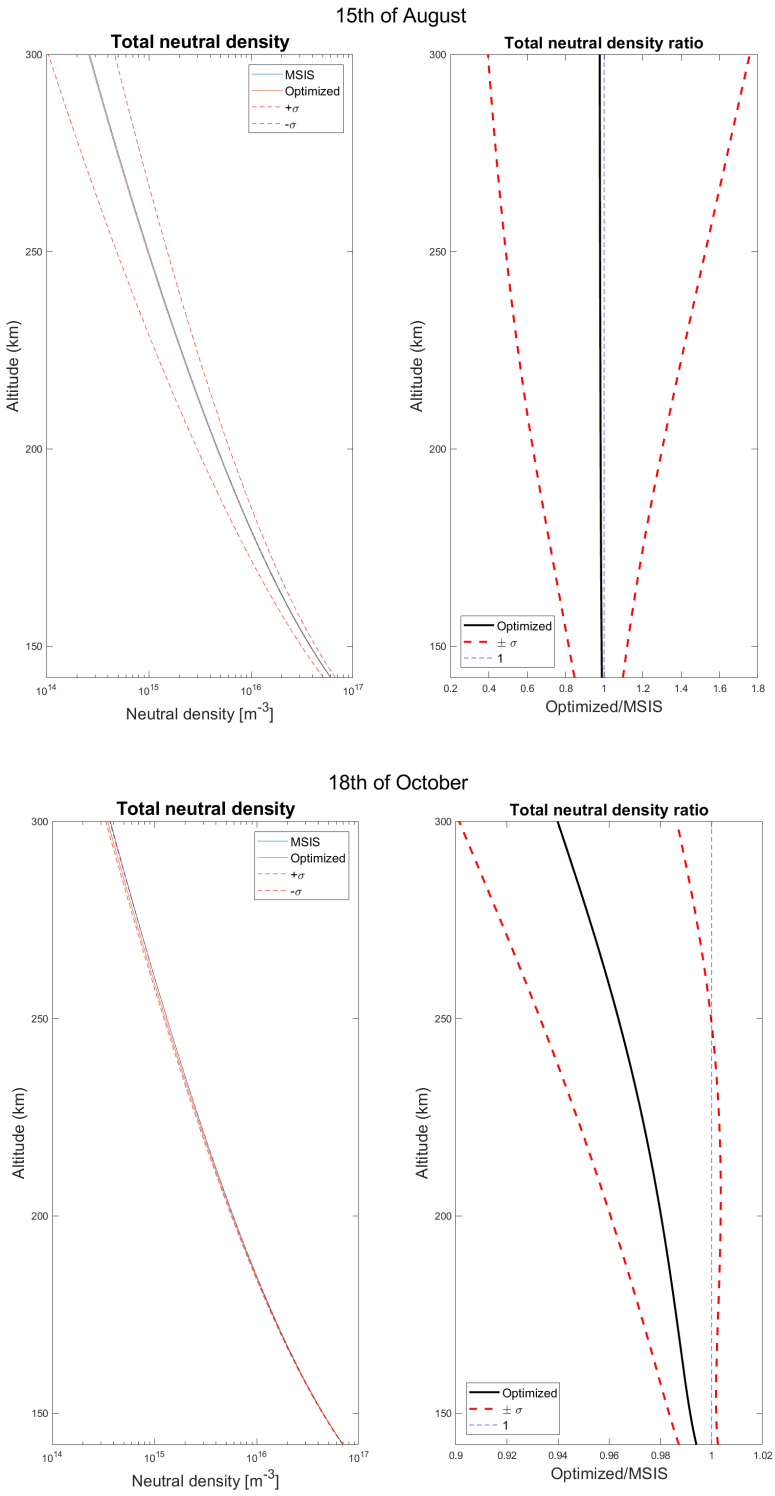

Figure 5.13: Total estimated thermospheric neutral density in the altitude range of interest for both the optimized MSIS parameters and for the daily SWPC reported F10.7 flux and AP values shown in Table 4.1. For the 15th the most-likely thermospheric density is close to the observed MSIS, but with high standard error. The 18th the most-likely density is slightly lower than the suggested MSIS with increasing difference with altitude.

At the lower altitudes the total neutral density from MSIS is within one σ to the estimate for the 18th of October, but at the higher altitudes it falls outside, indicating that the MSIS is likely overestimating the total density.
Figure 5.14 shows the estimated N_2, O and O_2 ratios using the most-likely parameters for the 18th of October and MSIS, with plotted standard errors. The middle panel shows how the oxygen factor dependence has the most impact at the lower altitudes, and then steadily decreases with increasing altitudes where the thermospheric densities gets more prone to changes in the EUV fluxes. The O_2 has the largest discrepancy from the MSIS, with an estimated value at the hmF2 being just a factor 0.80 of the predicted MSIS. The estimated neutral densities from N_2, O and O_2 after optimization can be seen together in Figure 5.15 for comparison. The O_2 had the largest deviation from MSIS, but as it only makes up for roughly 2% of the total neutral density at hmF2, it affects the total density by a factor < 0.005. The standard error are smaller for N_2 and O_2 as they only depend on the EUV fluxes, as is evident at the lower altitudes where the EUV fluxes have less influence, while O has an additional dependence on the Oxygen scaling factor

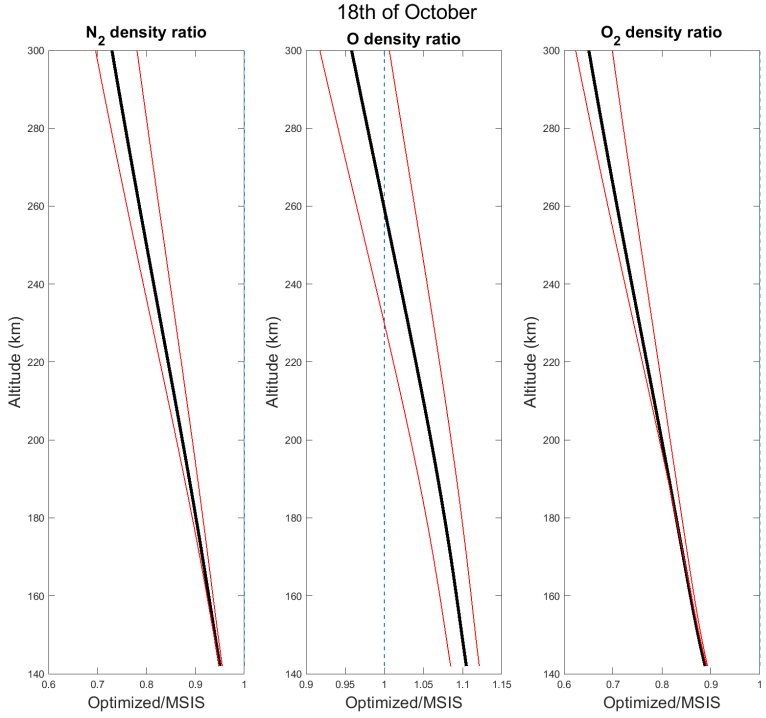

Figure 5.14: Ratio of the most-likely estimate to the MSIS with standard error for both N_2, O and O_2.

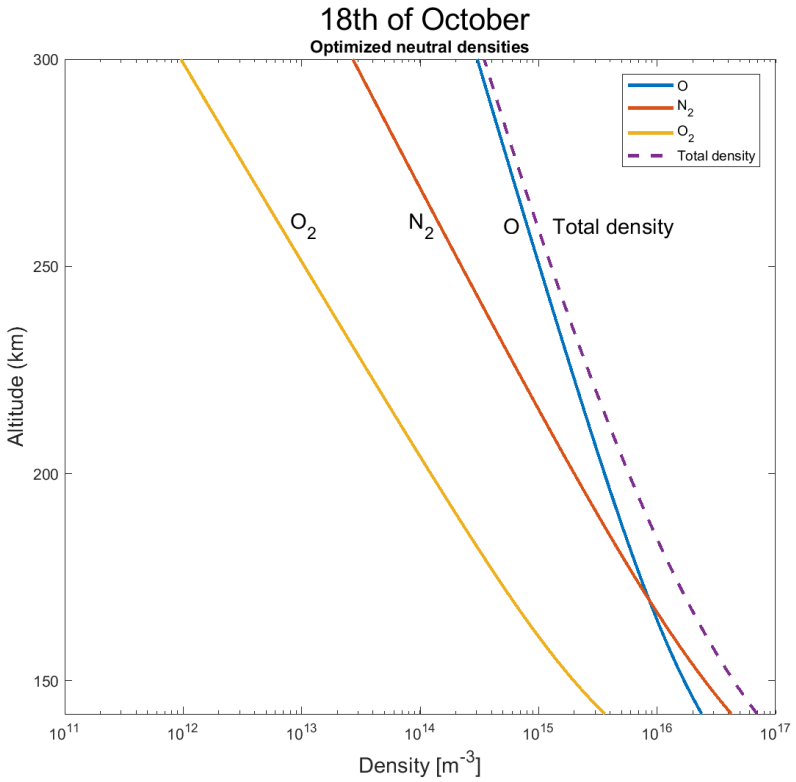

Figure 5.15: Optimized N_2, O and O_2 for the 18th of October.

The largest discrepancy from our estimate to the MSIS for each species is found at the top regions. Because this study relies on significant electron heating for the initial condition, it must be mentioned that the observed neutral densities at the boundaries are of less statistical significance than what is estimated at hmF2 as there are less heating at these altitudes. This implies that the biggest deviations from the MSIS observed at the topside may have higher uncertainties than what is indicated by the errorbars.

Chapter 6

Conclusion and further work

In this study we have modelled the electron cooling during an active HF-radio wave heating experiment using EISCAT-observations and found slight deviations from the MSIS thermospheric densities and the estimated densities on the 18th of October during quiet geomagnetic conditions, and shown that good statistical significance can be achieved if many heating-cycles are used for the same thermospheric-ionospheric conditions.

The total neutral density was modelled to be slightly lower than the predicted MSIS density in the 150 - 300 km altitude for the 18th of October with increasing discrepancies with altitude, ranging from being a factor 0.99 ± 0.01 at the lowest altitudes, 0.98 ± 0.02 at hmF2 and 0.94 ± 0.04 at 300 km of the predicted MSIS neutral density at their respective altitudes.
O was estimated to be a factor 1.11 ± 0.02 of MSIS at the lowest altitude, 1.05 ± 0.03 at hmF2 and 0.96 ± 0.04 at the top side, while N_2 was a factor 0.950 ± 0.002, 0.86 ± 0.01 and 0.73 ± 0.03 at the bottom, hmF2 and top site, respectively.

The total neutral density estimated from the observations on the 15th of August was a factor 0.98 ± 0.37 of the MSIS model at hmF2, with just minor variations (< 0.01) from the bottom to topside, and therefore inconclusive due to the high variance in the observed electron temperatures, leading to a high uncertainty in the final parameters. In addition the plasma line calibration was done only for the 18th of October and not for the data set for the 15th of August, this adds an additional uncertainty to the result for the 15th of August and it is likely that the electron density should also be higher for this day too, leading to larger background heating rates and therefore also affect the neutral density result.

From the results on the 18th of October the method has shown indications of good statistical significance and accuracy if sufficiently many heating-cycles are taken into account, but it should be mentioned that there may have been an overconfident certainty in the parameters due to the apparent low GUISDAP derived standard deviations to the EISCAT observed temperatures. The results from the 15th of August had high standard error but also showed an indication of a good accuracy when many heating-cycles were considered.

From the estimates on the 18th of October it also appears that the modelled temperature is far less affected by error-measurements in the observed temperatures that are later in the modelling window and not shortly after HF_{off}, indicating that more cycles from the 15th of August may have been used in this study.

6.1 Outlook

It was found that all the AP indexes for the 18th of October diverged towards the limits for the CNMSS, which may indicate that our model is insensitive to changes in the AP index. A few cycles on the 15th of August had non-diverging AP indexes, and the estimated mean was just slightly below the SWPC reported index but with a high standard error, therefore more studies should be conducted during varying geomagnetic activity levels to better determine if this is consecutive behaviour or just the low AP value for our particular day of observation.

The arc1 experiment mode may also be of interest for EISCAT-observations during active HF heating experiments as it gives a better spectral and temporal resolution and may therefore allow for better modelling of the electron temperatures. What must be considered —as was observed for the 15th of August— is that the low integration time may give bad SNR if NmF2 is not sufficiently high. However, a higher temporal resolution will make for interesting observations as more than 60% of the electron energy transfer appears to happen within the first 5 seconds of HF_{off}.

Senior et al. (2012) proposed another way to model and scale the background heating using a Gaussian profile with independent upper and lower half-widths, this may be implemented to this experiment and may solve for the slight overestimate of the background heating at the higher altitudes after optimization.

As the effective radiated power (ERP) of the HF-facility increases and the electrons get heated to higher temperatures, appropriate changes should be applied to the modelled cooling rates. Jones et al. (2003) argued that for higher electron temperatures Pavlov (1998b) model overestimates the electron cooling

rates due to vibrational excitation of O, with increasing discrepancy with electron temperature, and must be taken into account as ERP and higher electron heating increases as it is one of the dominant cooling terms at the lower altitude regions (see Figure 5.4). This was not of particular concern for this study as the electron temperatures was slightly less than 4000K at HF_{off}, where the discrepancy between Jones et al. (2003) and Pavlov (1998b) was less than 5%.

A major part of the electron energy loss is due to the vibrational excitation of N_2 shortly after HF_{off}, and at higher electron energies (≥ 2 eV) a depletion in the electron population has been shown to occur due to vibrational excitation of N_2 as may cause the electron energy distribution to deviate from the Maxwellian-distribution above these energy levels (Stubbe, 1981; Gustavsson et al., 2004, 2005; Gustavsson and Eliasson, 2008).

Appendices

Appendix A

Numerical methods for the PDE

A.1 Green's function

Green's function, $G(x, s)$, of a linear differential operator $L(x)$ acting on a distribution over a subset $\mathbb{R}^n$ in the Euclidean space, is the solution at the point s:

$$LG(x, s) = \delta(s - x)$$

where δ is the Dirac delta function. By implying the Green's function, there exists a function $f(s)$ such that:

$$Lu(x) = L\left(\int G(x, s)f(s)ds\right)$$

where $u(x)$ to the differential operator L can be calculated as:

$$u(x) = \int G(x, s)f(s)ds$$

This was applied in the Runge-Kutta 2 (RK2) method to solve the PDE (4.6.1), with maximum allowed width set to 5 km to ignore the non-linear variations of the PDE coefficients with increasing altitudes.

A.2 Runge-kutta

Runge-kutta is an iterative method to solve differential equations numerically. It uses the Euler's method, but with weighted steps at the starting, middle and

end position for the iteration to better predict the solution.

For RK2 the iterative method for a PDE $\dot{y} = f(y)$ with initial condition $y(t_0) = y_0$ is:

$$y_{n+1} = y_n + h\left[b_1 f(y_n) + b_2 f(y_n + h a_1)\right]$$

where h is the step size of each iteration, and b_1, b_2 and a_1 are constant that corresponds to the taylor expansion of the function $y(t)$ centred around t.

$$y(t+h) \approx y(t) + h\dot{y}(t) + \frac{1}{2}h^2\ddot{y}(t) + ...$$

The time steps was selected following the restriction implied by the maximum allowed green function width to $h \approx 0.0365s$; therefore 3280 RK2 iterations was executed for each solution each cycle.

Appendix B

Uncertainty & mean

B.1 Propagation of uncertainty

The uncertainty of the result was calculated using propagation of uncertainty for all the parameters used in the optimization process ($\nabla T_e^{top}, C_0$, F10.7, AP and Oxygen factor) and the uncertainty in the observed electron temperature (from GUISDAP).

We estimated the covariance matrix as:

$$\mathbf{\Sigma_d} = \left(\mathbf{J}^{\mathrm{T}} \mathbf{\Sigma_{Te}^{-1}} \mathbf{J}\right)^{-1} \tag{B.1.1}$$

where $\mathbf{J}$ is the Jacobian matrix for all the parameters used in the optimization and $\mathbf{\Sigma_{Te}}$ the diagonalized matrix of all the GUISDAP interpreted electron temperature errors.
The jacobian matrix we calculated for each parameter using a first order Taylor expansion of the error function around the optimal point:

$$\mathbf{J} = \frac{\partial T_{Mod}}{\partial q} \approx \frac{T_{Mod}(q_{ML} + \Delta p \cdot q_{ML}) - T_{mod}(q_{ML})}{\Delta p}$$

where q_{ML} is the most likely (the best fit from optimization) values for that parameter and Δp is a small perturbation to that state. Here we changed the most likely state of each parameter by $\Delta p = 0.001,\ 0.01$ and 0.1 before solving the PDE and got the change this inflicted to the modelled temperature. Because the AP index diverged to 0 for many of the cycles, in the calculation of the Jacobian it was changed to 0.1. This was done for all the pixels in the relaxation window and heights of interest. We now diagonalized all the elements in each $\mathbf{J}$ into a matrix of size $5 \times$ pixels, and then did the computation for the covariance matrix in equation B.1.1. The reason for changing all parameters with three different Δp was to look for non-linearity in the Jacobian, this was not observed.

This procedure was done individually for each cycle.

We combined the information from all the samples following the chain rule in Fisher information matrix as:

$$\Sigma = \left(\sum_{cycles} \mathbf{J}^{\mathrm{T}} \mathbf{\Sigma_{Te}^{-1}} \mathbf{J} \right)^{-1} \tag{B.1.2}$$

B.2 Variance weighted mean

The most-likely value for each day combined from all the cycles were calculated with a weighted-mean approach, taking the variance of each measurement into account:

$$\bar{x} = \frac{\sum_{i=1}^{n} (x_i \sigma_i^{-2})}{\sum_{i=1}^{n} \sigma_i^{-2}} \tag{B.2.1}$$

B.3 Meta-data

B.3.1 Sum observed electron temperatures & standard deviations

The sum of the total electron temperatures in the relaxation window for each cycle can be seen in Table B.1.

Table B.1: Sum of observed electron temperature and standard deviation in the relaxation window for each Heating-cycle.

Cycle	1.0	2.0	3.0	4.0	5.0	6.0	7.0	8.0
T_e	$4.91\,10^5$	$4.89\,10^5$	$4.92\,10^5$	$4.98\,10^5$	$5.01\,10^5$	$5.01\,10^5$	$5.13\,10^5$	$4.85\,10^5$
σ_{T_e}	$3.3\,10^4$	$3.32\,10^4$	$4.79\,10^4$	$3.43\,10^4$	$3.33\,10^4$	$3.38\,10^4$	$5.63\,10^4$	$3.37\,10^4$
Cycle	9.0	10.0	11.0	12.0	13.0	14.0	15.0	16.0
T_e	$4.91\,10^5$	$5.12\,10^5$	$4.98\,10^5$	$4.9\,10^5$	$4.91\,10^5$	$4.92\,10^5$	$4.85\,10^5$	$4.82\,10^5$
σ_{T_e}	$3.45\,10^4$	$4.72\,10^4$	$3.29\,10^4$	$3.41\,10^4$	$6.44\,10^4$	$6.35\,10^4$	$3.51\,10^4$	$3.54\,10^4$

B.3.2 Covariance Matrices

Composite covariance and correlation matrix

Table B.2: Composite covariance matrix for the 18th of October

$$\begin{pmatrix} 0.0001172 & -6.842\,10^{-5} & 0.01039 & -0.0007888 & -4.98\,10^{-5} \\ -6.842\,10^{-5} & 9.045\,10^{-5} & -0.006053 & 0.000148 & 0.0001327 \\ 0.01039 & -0.006053 & 2.031 & -0.527 & -0.003518 \\ -0.0007888 & 0.000148 & -0.527 & 0.2568 & -0.001187 \\ -4.98\,10^{-5} & 0.0001327 & -0.003518 & -0.001187 & 0.0002532 \end{pmatrix}$$

Table B.3: Composite correlation matrix for the 18th of October

$$\begin{pmatrix} 1.0 & -0.6645 & 0.6731 & -0.1438 & -0.2891 \\ -0.6645 & 1.0 & -0.4466 & 0.0307 & 0.8772 \\ 0.6731 & -0.4466 & 1.0 & -0.7297 & -0.1551 \\ -0.1438 & 0.0307 & -0.7297 & 1.0 & -0.1472 \\ -0.2891 & 0.8772 & -0.1551 & -0.1472 & 1.0 \end{pmatrix}$$

Table B.4: Composite covariance matrix for the 15th of August

$$\begin{pmatrix} 0.003028 & 0.001509 & 0.9256 & -0.2971 & 0.008422 \\ 0.001509 & 0.002709 & 0.8592 & -0.316 & 0.01078 \\ 0.9256 & 0.8592 & 391.3 & -134.8 & 4.042 \\ -0.2971 & -0.316 & -134.8 & 47.19 & -1.44 \\ 0.008422 & 0.01078 & 4.042 & -1.44 & 0.04632 \end{pmatrix}$$

Table B.5: Composite correlation matrix for the 15th of August

$$\begin{pmatrix} 1.0 & 0.5268 & 0.8504 & -0.786 & 0.7111 \\ 0.5268 & 1.0 & 0.8345 & -0.8839 & 0.9626 \\ 0.8504 & 0.8345 & 1.0 & -0.9917 & 0.9495 \\ -0.786 & -0.8839 & -0.9917 & 1.0 & -0.9739 \\ 0.7111 & 0.9626 & 0.9495 & -0.9739 & 1.0 \end{pmatrix}$$

Covariance matrices for the 18th of October

Table B.6: Cycle 1 – 18th of October

$$\begin{pmatrix} 0.002173 & -0.001991 & 0.2806 & -0.05089 & -0.002046 \\ -0.001991 & 0.002864 & -0.1908 & 0.01213 & 0.004031 \\ 0.2806 & -0.1908 & 90.56 & -30.28 & -0.07868 \\ -0.05089 & 0.01213 & -30.28 & 12.18 & -0.05082 \\ -0.002046 & 0.004031 & -0.07868 & -0.05082 & 0.006643 \end{pmatrix}$$

Table B.7: Cycle 2 – 18th of October

$$\begin{pmatrix} 0.002299 & -0.00165 & 0.3227 & -0.07142 & -0.001593 \\ -0.00165 & 0.003426 & -0.1994 & 0.02441 & 0.005932 \\ 0.3227 & -0.1994 & 68.63 & -20.8 & -0.1588 \\ -0.07142 & 0.02441 & -20.8 & 7.842 & -0.008753 \\ -0.001593 & 0.005932 & -0.1588 & -0.008753 & 0.01157 \end{pmatrix}$$

Table 6.8: Cycle 3 – 18th of October

$$\begin{pmatrix} 0.004948 & -0.003249 & 0.327 & 0.03609 & -0.003429 \\ -0.003249 & 0.003083 & -0.212 & -0.04624 & 0.004226 \\ 0.327 & -0.212 & 42.92 & -3.039 & -0.1789 \\ 0.03609 & -0.04624 & -3.039 & 2.95 & -0.09394 \\ -0.003429 & 0.004226 & -0.1789 & -0.09394 & 0.006943 \end{pmatrix}$$

Table 6.9: Cycle 4 – 18th of October

$$\begin{pmatrix} 0.001461 & -0.001048 & 0.0762 & 0.01803 & -0.001053 \\ -0.001048 & 0.001483 & 0.02256 & -0.05177 & 0.002337 \\ 0.0762 & 0.02256 & 31.45 & -12.87 & 0.1224 \\ 0.01803 & -0.05177 & -12.87 & 8.762 & -0.1234 \\ -0.001053 & 0.002337 & 0.1224 & -0.1234 & 0.004647 \end{pmatrix}$$

Table 6.10: Cycle 5 – 18th of October

$$\begin{pmatrix} 0.006742 & -0.001728 & 0.918 & -0.2042 & 0.002139 \\ -0.001728 & 0.01459 & 1.621 & -0.7137 & 0.03108 \\ 0.918 & 1.621 & 407.5 & -146.0 & 4.57 \\ -0.2042 & -0.7137 & -146.0 & 57.8 & -1.857 \\ 0.002139 & 0.03108 & 4.57 & -1.857 & 0.0723 \end{pmatrix}$$

Table 6.11: Cycle 6 – 18th of October

$$\begin{pmatrix} 0.002992 & -0.00173 & 0.2869 & -0.03351 & -0.001114 \\ -0.00173 & 0.001617 & -0.2261 & 0.05108 & 0.001672 \\ 0.2869 & -0.2261 & 46.48 & -12.47 & -0.2111 \\ -0.03351 & 0.05108 & -12.47 & 6.32 & 0.05385 \\ -0.001114 & 0.001672 & -0.2111 & 0.05385 & 0.002369 \end{pmatrix}$$

Table 6.12: Cycle 7 – 18th of October

$$\begin{pmatrix} 0.008911 & -0.002827 & 1.403 & -0.2963 & 0.001433 \\ -0.002827 & 0.001385 & -0.331 & 0.05402 & 0.0009037 \\ 1.403 & -0.331 & 361.0 & -96.61 & 0.6677 \\ -0.2963 & 0.05402 & -96.61 & 28.27 & -0.2038 \\ 0.001433 & 0.0009037 & 0.6677 & -0.2038 & 0.00449 \end{pmatrix}$$

Table 6.13: Cycle 8 – 18th of October

$$\begin{pmatrix} 0.0121 & 0.0168 & 5.11 & -1.89 & 0.0536 \\ 0.0168 & 0.113 & 19.2 & -8.02 & 0.291 \\ 5.11 & 19.2 & 3944.0 & -1600.0 & 52.2 \\ -1.89 & -8.02 & -1600.0 & 646.0 & -21.5 \\ 0.0536 & 0.291 & 52.2 & -21.5 & 0.762 \end{pmatrix}$$

Table 6.14: Cycle 9 – 18th of October

$$\begin{pmatrix} 0.0112 & 0.0136 & 4.44 & -1.63 & 0.0443 \\ 0.0136 & 0.108 & 18.0 & -7.59 & 0.274 \\ 4.44 & 18.0 & 3611.0 & -1488.0 & 47.9 \\ -1.63 & -7.59 & -1488.0 & 606.0 & -20.0 \\ 0.0443 & 0.274 & 47.9 & -20.0 & 0.704 \end{pmatrix}$$

Table 6.15: Cycle 10 – 18th of October

$$\begin{pmatrix} 0.0246 & 0.0517 & 5.67 & -7.55 & 0.286 \\ 0.0517 & 0.201 & 15.8 & -24.7 & 0.993 \\ 5.67 & 15.8 & 1511.0 & -2177.0 & 83.1 \\ -7.55 & -24.7 & -2177.0 & 3288.0 & -127.0 \\ 0.286 & 0.993 & 83.1 & -127.0 & 5.01 \end{pmatrix}$$

Table 6.16: Cycle 11 – 18th of October

$$\begin{pmatrix} 0.00377 & -0.00243 & 0.477 & -0.101 & -0.00183 \\ -0.00243 & 0.00324 & -0.431 & 0.112 & 0.00416 \\ 0.477 & -0.431 & 86.5 & -23.7 & -0.458 \\ -0.101 & 0.112 & -23.7 & 9.27 & 0.113 \\ -0.00183 & 0.00416 & -0.458 & 0.113 & 0.00675 \end{pmatrix}$$

Table 6.17: Cycle 12 – 18th of October

$$\begin{pmatrix} 0.0104 & 0.0136 & 4.03 & -1.43 & 0.0432 \\ 0.0136 & 0.048 & 10.2 & -4.06 & 0.13 \\ 4.03 & 10.2 & 2411.0 & -928.0 & 28.9 \\ -1.43 & -4.06 & -928.0 & 361.0 & -11.3 \\ 0.0432 & 0.13 & 28.9 & -11.3 & 0.36 \end{pmatrix}$$

Table 6.18: Cycle 13 – 18th of October

$$\begin{pmatrix} 8.05\,10^{-4} & -5.95\,10^{-4} & 0.052 & 0.00549 & -6.81\,10^{-4} \\ -5.95\,10^{-4} & 0.00113 & -0.0824 & 0.0131 & 0.00205 \\ 0.052 & -0.0824 & 17.0 & -5.84 & -0.153 \\ 0.00549 & 0.0131 & -5.84 & 3.74 & 0.0291 \\ -6.81\,10^{-4} & 0.00205 & -0.153 & 0.0291 & 0.00435 \end{pmatrix}$$

Table 6.19: Cycle 14 – 18th of October

$$\begin{pmatrix} 0.00831 & -0.00304 & 1.1 & -0.284 & -1.87\,10^{-5} \\ -0.00304 & 0.05 & 6.28 & -2.56 & 0.109 \\ 1.1 & 6.28 & 1166.0 & -442.0 & 15.0 \\ -0.284 & -2.56 & -442.0 & 173.0 & -5.99 \\ -1.87\,10^{-5} & 0.109 & 15.0 & -5.99 & 0.243 \end{pmatrix}$$

Table 6.20: Cycle 15 – 18th of October

$$\begin{pmatrix} 8.47\,10^{-4} & -7.02\,10^{-4} & 0.238 & -0.045 & -2.39\,10^{-4} \\ -7.02\,10^{-4} & 0.0229 & 1.25 & -0.546 & 0.0536 \\ 0.238 & 1.25 & 246.0 & -73.8 & 3.5 \\ -0.045 & -0.546 & -73.8 & 26.1 & -1.43 \\ -2.39\,10^{-4} & 0.0536 & 3.5 & -1.43 & 0.128 \end{pmatrix}$$

Table 6.21: Cycle 16 – 18th of October

$$\begin{pmatrix} 0.00595 & -0.00317 & 0.502 & -0.0424 & -0.00257 \\ -0.00317 & 0.0024 & -0.284 & 0.0325 & 0.0027 \\ 0.502 & -0.284 & 54.9 & -10.9 & -0.231 \\ -0.0424 & 0.0325 & -10.9 & 7.5 & 0.00749 \\ -0.00257 & 0.0027 & -0.231 & 0.00749 & 0.00392 \end{pmatrix}$$

Covariance matrices for the 15th of August

Table 6.22: Cycle 2 – 15th of August

$$\begin{pmatrix} 0.003734 & -0.0005074 & 0.08282 & 0.08463 & -0.0009531 \\ -0.0005074 & 0.0001991 & -0.02147 & -0.005968 & 0.0004058 \\ 0.08282 & -0.02147 & 15.77 & -2.043 & -0.04862 \\ 0.08463 & -0.005968 & -2.043 & 5.131 & -0.04872 \\ -0.0009531 & 0.0004058 & -0.04862 & -0.04872 & 0.002287 \end{pmatrix}$$

Table 6.23: Cycle 3 – 15th of August

$$\begin{pmatrix} 0.05267 & 0.03061 & 18.91 & -6.622 & 0.1683 \\ 0.03061 & 0.03826 & 15.26 & -5.83 & 0.1686 \\ 18.91 & 15.26 & 7970.0 & -2903.0 & 76.23 \\ -6.622 & -5.83 & -2903.0 & 1070.0 & -28.45 \\ 0.1683 & 0.1686 & 76.23 & -28.45 & 0.7879 \end{pmatrix}$$

Table 6.24: Cycle 5 – 15th of August

$$\begin{pmatrix} 0.05974 & 0.04289 & 22.35 & -7.78 & 0.2165 \\ 0.04289 & 0.05446 & 20.72 & -7.72 & 0.2354 \\ 22.35 & 20.72 & 9542.0 & -3429.0 & 97.77 \\ -7.78 & -7.72 & -3429.0 & 1244.0 & -35.8 \\ 0.2165 & 0.2354 & 97.77 & -35.8 & 1.06 \end{pmatrix}$$

Table 6.25: Cycle 7 – 15th of August

$$\begin{pmatrix} 0.05678 & 0.04359 & 19.61 & -6.981 & 0.1925 \\ 0.04359 & 0.06133 & 20.21 & -7.676 & 0.2344 \\ 19.61 & 20.21 & 7965.0 & -2933.0 & 83.28 \\ -6.981 & -7.676 & -2933.0 & 1089.0 & -31.2 \\ 0.1925 & 0.2344 & 83.28 & -31.2 & 0.9257 \end{pmatrix}$$

Table 6.26: Cycle 8 – 15th of August

$$\begin{pmatrix} 0.06725 & 0.03482 & 23.11 & -7.66 & 0.209 \\ 0.03482 & 0.03706 & 16.23 & -5.84 & 0.1776 \\ 23.11 & 16.23 & 9241.0 & -3177.0 & 88.9 \\ -7.66 & -5.84 & -3177.0 & 1104.0 & -31.22 \\ 0.209 & 0.1776 & 88.9 & -31.22 & 0.9106 \end{pmatrix}$$

Table 6.27: Cycle 9 – 15th of August

$$\begin{pmatrix} 0.05993 & 0.03895 & 18.9 & -6.359 & 0.1808 \\ 0.03895 & 0.051 & 16.98 & -6.169 & 0.1975 \\ 18.9 & 16.98 & 7084.0 & -2477.0 & 72.66 \\ -6.359 & -6.169 & -2477.0 & 875.1 & -25.94 \\ 0.1808 & 0.1975 & 72.66 & -25.94 & 0.7999 \end{pmatrix}$$

Table 6.28: Cycle 10 – 15th of August

$$\begin{pmatrix} 0.0004628 & -8.06\,10^{-5} & 0.0003001 & 0.03171 & -0.000138 \\ -8.06\,10^{-5} & 0.0002173 & -0.04093 & 0.01102 & 0.0003316 \\ 0.0003001 & -0.04093 & 41.34 & -14.69 & 0.1484 \\ 0.03171 & 0.01102 & -14.69 & 9.241 & -0.09592 \\ -0.000138 & 0.0003316 & 0.1484 & -0.09592 & 0.003512 \end{pmatrix}$$

Table 6.29: Cycle 12 – 15th of August

$$\begin{pmatrix} 0.02956 & 0.0005148 & 6.084 & -1.644 & 0.03405 \\ 0.0005148 & 0.004426 & 0.9245 & -0.3722 & 0.01495 \\ 6.084 & 0.9245 & 1686.0 & -503.9 & 10.98 \\ -1.644 & -0.3722 & -503.9 & 156.7 & -3.516 \\ 0.03405 & 0.01495 & 10.98 & -3.516 & 0.09353 \end{pmatrix}$$

Table 6.30: Cycle 14 – 15th of August

$$\begin{pmatrix} 0.01606 & -0.005308 & 1.381 & -0.1409 & -0.004338 \\ -0.005308 & 0.006839 & -0.2442 & -0.0838 & 0.01501 \\ 1.381 & -0.2442 & 252.7 & -58.25 & 0.6813 \\ -0.1409 & -0.0838 & -58.25 & 19.06 & -0.4926 \\ -0.004338 & 0.01501 & 0.6813 & -0.4926 & 0.0408 \end{pmatrix}$$

Table 6.31: Cycle 15 – 15th of August

$$\begin{pmatrix} 0.0009388 & -0.0009633 & 0.05194 & 0.02274 & -0.00161 \\ -0.0009633 & 0.003538 & -0.1639 & -0.01225 & 0.006893 \\ 0.05194 & -0.1639 & 37.04 & -10.92 & -0.2277 \\ 0.02274 & -0.01225 & -10.92 & 6.47 & -0.07547 \\ -0.00161 & 0.006893 & -0.2277 & -0.07547 & 0.01515 \end{pmatrix}$$

Table 6.32: Cycle 16 – 15th of August

$$\begin{pmatrix} 0.03331 & 0.0166 & 10.18 & -3.268 & 0.09264 \\ 0.0166 & 0.02979 & 9.451 & -3.476 & 0.1186 \\ 10.18 & 9.451 & 4304.0 & -1482.0 & 44.46 \\ -3.268 & -3.476 & -1482.0 & 519.1 & -15.84 \\ 0.09264 & 0.1186 & 44.46 & -15.84 & 0.5095 \end{pmatrix}$$

Bibliography

Bilitza, D., Rawer, K., Bossy, L., Kutiev, I., Oyama, K.-I., Leitinger, R., and Kazimirovsky, E. (1990). International reference ionosphere 1990.

Brautigam, D., Gussenhoven, M., and Hardy, D. A. (1991). A statistical study on the effects of imf bz and solar wind speed on auroral ion and electron precipitation. *Journal of Geophysical Research: Space Physics*, 96(A4):5525–5538.

Brekke, A. (2013). *Physics Of The Upper Polar Atmosphere*. Springer.

Campbell, L., Brunger, M. J., Cartwright, D., and Teubner, P. (2004). Production of vibrationally excited n 2 by electron impact. *Planetary and Space Science*, 52(9):815–822.

Cowley, S. (2000). Magnetosphere-ionosphere interactions: A tutorial review. *Magnetospheric current systems*, pages 91–106.

Dalgarno, A., McElroy, M. B., Rees, M. H., and Walker, J. (1968). The effect of oxygen cooling on ionospheric electron temperatures. *Planetary and Space Science*, 16(11):1371–1380.

Du Castel, F. and Testud, J. (1974). Some aspects of the design concept of a european incoherent scatter facility in the auroral zone (eiscat project). *Radio Science*, 9(2):113–119.

Folkestad, K., Hagfors, T., and Westerlund, S. (1983). Eiscat: An updated description of technical characteristics and operational capabilities. *Radio Science*, 18(06):867–879.

Gordon, W. E. (1958). Incoherent scattering of radio waves by free electrons with applications to space exploration by radar. *Proceedings of the IRE*, 46(11):1824–1829.

Gustavsson, B. and Eliasson, B. (2008). Hf radio wave acceleration of ionospheric electrons: Analysis of hf-induced optical enhancements. *Journal of Geophysical Research: Space Physics*, 113(A8).

Gustavsson, B., Rietveld, M., Ivchenko, N. V., and Kosch, M. (2010). Rise and fall of electron temperatures: Ohmic heating of ionospheric electrons from underdense hf radio wave pumping. *Journal of Geophysical Research: Space Physics*, 115(A12).

Gustavsson, B., Rietveld, M. T., Grydeland, T., Sergienko, T., Kosch, M., La Hoz, C., Brändström, B., Leyser, T., Isham, B., Gallop, P., et al. (2005). The electron energy distribution during hf pumping, a picture painted with all colors.

Gustavsson, B., Sergienko, T., Häggström, I., Honary, F., and Aso, T. (2004). Simulation of high energy tail of electron distribution function. *Advances in polar upper atmosphere research*, 18:1–9.

Gustavsson, B. J., Löfås, H., Ivchenko, N., Rietveld, M. T., and Leyser, T. (2009). F-region electron heating by x-mode radiowaves in underdense conditions.

Hansen, J., Morales, G., Duncan, L., and Dimonte, G. (1992a). Large-scale hf-induced ionospheric modifications: Experiments. *Journal of Geophysical Research: Space Physics*, 97(A1):113–122.

Hansen, J., Morales, G., and Maggs, J. (1992b). Large-scale hf-induced ionospheric modifications: Theory and modeling. *Journal of Geophysical Research: Space Physics*, 97(A11):17019–17032.

Hedin, A. (1989). Hot oxygen geocorona as inferred from neutral exospheric models and mass spectrometer measurements. *Journal of Geophysical Research: Space Physics*, 94(A5):5523–5529.

Hedin, A., Salah, J., Evans, J., Reber, C., Newton, G., Spencer, N., Kayser, D. C., Alcayde, D., Bauer, P., Cogger, L., et al. (1977). A global thermospheric model based on mass spectrometer and incoherent scatter data msis, 1. n2 density and temperature. *Journal of Geophysical Research*, 82(16):2139–2147.

Hedin, A. E. (1987). Msis-86 thermospheric model. *Journal of Geophysical Research: Space Physics*, 92(A5):4649–4662.

Hedin, A. E. (1991). Extension of the msis thermosphere model into the middle and lower atmosphere. *Journal of Geophysical Research: Space Physics*, 96(A2):1159–1172.

Huuskonen, A., Lehtinen, M., and Pirttilä, J. (1996). Fractional lags in alternating codes: Improving incoherent scatter measurements by using lag estimates at noninteger multiples of baud length. *Radio Science*, 31(02):245–261.

Jones, D. B., Campbell, L., Bottema, M., and Brunger, M. J. (2003). New electron-energy transfer rates for vibrational excitation of o2. *New Journal of Physics*, 5(1):114.

Judd, F. C. (1987). *Radio wave propagation:(HF bands); radio amateur's guide*. Heinemann.

Kunitake, M. and Schlegel, K. (1991). Neutral winds in the lower thermosphere at high latitudes from five years of eiscat data. In *Annales Geophysicae*, volume 9, pages 143–155.

Lehtinen, M., Huuskonen, A., and Pirttilä, J. (1997). First experiences of full-profile analysis with guisdap. In *Annales Geophysicae*, volume 14, pages 1487–1495. Springer.

Lehtinen, M. S. and Häggström, I. (1987). A new modulation principle for incoherent scatter measurements. *Radio Science*, 22(04):625–634.

Lehtinen, M. S. and Huuskonen, A. (1996). General incoherent scatter analysis and guisdap. *Journal of Atmospheric and Terrestrial Physics*, 58(1):435–452.

Litvin, A., Oliver, W., Picone, J., and Buonsanto, M. (2000). The upper atmosphere during june 5–11, 1991. *Journal of Geophysical Research: Space Physics*, 105(A6):12789–12796.

Mantas, G. P., Carlson, H. C., and LaHoz, C. H. (1981). Thermal response of the f region ionosphere in artificial modification experiments by hf radio waves. *Journal of Geophysical Research: Space Physics*, 86(A2):561–574.

Mikhailov, A. and Schlegel, K. (1998). Physical mechanism of strong negative storm effects in the daytime ionospheric f2 region observed with eiscat. In *Annales Geophysicae*, volume 16, pages 602–608. Springer.

Mikhailov, A. V. and Lilensten, J. (2004). A revised method to extract thermospheric parameters from incoherent scatter observations. *Annals of Geophysics*, 47(2-3 Sup.).

Nelder, J. A. and Mead, R. (1965). A simplex method for function minimization. *The computer journal*, 7(4):308–313.

Nicolet, M. (1953). The collision frequency of electrons in the ionosphere. *Journal of Atmospheric and Terrestrial Physics*, 3(4):200–211.

Nygrén, T. (1996). *Introduction to incoherent scatter measurements*. Invers.

Pavlov, A. (1998a). New electron energy transfer and cooling rates by excitation of o 2. In *Annales Geophysicae*, volume 16, pages 1007–1013. Springer.

Pavlov, A. (1998b). New electron energy transfer rates for vibrational excitation of n2. In *Annales Geophysicae*, volume 16, pages 176–182. Springer.

Pavlov, A. and Foster, J. (2001). Model/data comparison of f region ionospheric perturbation over millstone hill during the severe geomagnetic storm of july 15–16, 2000. *Journal of Geophysical Research: Space Physics*, 106(A12):29051–29069.

Picone, J., Hedin, A., Drob, D. P., and Aikin, A. (2002). Nrlmsise-00 empirical model of the atmosphere: Statistical comparisons and scientific issues. *Journal of Geophysical Research: Space Physics*, 107(A12).

Prasad, S. and Furman, D. (1973). Electron cooling by molecular oxygen. *Journal of Geophysical Research*, 78(28):6701–6707.

Rawer, K., Bilitza, D., and Ramakrishnan, S. (1978). Goals and status of the international reference ionosphere. *Reviews of Geophysics*, 16(2):177–181.

Rees, M. H. and Roble, R. G. (1975). Observations and theory of the formation of stable auroral red arcs. *Reviews of Geophysics*, 13(1):201–242.

Reigber, C., Lühr, H., and Schwintzer, P. (2002). Champ mission status. *Advances in Space Research*, 30(2):129–134.

Rietveld, M., Kohl, H., Kopka, H., and Stubbe, P. (1993). Introduction to ionospheric heating at tromsø—i. experimental overview. *Journal of atmospheric and terrestrial physics*, 55(4-5):577–599.

Rietveld, M., Wright, J., Zabotin, N., and Pitteway, M. (2008). The tromsø dynasonde. *Polar Science*, 2(1):55–71.

Rishbeth, H. and Williams, P. (1985). The eiscat ionospheric radar-the system and its early results. *Quarterly Journal of the Royal Astronomical Society*, 26:478–512.

Schunk, R. and Nagy, A. (2009). *Ionospheres: Physics, Plasma Physics, and Chemistry*. Cambridge Atmospheric and Space Science Series. Cambridge University Press, 2 edition.

Schunk, R. and Nagy, A. F. (1978). Electron temperatures in the f region of the ionosphere: Theory and observations. *Reviews of Geophysics*, 16(3):355–399.

Senior, A., Rietveld, M., Yeoman, T., and Kosch, M. (2012). The dependence of f-region electron heating on hf radio pump power: Measurements at eiscat tromsø. *Journal of Geophysical Research: Space Physics*, 117(A4).

Shoucri, M. M., Morales, G., and Maggs, J. (1984). Ohmic heating of the polar f region by hf pulses. *Journal of Geophysical Research: Space Physics*, 89(A5):2907–2917.

Stocker, A., Honary, F., Robinson, T., Jones, T., Stubbe, P., and Kopka, H. (1992). Eiscat observations of large scale electron temperture and electron density perturbations caused by high power hf radio waves. *Journal of atmospheric and terrestrial physics*, 54(11-12):1555–1572.

Stubbe, P. (1971). Energy exchange and thermal balance problems. *J. Scientific and Industrial Res.*, 30:379–387.

Stubbe, P. (1981). Modifying effects of a strong electromagnetic wave upon a weakly ionized plasma: A kinetic description. *Radio Science*, 16(03):417–425.

Stubbe, P. and Varnum, W. (1972). Electron energy transfer rates in the ionosphere. *Planetary and space science*, 20(8):1121–1126.

Swartz, W. E., Nisbet, J. S., and Green, A. E. (1971). Analytic expression for the energy-transfer rate from photoelectrons to thermal-electrons. *Journal of Geophysical Research*, 76(34):8425–8426.

Thome, G. D. and Blood, D. W. (1974). First observations of rf backscatter from field-aligned irregularities produced by ionospheric heating. *Radio Science*, 9(11):917–921.

Thomson, J. A. (1970). Energy deposition in artificial ionospheric heating experiments. *Journal of Geophysical Research*, 75(31):6446–6452.

Thomson, J. J. (1903). *Conduction of electricity through gases*. University press.

Wannberg, G. (1993). The g2-system and general purpose alternating code experiments for eiscat. *Journal of atmospheric and terrestrial physics*, 55(4-5):543–557.

Wikipedia (2004). Thomson scattering — Wikipedia, the free encyclopedia. [Online; accessed 09-December-2017].

Wikipedia (2010). Landau damping — Wikipedia, the free encyclopedia. [Online; accessed 09-December-2017].

Yang, Y., Marshak, A., Mao, J., Lyapustin, A., and Herman, J. (2013). A method of retrieving cloud top height and cloud geometrical thickness with oxygen a and b bands for the deep space climate observatory (dscovr) mission: Radiative transfer simulations. *Journal of Quantitative Spectroscopy and Radiative Transfer*, 122:141–149.